

**University of Alberta**

Tungsten Carbide-based Anodes for Direct Methane Solid Oxide Fuel Cells

by

Alireza Torabi Tehrani

A thesis submitted to the Faculty of Graduate Studies and Research  
in partial fulfillment of the requirements for the degree of

Doctor of Philosophy

in

Materials Engineering

Department of Chemical and Materials Engineering

©Alireza Torabi Tehrani

Spring 2012

Edmonton, Alberta

Permission is hereby granted to the University of Alberta Libraries to reproduce single copies of this thesis and to lend or sell such copies for private, scholarly or scientific research purposes only. Where the thesis is converted to, or otherwise made available in digital form, the University of Alberta will advise potential users of the thesis of these terms.

The author reserves all other publication and other rights in association with the copyright in the thesis and, except as herein before provided, neither the thesis nor any substantial portion thereof may be printed or otherwise reproduced in any material form whatsoever without the author's prior written permission.

To my parents.

# Abstract

This work is focused on development of tungsten carbide-based materials as alternative anodes for direct utilization of methane in solid oxide fuel cells (SOFCs). Not only were the capabilities of the anodes highlighted, but the challenges were also stressed.

First, the impact of porous support microstructure on the electrochemical performance of infiltrated electrodes in SOFCs was investigated. Five distinctly different porous YSZ supports were developed and the influence of size, connectivity and distribution of the pores as well as the configuration of YSZ particles on the surface area and three phase boundary length was analyzed.

Next, the electrochemical characteristics and chemical stability of WC-based anodes were investigated. Two different cells were developed based on a conventional WC-YSZ composite anode and a WC infiltrated porous YSZ supported anode. It was shown that the former cannot be used as an alternative anode because of catastrophic changes in anode microstructure. The latter, however, performed rather stably with no catastrophic degradation. While WC-YSZ anodes were resistant to carbon formation under  $\text{CH}_4$ , the fuel was poorly activated. Upon the addition of  $\text{CeO}_2$  and Ru promoters, the performance was remarkably boosted and the chemical stability of WC was highly improved.

Finally, cells based on Ni-CeO<sub>2</sub>-WC-YSZ anodes were studied. Symmetrical cell study showed that the Ni modified electrode performed stably with methane at 850°C under open circuit condition with no carbon formation. Moreover, the fuel cell results revealed that not only did the anode operate steadily with a reasonable performance in methane fuel, but the stability of the carbide phase was well maintained. The cell also successfully experienced an oxidation-reduction-re carburization cycle. This study indicates that the Ni modified WC-based anodes are compatible with methane fuel, giving reasonable and stable performance.

## Acknowledgements

There are many people who have been memorably supportive in my journey through PhD. First and foremost, I would like to thank my supervisor Professor Thomas H. Etsell for his excellent mentorship. Being encouraging and patient, he has always trusted me and let me learn from experience. His life lesson for me is that failure is one's decision to no longer try.

Second, I would like to thank Dr. Partha Sarkar from Alberta Innovates Technology Future (AITF) for being the most supportive not only by sharing thoughts and ideas, but also by generously providing materials and equipment.

Third, I would like to thank Dr. Natalia Semagina whose generous advice has constantly reinforced my research and whose questions often lead the way for new insights into my work.

Fourth, I would like to thank the very people who have helped me with characterization techniques: Shiraz Merali and Diane Caird for XRD results, De-ann Rolling for SEM and EDS results, Nancy Zhang for BET results, Dimitre Karpuzov for XPS results, and my friend Dr. Amir Hanifi, for TEM images and PSA data.

Fifth, I would like to thank my friends and colleagues whose questions and/or comments have greatly helped me with shedding light on the ambiguities of my work: Dr. Saied Amiri, Dr. Amir Hanifi, Dr. Nemanja Danilovic, Dr. Adrien Vincent, Mr. Kasra Nikooyeh, Mr. Milad Roushanafshar and Mr. Mark Zazulak.

Sixth, I am very grateful to the Department of Chemical and Materials Engineering staff, especially Lily Laser, Heather Green and Marion Pritchard, for being remarkably helpful and exceptionally nice.

Seventh, I am thankful to Natural Sciences and Engineering Research Council of Canada (NSERC) and Solid Oxide Fuel Cells Canada (SOFCC) Strategic Research Network for their financial support.

Finally, I deeply appreciate my family and friends who have been always there for me and lavished me with love.

## Table of Content

Chapter 1: Introduction.....	1
1.1. Research Background.....	1
1.1.1. Introduction.....	1
1.1.2. Solid oxide fuel cell fundamentals.....	3
1.1.2.1. Principles of operation.....	3
1.1.2.2. Microscopic aspects of the electrodes.....	6
1.1.2.3. Thermodynamics of SOFCs.....	8
1.1.2.4. Overpotential.....	8
1.1.3. The development of anode materials.....	10
1.1.3.1. Ni-YSZ anode materials.....	10
1.1.3.2. Carbon deposition.....	12
1.1.3.3. Anode poisoning by fuel impurities.....	15
1.1.3.4. Alternative anode materials.....	17
1.1.4. Principles of ac impedance analysis.....	18
1.2. Research Motivations and Objectives.....	21
1.3. Research Outline.....	23
1.4. Cell Fabrication Process.....	24
References.....	27
Chapter 2: Effects of Porous Support Microstructure on Performance of Infiltrated Electrodes in Solid Oxide Fuel Cells.....	30
2.1. Introduction.....	30
2.2. Experimental Procedure.....	32
2.3. Results and Discussion.....	35
2.4. Conclusions.....	54
References.....	55

Chapter 3: Electrochemical Behavior of Tungsten Carbide-based Materials as Candidate Anodes for Solid Oxide Fuel Cells.....	57
3.1. Introduction.....	57
3.2. Experimental Procedure.....	60
3.3. Results and Discussion.....	62
3.3.1. Sintering.....	62
3.3.2. WC-YSZ composite electrodes.....	63
3.3.3. Electrocatalyst incorporation.....	70
3.3.4. Electrode performance stability.....	74
3.3.5. Electrode reaction mechanisms.....	80
3.3.6. Overall discussion.....	82
3.4. Conclusions.....	84
References.....	85

Chapter 4: Tungsten Carbide-based Anodes for Solid Oxide Fuel Cells: Preparation, Performance and Challenges.....	88
4.1. Introduction.....	88
4.2. Experimental Procedure.....	92
4.2.1. Cell fabrication.....	92
4.2.2. Cell test.....	95
4.2.3. Cell characterization.....	96
4.3. Results and Discussion.....	96
4.4. Conclusions.....	118
References.....	119

Chapter 5: Nickel Modified Tungsten Carbide-based Anode Materials for Direct Utilization of Methane in Solid Oxide Fuel Cells.....	122
5.1. Introduction.....	122
5.2. Experimental Procedure.....	125

5.2.1. Cell fabrication.....	125
5.2.2. Cell test.....	127
5.2.3. Cell characterization.....	128
5.3. Results and Discussion.....	129
5.3.1. Symmetrical study.....	129
5.3.2. Fuel cell study.....	134
5.3.3. Stability issue.....	137
5.3.4. Redox issue.....	143
5.3.5. WC as an anode material.....	149
5.4. Conclusions.....	151
References.....	152
Chapter 6: Concluding Remarks.....	155

## List of Tables

Table 1.1. Physical properties of tungsten carbide and nickel.....	22
Table 2.1. Characteristics of the porous structures studied.....	33
Table 2.2. Particle size and surface area of as received YSZ and calcined and milled YSZ powder.....	37
Table 2.3. Ohmic and polarization resistance of symmetrical cells .....	42
Table 2.4. SSA of the porous structures before and after LSM infiltration.....	42
Table 2.5. Calculated amount of LSM required for a monolayer coverage and the corresponding TPB length.....	53
Table 3.1. Ohmic and non-ohmic polarization of conventional and infiltrated carbide symmetrical cells.....	68
Table 3.2. Ohmic and non-ohmic polarization of different carbide-based symmetrical cells.....	71
Table 3.3. Oxidation of WC in different gas mixtures.....	79
Table 4.1. Summary of the phase analysis after fuel cell test (M: major phase, m: minor phase).....	114
Table 5.1. Ohmic and non-ohmic polarization of a NCWZ symmetrical cell.....	131
Table 5.2. Power densities of cells with Ni-CeO <sub>2</sub> -WC-YSZ (NCWZ) and Ru-CeO <sub>2</sub> -WC-YSZ (RCWZ) [24] anodes.....	136

## List of Figures

Fig. 1.1. Operating principles of a solid oxide fuel cell [8].....	3
Fig. 1.2. Microscopic representation of an anode supported SOFC [9]....	7
Fig. 1.3. Two different mechanisms of sulfur poisoning [29].....	16
Fig. 1.4. Ac impedance analysis of a SOFC. (a) voltage-current dependence, (b) an equivalent circuit model, (c) Nyquist plot of impedance, and (d) Bode diagram of impedance [34].....	20
Fig. 1.5. Schematic cell fabrication procedure: (a) conventional symmetrical cell, (b) infiltrated symmetrical cell, (c) conventional full cell, (d) infiltrated full cell.....	26
Fig. 2.1. SEM micrographs of YSZ-P.....	35
Fig. 2.2. TEM micrographs of (a) as received YSZ and (b) calcined and milled YSZ.....	36
Fig. 2.3. SEM micrographs of CYSZ-P.....	37
Fig. 2.4. SEM micrographs of YSZ-C.....	38
Fig. 2.5. SEM micrographs of YSZ-PC.....	39
Fig. 2.6. SEM micrographs of YSZ-PG.....	39
Fig. 2.7. (a) Ac impedance spectra of the cells at 900°C, (b) Ac impedance spectra of the cells at 800°C, and (c) area specific resistance (polarization) of CYSZ at different temperatures.....	41
Fig. 2.8. Adsorption/desorption isotherms of YSZ-P, CYSZ-P and YSZ-PG (a) before and (b) after LSM impregnation.....	44
Fig. 2.9. BJH pore size distribution of YSZ-P, CYSZ-P and YSZ-PG before and after LSM impregnation: (a) cumulative pore volume distribution and (b) differential pore volume distribution.....	45
Fig. 2.10. Schematic illustration of LSM half spheres closed-packed arrangement (the dashed circles are monosized LSM particles with a radius of $x$ and the black circle is the interparticle cavity with a radius of $r$ .).....	46
Fig. 2.11. SEM micrographs of LSM impregnated porous YSZ structures: (a) CYSZ-P (b) YSZ-P (c) YSZ-C (d) YSZ-PC and (e) YSZ-PG.....	47

Fig. 2.12. SEM micrographs of (a) YSZ-PC showing an LSM-free PMMA-based cavity and (b) YSZ-PG showing a PMMA-based cavity covered with LSM nanoparticles.....	49
Fig. 2.13. SEM micrographs of (a) CYSZ-P showing a multilayer LSM coverage and (b) YSZ-PG showing no multilayer LSM coverage.....	50
Fig. 2.14. (a) Ac impedance spectra of CYSZ-P and YSZ-PG at 800°C within a 72 hr period and (b) stability of CYSZ-P and YSZ-PG.....	51
Fig. 3.1. (a) Ac impedance spectra of WC-YSZ at 800°C in humidified hydrogen for two cells sintered at 1300 and 1400°C, (b) XRD pattern of WZ-1300 after a 100 hour test in humidified hydrogen.....	64
Fig. 3.2. (a) and (b) Ac impedance of a conventional WC-YSZ composite cell and a WC-infiltrated porous YSZ cell under humidified 80% H <sub>2</sub> – 20% CH <sub>4</sub> and humidified CH <sub>4</sub> , (c) an equivalent circuit model.....	67
Fig. 3.3. SEM micrographs of (a) a conventional WC-YSZ composite cell and (b) a WC-infiltrated porous YSZ cell. Vertical arrows point to YSZ and horizontal ones point to WC.....	68
Fig. 3.4. Effect of temperature on the ac impedance of a conventional WC-YSZ composite cell.....	69
Fig. 3.5. Area specific resistances of a conventional WC-YSZ composite cell as a function of temperature.....	70
Fig. 3.6. Ac impedance spectra of different carbide-based symmetrical cells under (a) humidified 80% H <sub>2</sub> – 20% CH <sub>4</sub> mixed atmosphere, and (b) humidified methane at 800°C.....	71
Fig. 3.7. SEM micrograph of RCWZ cell (electrode/ electrolyte interface). As an example, the dip in YSZ electrolyte is well covered with very small ceria particles.....	73
Fig. 3.8. The stability of WZ, CWZ, RWZ and RCWZ (respectively from top to bottom) under an applied current.....	74
Fig. 3.9. Ac impedance spectra of (a) WZ and (b) RCWZ before and after current was applied.....	76
Fig. 3.10. (a) XRD pattern of RWCZ cell after performing the test, (b) XPS spectra of tungsten (W4f) before and after ion etching.....	77

Fig. 3.11. XRD spectra for WC powders treated under atmospheres with oxidizing ratios of 0.88, 1.2, 1.67 and 2.63.....	79
Fig. 4.1. Comparison between a conventional Pt cathode and a LSM infiltrated porous YSZ cathode.....	97
Fig. 4.2. Performance of cells with a conventional WC-YSZ composite anode and a WC-infiltrated porous YSZ anode at 800°C (a) Ac impedance spectra and (b) V-i characteristics.....	99
Fig. 4.3. XRD spectra of the conventional and infiltrated WC-YSZ composite.....	100
Fig. 4.4. Potentiostatic performance (0.7 V) of cells with the conventional WC-YSZ composite anode and a WC-infiltrated porous YSZ anode under humidified mixed fuel at 850°C.....	100
Fig. 4.5. (a) and (b) Ac impedance of a cell with conventional WC-YSZ composite anode and WC-infiltrated porous YSZ anode before and after a potentiostatic test under humidified mixed fuel at 800°C, (c) anode delamination in the conventional sample.....	102
Fig. 4.6. XRD spectra of the conventional and infiltrated WC-YSZ composite after a potentiostatic test under humidified mixed fuel at 800°C.....	104
Fig. 4.7. SEM micrograph of the conventional WC-YSZ anode and YSZ electrolyte interface after a cell test.....	104
Fig. 4.8. XPS spectra of elemental carbon (C1s) in as-received WC powder and a WC-YSZ anode surface after cell test under humidified methane at 800°C.....	105
Fig. 4.9. Ac impedance spectra of a cell with a ceria-Ru promoted WC-infiltrated porous YSZ anode.....	106
Fig. 4.10. V-i characteristics and power densities of a cell with the ceria-Ru promoted WC-infiltrated porous YSZ anode under (a) H <sub>2</sub> -CH <sub>4</sub> mixed atmosphere and (b) CH <sub>4</sub> .....	108
Fig. 4.11. Comparison between the measured OCV of a cell with the ceria-Ru promoted WC-infiltrated porous YSZ anode under humidified methane and the calculated OCV for hydrogen oxidation from the Nernst equation.....	108
Fig. 4.12. SEM micrographs of the ceria-Ru promoted WC-infiltrated porous YSZ anode (R: Ru, C: CeO <sub>2</sub> , W: WC, and Z: YSZ).....	110

Fig. 4.13. (a) Potentiostatic performance (0.7 V) of a cell with the ceria-Ru impregnated conventional WC-YSZ anode at 850°C under mixed fuel, (b) OCV impedance spectra of the cell before and after the stability test.....	112
Fig. 4.14. XRD spectra of a cell with the ceria-Ru impregnated conventional WC-YSZ anode after a potentiostatic test under humidified mixed fuel at 850°C.....	112
Fig. 5.1. (a) Ac impedance spectra of a Ni-CeO <sub>2</sub> -WC-YSZ (NCWZ) symmetrical cell at 800°C under both humidified 80% H <sub>2</sub> – 20% CH <sub>4</sub> and CH <sub>4</sub> atmospheres, (b) an equivalent circuit model.....	130
Fig. 5.2. Ac impedance spectra of the symmetrical NCWZ cell under OCV condition at 850°C under humidified methane.....	133
Fig. 5.3. SEM micrograph of the symmetrical NCWZ cell after being exposed to methane under OCV for 48 hr at 850°C.....	133
Fig. 5.4. Ac impedance spectra of a cell with a Ni-CeO <sub>2</sub> -WC-YSZ anode at 850°C under humidified 80% H <sub>2</sub> – 20% CH <sub>4</sub> atmosphere and humidified methane.....	135
Fig. 5.5. V-i characteristics and power densities of the cell with a Ni-CeO <sub>2</sub> -WC-YSZ anode at 850 and 900°C under the two fuels.....	136
Fig. 5.6. SEM micrographs of the Ni-CeO <sub>2</sub> -WC-YSZ anode (N: Ni, C: CeO <sub>2</sub> , W: WC, and Z: YSZ).....	137
Fig. 5.7. Performance of the cell toward humidified methane, under a constant voltage of 0.7 V at 850°C for 24 hr.....	138
Fig. 5.8. XRD spectrum of a NCWZ anode tested for more than a week.....	139
Fig. 5.9. OCV impedance spectra of the cell before and after the stability test at 850°C under methane.....	139
Fig. 5.10. An SEM micrograph of the Ni-WC-YSZ anode operated on humidified 80% H <sub>2</sub> – 20% CH <sub>4</sub> and humidified methane fuels.....	142
Fig. 5.11. Schematic drawing of the cell configuration, (a) before and (b) after infiltration.....	144
Fig. 5.12. OCV change of the cell during an oxidation-reduction cycle.....	145
Fig. 5.13. OCV impedance behavior of the cell during a course of recarburization after the oxidation-reduction cycle.....	146

Fig. 5.14. V-i behavior of the cell during the recarburization process.....	147
Fig. 5.15. OCV impedance spectra of the recarburized cell before and after a 24 hour potentiostatic test at 850°C under the mixed fuel.....	149
Fig. 5.16. SEM micrograph of an interface between the Ni-CeO <sub>2</sub> -WC-YSZ anode and YSZ electrolyte after the oxidation-reduction-recarburization cycle.....	149

## List of Abbreviations

AMT	Ammonium Metatungstate
BE	Binding Energy
BET	Brunauer-Emmett-Teller
BJH	Barrett-Joyner-Halender
CTE	Coefficient of Thermal Expansion
DM	Direct Methanol
EIS	Electrochemical Impedance Spectroscopy
EMF	Electromotive Force
FWHM	Full Width at Half Maximum
GDC	Gadolinium-doped Ceria
IUPAC	International Union of Pure and Applied Chemistry
LSM	Strontium-doped Lanthanum Manganite
LST	Lanthanum-Strontium Titanate
LSV	Strontium-doped Lanthanum Vanadate
MIEC	Mixed Ionic Electronic Conductors
OCP	Open Circuit Potential
OCV	Open Circuit Voltage
PEM	Proton Exchange Membrane
PMMA	Polymethyl Methacrylate
SDC	Samarium-doped Ceria
SEM	Scanning Electron Microscope
SOFC	Solid Oxide Fuel Cell
SSZ	Scandia Stabilized Zirconia
TEM	Transmission Electron Microscope
TPB	Triple Phase Boundary
XPS	X-ray Photoelectron Spectroscopy
XRD	X-ray Diffraction
YSZ	Yttria Stabilized Zirconia

# Chapter 1

## Introduction

### 1.1. Research Background

#### 1.1.1. Introduction

A fuel cell is an electrochemical device which directly and efficiently converts chemical energy of a fuel into electrical energy by exploiting the spontaneous reaction between oxygen and the fuel. The primitive demonstration of this conversion was successfully accomplished in 1839 by William Grove [1]. However, the evolution of early scientific experiments into commercially viable industrial products has been quite challenging. Complications in commercialization of fuel cells essentially have to do with the lack of proper materials and fabrication methods which are cost effective [2].

The advantages of fuel cells over traditional power generation systems are numerous [1-4]. Undoubtedly, the most prominent benefit of fuel cells is their high energy conversion efficiency associated with direct conversion of chemical energy to electrical energy. A further feature of this is that the high conversion efficiency is relatively size-

independent. In addition, as compared with internal combustion engines which are constrained by the Carnot limit, fuel cells are remarkably more environmentally friendly since they emit negligible amounts of  $\text{NO}_x$ ,  $\text{SO}_x$  or particulate pollutants. Among other benefits offered by fuel cells are: minimal placing restriction, modularity, portability and quiet operation.

In the past few years, numerous attempts have been made to develop and improve fuel cell technology. To date, five major fuel cells have been developed: alkaline, phosphoric acid, polymer electrolyte membrane, molten carbonate, and solid oxide fuel cell. This classification is based on their electrolyte types [3-5].

Predominantly, the main restriction on fuel cells is fuel supply [6]. Hydrogen is referred to as being the ideal fuel for fuel cell systems; however, there are significant concerns relating to hydrogen generation and storage that must be addressed before it can be commercially used. Among the different types of fuel cells, the solid oxide fuel cell (SOFC) is the one which can utilize a wide variety of fuels, including natural gas, coal gas, biogas, alcohol and gasoline, besides hydrogen [7]. This fuel flexibility and use of existing fuel infrastructure to bridge the hydrogen infrastructure gap is the major advantage of SOFCs over other fuel cells. Moreover, since SOFCs operate at high temperatures (600-1000°C), the generated heat can be used in different ways such as running a gas turbine or an endothermic internal fuel reformer [6,7].

Having these promising advantages, solid oxide fuel cells have received a great deal of attention in the past few years. However, commercialization of these efficient power sources is still suffering from a lack of sufficient materials knowledge. Since the cell system is

exposed to the fuel on the anode side, the problem is even more challenging when the development of anode materials is considered. This study aims to deal with this problem to overcome the limitations of state-of-the-art anode materials.

### 1.1.2. Solid oxide fuel cell fundamentals

#### 1.1.2.1. Principles of operation

The operating principles of a solid oxide fuel cell are illustrated schematically in Figure 1.1. A single SOFC, similar to all fuel cells, comprises three main components: a cathode or air electrode, an anode or fuel electrode, and an electrolyte. Essentially, what distinguishes SOFCs from other fuel cell systems is that the electrolyte is an oxide ion conducting ceramic. In practice, two types of SOFCs have been studied: oxygen ion conducting ceramics and proton conducting ceramics. However, most researchers have been focused on the former [1,6].

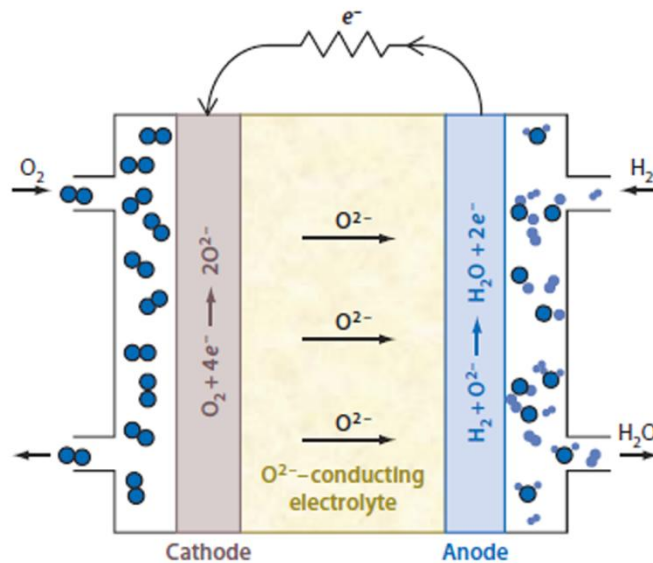


**Fig. 1.1.** Operating principles of a solid oxide fuel cell [8]

The major function of the cathode is to provide reaction sites for the electrochemical reduction of oxygen molecules. Using electrons supplied from an external circuit, molecular oxygen is reduced to oxygen anions based on the following reaction:

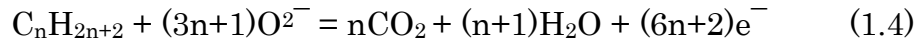


In addition to being catalytically active, which is required to dissociate oxygen molecules, the cathode must be electronically conductive in the oxidizing environment at high temperatures. Several precious metals and electronically conductive ceramics are viable to satisfy these criteria. The latter are the materials of choice since the former are restricted due to high cost. Since previous studies [7] have shown that the cathodic reaction predominantly occurs at the three phase boundary (TPB), where the cathode, the electrolyte and the gas phase meet, it is extremely desirable that the cathode exhibit both ionic and electronic conductivity in order to markedly extend the reaction zone. Other critical features for cathode materials are: chemical and morphological stability, as well as thermal expansion match with other cell components. To date, the most common cathode is strontium doped lanthanum manganite (LSM) which is a p-type perovskite. Another oxide of interest as a cathode material is doped lanthanum cobaltite, specifically for intermediate temperature SOFCs [1,7].

The main function of the electrolyte is to transport ions between the cathode and anode. Accordingly, the electrolyte material must be ionically conductive and electronically insulative over a wide range of oxygen partial pressures, from about 1 atm at the cathode side to lower than  $10^{-20}$  atm at the anode side [6]. What determines the operating temperature of SOFCs is essentially the temperature required to achieve sufficient ionic conductivity in the electrolyte. In addition, the electrolyte must be fully dense to prevent any gas cross leakage,

chemically and morphologically stable in both reducing and oxidizing atmospheres, and compatible with other cell components with respect to thermal expansion. The most favored material has been yttria stabilized zirconia (YSZ) thus far. As an alternative electrolyte material, ceria-based oxides have been extensively considered especially for reduced temperature operation (600-800 °C) [7].

Providing reaction sites for electrochemical oxidation of the fuel is basically the major function of the anode. Due to the difference in oxygen chemical potential between the cathode and anode, oxygen anions migrate from the air side to the fuel side through the electrolyte and oxidation of the fuel occurs according to the following reactions:



Since the released electrons must be transferred to the external circuit, the anode by necessity must be electronically conductive. Analogous to the cathode, it is highly advantageous for the anode to exhibit both electronic and ionic conduction either as a single material or a composite to allow the reaction to be spread over a much broader region [6,7,9,10]. Chemical and morphological stability and thermal expansion compatibility with other cell components are obviously the other requirements for appropriate anode materials. Until now, a nickel-zirconia ceramic-metal composite is the most prevalent anode material especially where hydrogen is the fuel; however, there are several significant limitations for Ni-based cermets when fuels other than hydrogen are considered. This will be discussed in detail later.

To provide structural support for the SOFC, any of the three cell components can be utilized. Since ionic resistivity of the electrolyte is

considerably higher than electronic resistivity of the cathode and the anode, the electrolyte contribution to ohmic loss is significant (the ionic resistivity of YSZ at 800°C is about 50  $\Omega \cdot \text{cm}$ ; on the other hand, the electronic resistivity of LSM and Ni-YSZ are about  $10^{-2} \Omega \cdot \text{cm}$  and  $10^{-4} \Omega \cdot \text{cm}$  respectively). Therefore electrolyte-supported cells, which traditionally have been widely used, are less desirable. Recently, most studies have focused on electrode-supported cells, in which the electrolyte is as thin as 5 to 30 microns [6,7].

### *1.1.2.2. Microscopic aspects of the electrodes*

Due to the fact that the electrode microstructure significantly affects cell performance in SOFCs [10,11], a brief discussion of how the electrode operates on a microscopic scale is noteworthy. A microscopic representation of an anode supported SOFC is schematically shown in Figure 1.2. In electrochemistry, in general, charge transfer is a basic step in electrode reactions, wherein a neutral species is converted into an ion or vice versa. In solid state electrochemistry, this step involves three phases: the ion conducting electrolyte, the electron conducting electrode and the gas phase. If conduction of ions is restricted to the electrolyte, charge transfer occurs at the three phase boundary (TPB), where the three phases converge. Therefore, if any of these three phases could not participate in a potential reaction zone, that zone is unable to make any contribution to the cell performance. Characterized by a line along the electrolyte surface, the TPB essentially affects electrode kinetics [6-10].

The idea of mixed ionic-electronic conduction (MIEC) is a wise approach to take advantage of the TPB concept [6-10]. Using MIEC electrodes, the electrochemical region of charge transfer spreads from the limited electrolyte/electrode interface to a much broader region. In

the vicinity of the electrolyte, conduction is predominantly ionic and relatively far from the electrolyte, it is predominantly electronic. Such ionic to electronic transformation occurs over a critical thickness. It is, thus, favorable that the electrode shows MIEC characteristics, at least over this critical thickness, which is on the order of a few to a few tens of microns [7]. This functional layer is normally referred to as an electroactive layer, electrocatalytic layer or interlayer.

With respect to electrode microstructure, a fine porous microstructure is required to increase the TPB and consequently to enhance the electrochemical reaction rate. On the other hand, since the gas species migrate diffusively, gas transport is markedly hindered by such a fine microstructure. Fortunately, a compromise is achievable by grading the electrode microstructure: a fine porous microstructure close to the electrolyte/electrode interface, where the electroactive layer is present, and a coarse porous microstructure away from this interlayer, as shown in Figure 1.2 [7,9].

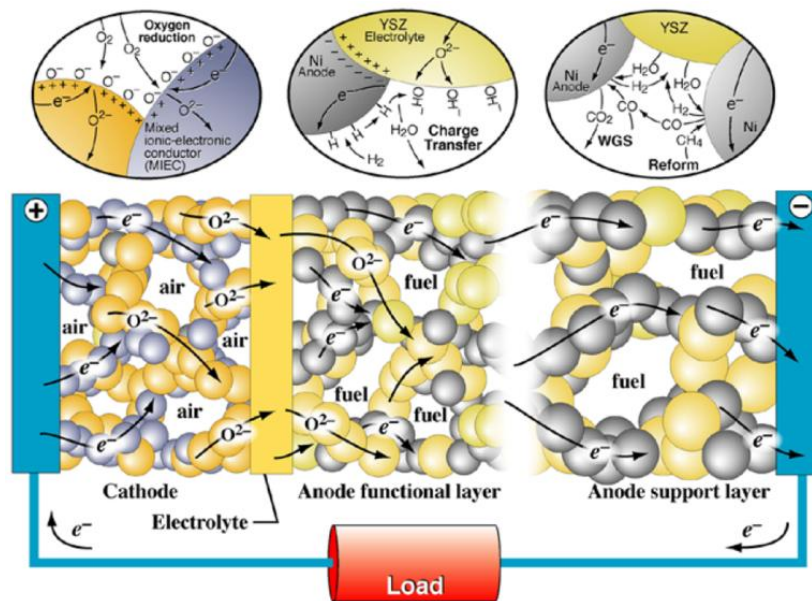


Fig. 1.2. Microscopic representation of an anode supported SOFC [9]

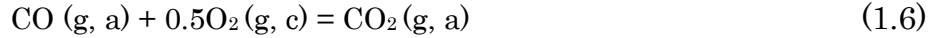
### 1.1.2.3. Thermodynamics of SOFCs

The maximum cell potential available from a fuel cell system occurs under open circuit condition. This equilibrium cell voltage is referred to as the Nernst potential and is expressed as

$$E_{rev} = -\frac{\Delta G^o}{n_e F} - \frac{RT}{n_e F} \ln \prod p_j^{v_j} \quad (1.5)$$

In this equation,  $\Delta G^o$  is the change in standard state Gibbs free energy associated with the oxidation reaction,  $n_e$  is the number of electrons involved in the electrode reactions (number of moles of oxygen required to oxidize one mole of fuel multiplied by four),  $F$  is Faraday's constant,  $R$  is the universal gas constant,  $T$  is the absolute temperature,  $p_j$  is the partial pressure of component  $j$  and  $v_j$  is the stoichiometric coefficient of component  $j$  (negative for reactants and positive for products).

As an example, if the oxidation of carbon monoxide is considered:



where  $a$  and  $c$  represent the anode and cathode, respectively, then the reversible potential is given as

$$E_{rev} = -\frac{\Delta G^o}{2F} - \frac{RT}{2F} \ln \frac{P_{\text{CO}_2,a}}{P_{\text{CO},a} \cdot P_{\text{O}_2,c}^{0.5}} \quad (1.7)$$

Note that the reversible potential is around 1.1 V under typical operating conditions of SOFCs [9].

### 1.1.2.4. Overpotential

The maximum electrical energy available from a fuel cell system is unachievable because of various internal losses at a given current density. These losses are normally referred to as voltage losses, overpotential or polarization. Based on their origins, there are three types of overpotential: ohmic ( $\eta_{\text{ohm}}$ ), concentration ( $\eta_{\text{con}}$ ), and activation

( $\eta_{act}$ ). The total polarization of a cell is  $\eta_{ohm} + \eta_{con} + \eta_{act}$ , which needs to be minimum so that an SOFC can operate efficiently.

The ohmic loss is related to the resistance of the cell components against electrical charge movements. Ionic conductivity of the electrolyte, electronic and ionic conductivity of the electrodes, and possible ohmic resistances associated with interfaces are the major parameters that determine the ohmic loss [12]. Since ionic conductivity of the electrolyte is much lower than electronic conductivities of the electrodes, ohmic loss is mainly due to the electrolyte. Using an electrolyte with greater ionic conductivity, such as doped ceria, and with lower thickness is a wise strategy to minimize this loss. Recently, electrode supported cells in which the electrolyte thickness is 5-30 microns have been preferable due to the high ohmic loss in electrolyte-supported cells.

In an SOFC system, since the reacting components are gaseous, they must be conveyed to the electrode/electrolyte interface (reaction zone) through the porous electrodes. “The physical resistance to the transport of gaseous species through the electrode at a given current density” [7] is referred to as concentration polarization. At a given current density, this type of voltage loss is fundamentally affected by several major parameters including the quantity, size and morphology of the electrode pores, the gaseous diffusivity, and the partial pressure of the gases [7,9,12]. Due to the fact that the binary  $H_2$ - $H_2O$  diffusivity is about 4-5 times higher than the binary  $O_2$ - $N_2$  diffusivity, and the partial pressure of hydrogen in the fuel is greater than that of oxygen in the oxidant, anodic concentration polarization is normally much less than on the cathodic side, when the thickness and microstructure of both electrodes are comparable [7].

As all chemical reactions involve energy barriers that must be overcome by the reactants, there is an activation barrier associated with electrode reactions. This activation barrier is the result of many complex electrochemical reaction steps where typically the slowest or rate-determining step is responsible for the activation polarization. Various researches have confirmed that the charge transfer reaction, as a fundamental step in electrode reactions, occurs at the TPB [7]. Therefore, electrode kinetics in general and activation polarization in particular, mainly depend on the TPB length. Electrocatalytic activity of the electrodes, partial pressure of the gases, and the reaction temperature are other significant parameters that can affect activation overpotential [7,9,12].

### 1.1.3. The development of anode materials

#### *1.1.3.1. Ni-YSZ anode materials*

To date, the most advanced SOFCs are clearly those based on Ni-YSZ composite anodes since they demonstrate long term stability, low overpotentials, high electrical and thermal conductivity, and excellent catalytic activity. In the cermet, Ni acts as an electronic conductor as well as a catalyst. The roles of YSZ, on the other hand, are to provide a structural support to suppress the sintering of Ni, to introduce the MIEC characteristics which have been discussed above, and to more closely match the thermal expansion of the anode to that of the other cell components.

The electrical conductivity of Ni-YSZ is greatly affected by its metal content. The threshold volume percent of Ni in the composite is about 30%. Below this value, the conductivity of the cermet is predominantly ionic which is associated with the YSZ phase [1,10]. In addition, the

particle size and distribution of both Ni and YSZ strongly affect the electrical conductivity of the Ni-YSZ composite as well as the threshold fraction of the metallic phase. In general, at the same Ni volume percent, the lower the Ni/YSZ particle size ratio, the greater the electrical conductivity of the composite [13].

Conventionally, the starting powders to make the Ni-YSZ cermet are NiO and YSZ. Exposed to the fuel, the NiO is subsequently reduced to nickel in situ. Since nickel metal is denser than nickel oxide, the initial volume of the nickel oxide is reduced by over 25% during the reduction process, leaving valuable porosity in the anode microstructure. The behavior of the anode is significantly dependent on the characteristics of the starting powders [13].

Performance degradation is a critical concern in long term operation of the Ni-YSZ based SOFCs. The major cause of such degradation is microstructural change due to Ni phase coarsening. It has been confirmed that this agglomeration is mainly because of the poor wettability of YSZ by nickel metal [13-15]. The sintering of Ni particles will result in the formation of isolated islands thus reducing the anode conductivity. Although optimization of the cermet microstructure can markedly address this problem, cell operation at high current densities and fuel utilization can still lead to Ni phase coarsening [14].

Although Ni-YSZ is still the most common anode material, particularly where hydrogen is the fuel, in addition to Ni agglomeration there are significant concerns associated with this cermet especially when more commercial fuels such as natural gas and synthesis gas are considered [7,10]. Impurities in these practical fuels even as low as a few ppm could severely degrade cell performance and affect its durability due to the great sensitivity of Ni to various impurities. The most prevalent

impurity which is unavoidably present in fuels like natural gas and synthesis gas is H<sub>2</sub>S [7]. Poisoning effects by other fuel impurities such as CH<sub>3</sub>SH, COS, NH<sub>3</sub> and Cl<sub>2</sub> are also of great concern [16]. Nickel is also renowned for its tendency to promote the buildup of carbon. This is another critical problem to be avoided since over time this can cause loss of cell performance and even failure [7]. Finally, since SOFCs are expected to go through several redox cycles during long term operation [17], the nickel phase can be oxidized. The dimensional changes associated with such an oxidation can cause performance loss.

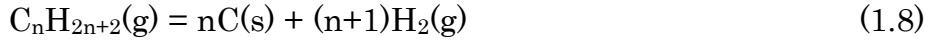
#### *1.1.3.2. Carbon deposition*

The ability to internally reform hydrocarbon fuels and to utilize the produced H<sub>2</sub> and CO, along with the possibility to directly utilize hydrocarbon fuels (direct oxidation), represents an exceptional advantage of SOFCs over other fuel cell systems. However, carbon deposition resulting from hydrocarbon pyrolysis is a serious problem associated with hydrocarbon fuels utilization [18,19]. Depending on the catalyst involved in cracking of the hydrocarbon, varieties of carbon can be formed [20] such as fibers, amorphous, and graphitic. While formation of carbon fibers is normally associated with separation of the catalyst from its support, amorphous carbon forms with no loss of the catalyst.

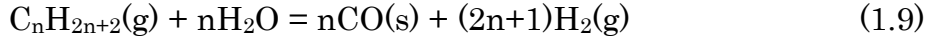
Nickel is an exceptional catalyst not only for cracking of methane and higher hydrocarbons, but formation of fibrous carbon [20]. The mechanism of carbon formation on nickel includes carbon deposition on the nickel surface, carbon dissolution into the nickel bulk and carbon fiber precipitation which leads to metal dusting [21]. This process results in loss of contact between the nickel catalyst and the ionically conductive support (YSZ) and, therefore, degradation of the

electrochemical performance [22]. In addition, the buildup of carbon leads to blocking of active sites on the anode resulting in more performance loss. Further carbon deposition eventually impedes the gas flow in the anode channels which can cause serious cell performance degradation and even failure.

The pyrolysis of hydrocarbons is based on the following general reaction:

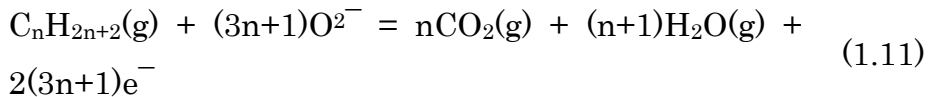
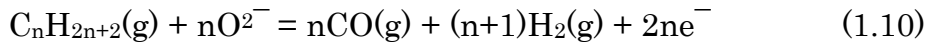


Adding steam to the fuel can suppress reaction (1.8) which is referred to as hydrocarbon steam reforming:



The steam reforming process can be performed either internally or externally. Obviously, internal direct reforming is preferable since it is more efficient and cost effective. However, there are several significant difficulties associated with such internal reforming, including the problem of sintering of the nickel particles in high steam partial pressures [7].

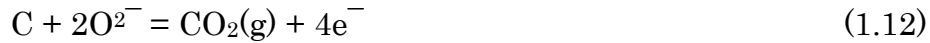
It is also possible to use hydrocarbon fuels directly, without any intermediate reforming stage. However, in the absence of a co-fed oxidant, it is challenging to hinder the buildup of carbon [6,7,11,14]. The direct oxidation of hydrocarbons occurs according to the following reactions:



The former, which is a partial oxidation reaction, is preferable due to the production of hydrogen and carbon monoxide [7]. The direct

oxidation of hydrocarbons is only possible if the anode is catalytically inactive toward carbon deposition [11].

Although promising results have been presented by researchers using ceria based materials [23,24], Mogensen and Kammer [20] argued that direct electrochemical oxidation of hydrocarbons on these materials does not occur at a reasonable rate. They further explained that the high performance of these anodes should be attributed to cracking of the hydrocarbon fuel on the metal catalyst followed by electrochemical oxidation of the cracking products:



Upon reduction, ceria can play a role as an oxygen donor and promote reaction 1.12 which not only prevents the buildup of carbon, but enhances the electrochemical performance.

Many attempts have been made to modify Ni-based anodes in order to overcome the challenge of incompatibility with hydrocarbon fuels. Liu and Barnett [25] showed that a conventional Ni-YSZ anode supported cell can be successfully operated on humidified methane and natural gas at low operating temperature (below 700°C) and high current density conditions. They, however, emphasized that at higher operating temperatures and under open circuit condition, carbon formation is seriously problematic. Kim et al. [26] tried to modify the nickel catalyst by alloying with copper. Their results indicate that whereas alloying suppresses carbon formation to a great extent, the electrochemical performance markedly decreases. Others [27,28] also reported stable performance in cells with Sn modified Ni-based anodes under hydrocarbon fuels. Furthermore, it has been shown that the addition of a trace amount of dopants such as Au, Cu, Ru and Mo into

nickel-based anodes can markedly improve the resistance to carbon deposition when the cell is operating at low oxidant to carbon ratios to decrease operating costs and to prevent sintering of the anode [7].

#### *1.1.3.3. Anode poisoning by fuel impurities*

As discussed previously, one of the greatest advantages of SOFCs over other fuel cells is fuel flexibility and the use of existing fuel infrastructure. In other words, a wide variety of fuels, including natural gas, coal gas, biogas, alcohol and gasoline, can be used besides hydrogen [16]. However, the presence of impurities in these practical fuels can strongly affect cell durability. Although they can be removed to a large extent by purification processes, identifying poisoning mechanisms by different impurities is essential to enhance the impurity tolerance of the anodes.

H<sub>2</sub>S is the most well-known impurity since it is unavoidably present in fuels such as natural gas, coal gas and biogas. Ni-based anodes are poisoned by H<sub>2</sub>S levels as low as 0.05 ppm. It has been revealed that sulfur poisoning of Ni-based anodes involves two different stages (Figure 1.3) [29]. At lower concentration of H<sub>2</sub>S (below 5 ppm), the interfacial adsorption of sulfur-based species on nickel, which is associated with a small voltage drop, is reversible (Figure 1.3(b)). In other words, upon injecting a sulfur-free fuel, the adsorbed components are eliminated and cell performance can be restored.

On the other hand, at higher concentrations of H<sub>2</sub>S, sulfur poisoning of the anode leads to a large fatal voltage drop which is no longer reversible. Comprehensive understanding of degradation mechanisms associated with sulfur poisoning at high levels of H<sub>2</sub>S is still in progress. Sasaki et al. [29] reported that Ni was oxidized to NiO (Figure 1.3(c)), which resulted in delamination of the anode layer from

the electrolyte due to the local volume change related to this oxidation. They emphasized that, particularly at lower concentrations of  $\text{H}_2\text{S}$  ( $\ll 10,000$  ppm), sulfur poisoning cannot be simply explained by Ni sulfide formation. However, Dong et al. [30] observed  $\text{Ni}_3\text{S}_2$  on a Ni-YSZ anode exposed to 100 ppm  $\text{H}_2\text{S}$ . They reasoned that even though the formation of a stable sulfide at this low level of  $\text{H}_2\text{S}$  could not be confirmed by thermodynamic calculations, it was reasonable for  $\text{Ni}_3\text{S}_2$  to form on Ni particles with nano-scale surface roughness. Also, it has been confirmed that sulfur tolerance of the anode is remarkably enhanced with temperature. This means that, at higher temperatures, the transition from reversible to irreversible poisoning happens at higher concentrations of  $\text{H}_2\text{S}$  [29-32].

Besides  $\text{H}_2\text{S}$ , other sulfur compounds such as COS and  $\text{CH}_3\text{SH}$  are also present as impurities in practical fuels. Both experimental studies and thermochemical calculations have revealed that almost all sulfur compounds present as impurities in fuels exist as  $\text{H}_2\text{S}$  at SOFC operating temperatures at equilibrium [16]. Therefore, the poisoning behavior by them is identical at least in the short term. However, more attention should be paid to the degradation behavior by sulfur compounds other than  $\text{H}_2\text{S}$  during long term operation [16].

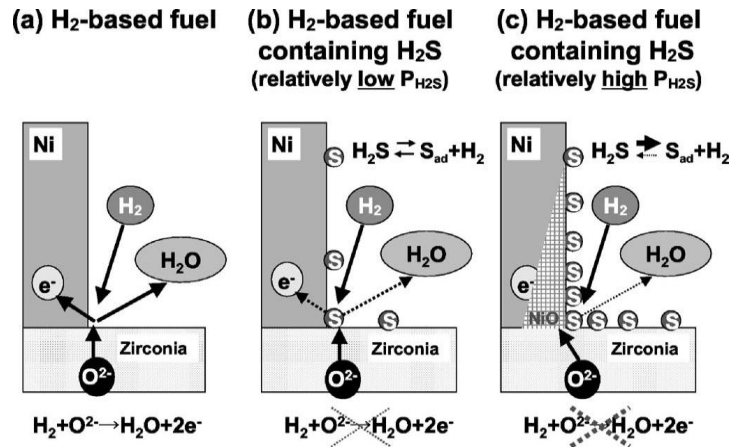


Fig. 1.3. Two different mechanisms of sulfur poisoning [29]

Another fuel impurity required to be considered is chlorine, which can easily react with Ni to produce NiCl<sub>2</sub> even when the concentration of Cl<sub>2</sub> is as low as 100 ppb [16]:



Degradation in cell performance is virtually undetectable when the fuel contains a low concentration of chlorine impurity (5 ppm for example). As the concentration of Cl<sub>2</sub> in the fuel increases, a constant rate of degradation in cell performance along with a remarkable change in the anode microstructure occur [16]. This significant microstructural change is essentially due to the low sublimation temperature of NiCl<sub>2</sub>.

#### *1.1.3.4. Alternative anode materials*

Recently, numerous studies have been undertaken with respect to alternative anode materials. These novel anodes can be basically categorized into two major groups: ceramic-metal composites and oxide ceramics. Direct modification of conventional Ni-YSZ anodes results in new cermet anodes. This can be achieved by a partial or total replacement of Ni with more impurity tolerant metals which have less propensity for carbon formation and/ or substitution of YSZ by new electrolyte materials with greater ionic conductivity and higher stability [32]. Ceria-based cermets are undoubtedly one of the strongest options. In a reducing atmosphere, ceria-based ceramics exhibit mixed ionic-electronic conductivity due to the reduction of CeO<sub>2</sub> to CeO<sub>2-x</sub>. Additionally, oxygen vacancy formation associated with such a reduction improves the prominent catalytic activity of ceria [9,13]. Ni-GDC (gadolinium-doped ceria), Ni-SDC (samarium-doped ceria), and Cu-GDC are some ceria-based cermets with promising performance [6,10,11,14,32]. Cermets such as Ni-SSZ (scandia-

stabilized zirconia), Ru-YSZ, Cu-YSZ, Cu-ceria-YSZ are among other materials with acceptable characteristics as an anode [13,14,32].

Oxide ceramics with both ionic and electronic conductivity at high temperature and in a reducing atmosphere are the other attractive group of alternative anode materials. Lower activation polarization, higher compatibility with the electrolyte, improved long term stability, and greater impurity tolerance and resistance to carbon deposition are the major advantages of single phase oxide anodes over cermets [10,32,33]. The most popular oxide anodes are titanium- and chromium-based perovskites. Lanthanum-strontium titanate (LST), in particular, is of great interest as an anode material due to its high electronic conductivity, stability in a reducing atmosphere and strong sulfur tolerance [31]. Strontium-doped lanthanum chromite is also attractive since it does not catalyze carbon deposition [33]. Also, because of its promising sulfur tolerance, strontium-doped lanthanum vanadate (LSV) has been recently considered; however, redox stability of LSV is a problem to be addressed [31,33]. Pyrochlore-type oxides, tungsten bronze-type oxides and bismuth oxide are among other materials studied as alternative anodes [33].

#### 1.1.4. Principles of ac impedance analysis

AC impedance spectroscopy is a non-destructive technique which is used for diagnosis and performance optimization in electrochemical devices. This powerful method provides information on individual polarizations including ohmic resistance, surface reactions, and mass transfer losses.

Electrochemical impedance theory is based on ac theory which shows the respond of a circuit to an alternating current or voltage as a

function of frequency. When a potential (voltage) is applied across an electrochemical device (such as a fuel cell), a current flows through the cell in response to the applied potential. The amount of this current is governed by the electrochemical processes taking place.

If the applied potential is sinusoidal ( $E(t) = E_m \sin(2\pi ft)$ ) then the subsequent current will also be sinusoidal ( $I(t) = I_m \sin(2\pi ft + \phi)$ ). The quotient of the applied potential divided by the current flow is known as the impedance, which is analogous to the resistance-current-potential relationship of a dc circuit. Normally, the expressions of voltage and current are converted from a time domain to a complex domain, in which  $E = E_{re} + E_{im} j$  and  $I = I_{re} + I_{im} j$ . Thus, the impedance can be defined as  $Z = E/I = Z_{re} + Z_{im} j$  in which the magnitude of the impedance is  $|Z| = \sqrt{(Z_{re}^2 + Z_{im}^2)}$  and the phase angle is  $\phi$ .

The plot of the real impedance ( $Z_{re}$ ) versus imaginary impedance ( $Z_{im}$ ) is called a Nyquist plot (or Cole-Cole plot). The major benefit of this plot is that the ohmic resistance and the polarization resistance can be easily read. Another popular way to present the impedance data is a Bode plot which shows the absolute value of the impedance and the phase angle as a function of frequency. To obtain more information from ac impedance analysis, it is most beneficial to present Nyquist and Bode plots together. Figure 1.4 shows an example of these two plots.

In a fuel cell, the shape of the impedance plot reflects different time dependent electrochemical processes which are strongly governed by parameters such as electrode material and composition, microstructure, temperature, and pressure and flow rate of gases. Therefore, the ac impedance method can be used to separately study these processes including ohmic losses, charge transfer at the

electrode/electrolyte interface, adsorption/desorption of the reactive species on the electrode, chemical reactions, and mass diffusion [34].

Often, to simulate these electrochemical processes, equivalent circuit models (ECM) are used. An example of a possible equivalent circuit for characterizing impedance is also shown in Figure 1.4. The most attractive feature of ECM as an impedance diagnosis method is that for each circuit element, there is a physical/chemical equivalent such as electrolyte resistance, charge transfer and mass transfer.

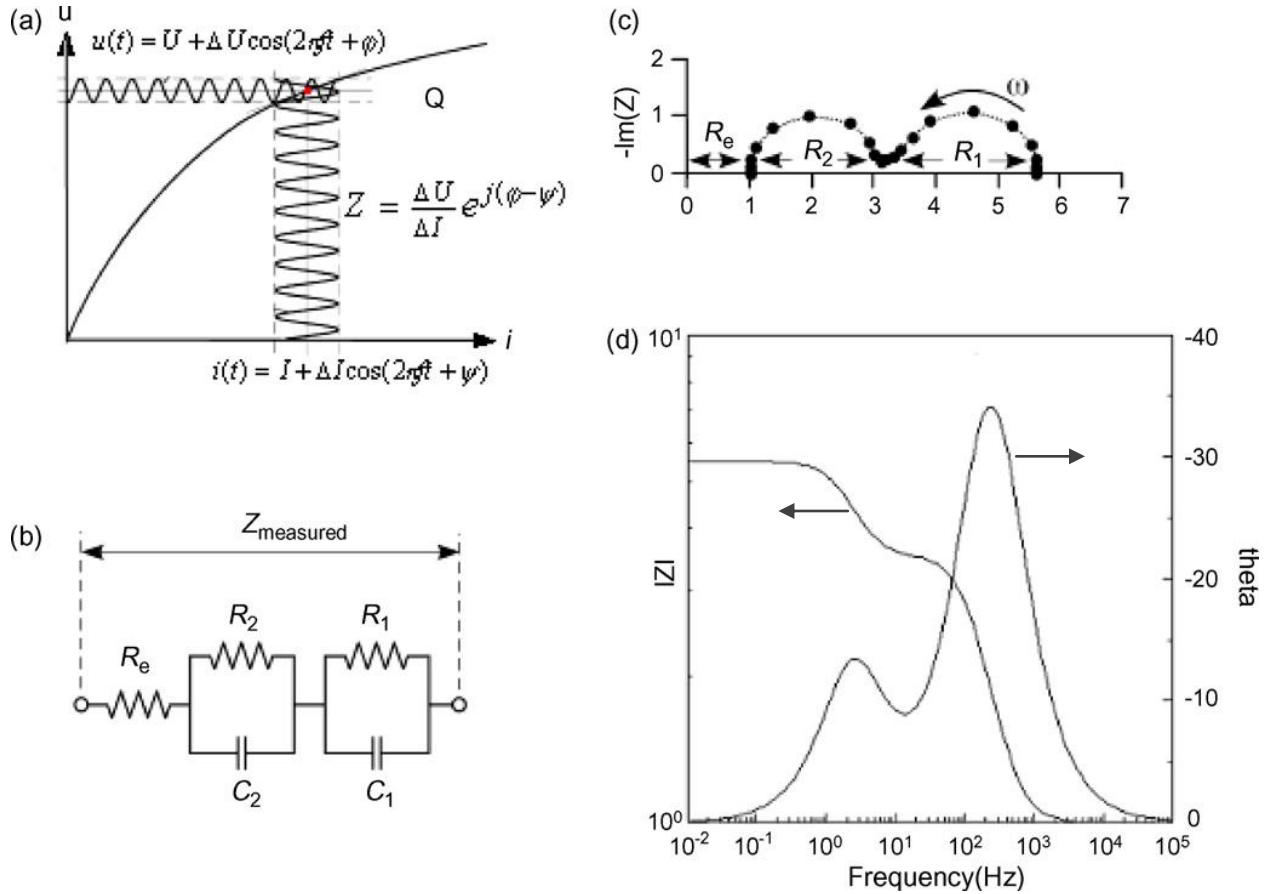


**Fig. 1.4.** Ac impedance analysis of an SOFC. (a) voltage-current dependence, (b) an equivalent circuit model, (c) Nyquist plot of impedance, and (d) Bode diagram of impedance [34].

It is noteworthy that ac impedance shows the average outcome of these electrochemical processes. It is possible, therefore, that cells with significantly different characteristics exhibit a virtually identical impedance plot! Therefore, it is important to use other analysis techniques along with the ac impedance method to obtain more reliable data and to interpret the results more precisely.

## **1.2. Research Motivations and Objectives**

In 1973, Levy and Boudart [35] showed the resemblance between Pt and tungsten carbide in surface catalysis. They suggested that such catalytic behavior in tungsten carbide which is not observed in tungsten metal is due to a modification in the electron distribution of tungsten by addition of carbon. Since then, the catalytic characteristics of Groups IV-VI carbides have been extensively studied. The fact that the catalytic attributes of these carbides are greatly similar to those of Pt-group precious metals is now well appreciated [36]. In particular, they have been very promising in reactions which deal with transformation of C-H bonds in hydrocarbons. Based on their precious metal-like catalytic behavior, molybdenum and tungsten carbide have recently been given a great deal of attention as electrocatalysts for low temperature fuel cells including proton exchange membrane (PEM) and direct methanol (DM) fuel cells [37-39]. They, however, have not been investigated to any great extent as alternative anodes for SOFC applications.

The characteristics of tungsten carbide are compared to those of nickel in Table 1.1. What has motivated us to study WC as an SOFC anode is its several compelling characteristics. First, the similar catalytic behavior between WC and precious metals is strongly intriguing. Second, in spite of being a ceramic, the electronic conductivity of

tungsten carbide is similar to that of metals (same order of magnitude as shown in Table 1.1). Third, the very high melting point of WC (2870°C) could reasonably guarantee long term microstructural durability at high operating temperatures. Fourth, as opposed to metals such as Ni and Cu, tungsten carbide is compatible with precious metals, which is indeed beneficial for boosting the catalytic activity toward hydrocarbon fuels. Finally, no carbon formation is expected on tungsten carbide under hydrocarbon fuels.

The purpose of this study is, thus, to investigate WC-based materials as potential alternative anodes for direct utilization of hydrocarbons in solid oxide fuel cells. The research objectives are as follows:

- To fabricate cells based on as-received WC powder and laboratory-made nano-sized WC powder
- To characterize the electrochemical behavior of half cells and full cells based on WC electrodes
- To analyze the electrochemical behavior of WC-based anodes
- To study the influence of active metal and oxide electrocatalysts on the electrochemical behavior of WC-based anodes
- To understand the challenges of WC-based anodes and to properly address them
- To develop a viable solid oxide fuel cell based on WC-based anodes capable of operating on methane fuel

**Table 1.1.** Physical properties of tungsten carbide and nickel

Property	WC	Ni
Density (g · cm <sup>-3</sup> )	15.6	8.9
Melting point (K)	3143	1728
Electrical conductivity at 800°C (S · cm <sup>-1</sup> )	3.8E4	2.4E4
Thermal expansion coefficient (10 <sup>-6</sup> · K <sup>-1</sup> )	6.9	13.4
Thermal conductivity (W · m <sup>-1</sup> · K <sup>-1</sup> )	121	90.9

### 1.3. Research Outline

The primary focus of the current work was to investigate tungsten carbide-based anodes for direct utilization of methane in solid oxide fuel cells. Considering the drawbacks of conventional WC-YSZ composites as anode materials, which are explained in detail later, it was necessary to develop a porous support into which the electrode functional materials are incorporated. The first part of this work (Chapter 2) is, therefore, focused on how the microstructure of the porous support affects the electrochemical performance of infiltrated electrodes in solid oxide fuel cells. Strontium doped lanthanum manganite ( $\text{La}_{0.8}\text{Sr}_{0.2}\text{MnO}_3$ , LSM) was chosen for two main reasons: it is a well-studied electrocatalyst cathode material, and it can be eventually used as the cathode for the rest of this study. Accordingly, Chapter 2 deals with impacts of porous support morphology on the electrochemical performance of symmetrical cells, based on LSM cathodes. With the total volume fraction of open porosity identically kept in the range of 50-55% for all the cells, the effect of size, connectivity and distribution of the pores on the ohmic and polarization resistance of the cathode was investigated using ac impedance spectroscopy.

The second part of this work (Chapter 3) is focused on electrochemical characterization of WC-based materials. In this chapter, first the electrochemical behavior of a conventional WC-YSZ composite and a carbide infiltrated porous YSZ support are studied under hydrogen, mixed hydrogen-methane and methane atmospheres. Second, the influence of ceria and/or Ru on the electrochemical performance of the carbide-based electrodes is investigated. Third, electrode performance stability is discussed based on a series of in-situ and ex-situ experiments. Finally, electrode reactions mechanisms are proposed.

The third part (Chapter 4) deals with preparation, electrochemical performance and challenges of fuel cells based on WC-based anode materials. This chapter starts with processing of solid oxide fuel cells based on either conventional WC-YSZ or WC infiltrated porous YSZ supported anodes and LSM infiltrated porous YSZ supported cathodes. Then the electrochemical performance of these conventional and infiltrated cells is compared, and the effect of ceria and Ru addition into the carbide-based anodes is described. Lastly, the implications of these results and the challenges of WC-based anodes are discussed.

The summit of this research is presented in the fourth part (Chapter 5), where the electrochemical performance of solid oxide fuel cells based on Ni-CeO<sub>2</sub>-WC-YSZ (NCWZ) composite anodes under methane fuels is investigated. First, the electrochemical behavior of NCWZ symmetrical cells toward methane under open circuit condition is researched. Next, the electrochemical behavior of a fuel cell based on Ni-CeO<sub>2</sub>-WC-YSZ anode/YSZ electrolyte/LSM-YSZ cathode is analyzed and the influence of Ni on the chemical stability of the carbide phase is discussed. Finally, the effect of oxidation-reduction-re carburization cycling on electrochemical performance and structural integrity of the cell is studied.

#### **1.4. Cell Fabrication Process**

In this work, symmetrical and full cell studies were carried out on both conventional and infiltrated cells. Although the fabrication process for each system will be explained in detail in each chapter, it is useful to give an overview of the cell fabrication processes in order to visualize the procedure. The schematic drawing in Figure 1.5 shows the fabrication processes. For the sake of simplicity, electrolyte supported cells were used in the entire work.

To prepare a conventional symmetrical cell (Fig. 1.5 (a)), thin WC-YSZ electrodes were symmetrically screen printed onto a YSZ electrolyte followed by sintering at 1300°C for 3 hr under a CO-CO<sub>2</sub> mixed atmosphere.

To prepare an infiltrated symmetrical cell (Fig. 1.5 (b)), thin calcined-based YSZ porous layers (CYSZ) were symmetrically screen printed onto a YSZ electrolyte followed by sintering at 1300°C for 3 hr in air. These CYSZ porous layers play a supporting role for the functional components such as electronic conductors and active catalysts. Ammonium metatungstate (AMT) solution was then symmetrically infiltrated into the porous support and heat treated at 880°C for 12 hr under a 80% H<sub>2</sub> – 20% CH<sub>4</sub> mixed atmosphere to create a nano-sized WC network over the support for both electrodes.

To prepare a conventional full cell (Fig. 1.5 (c)), a thin WC-YSZ anode was screen printed on one side of a YSZ electrolyte and a CYSZ porous layer was screen printed on the other side of the electrolyte disc. The cell was then sintered at 1300°C for 3 hr under a CO-CO<sub>2</sub> mixed atmosphere. The WC-YSZ anode layer was infiltrated with active electrocatalysts, if required. Finally, the porous CYSZ layer was infiltrated with a cathode solution to be heat treated in-situ.

To prepare an infiltrated full cell (Fig. 1.5 (d)), thin CYSZ porous layers were symmetrically screen printed onto a YSZ electrolyte followed by sintering at 1300°C for 3 hr in air. Ammonium metatungstate (AMT) solution was then infiltrated into a porous CYSZ layer (anode side) and heat treated at 880°C for 12 hr under a 80% H<sub>2</sub> – 20% CH<sub>4</sub> mixed atmosphere to create a nano-sized WC network within the support. The anode layer was infiltrated with other active electrocatalysts, if

required. Finally, the other porous layer (cathode side) was infiltrated with a cathode solution to be heat treated in-situ.

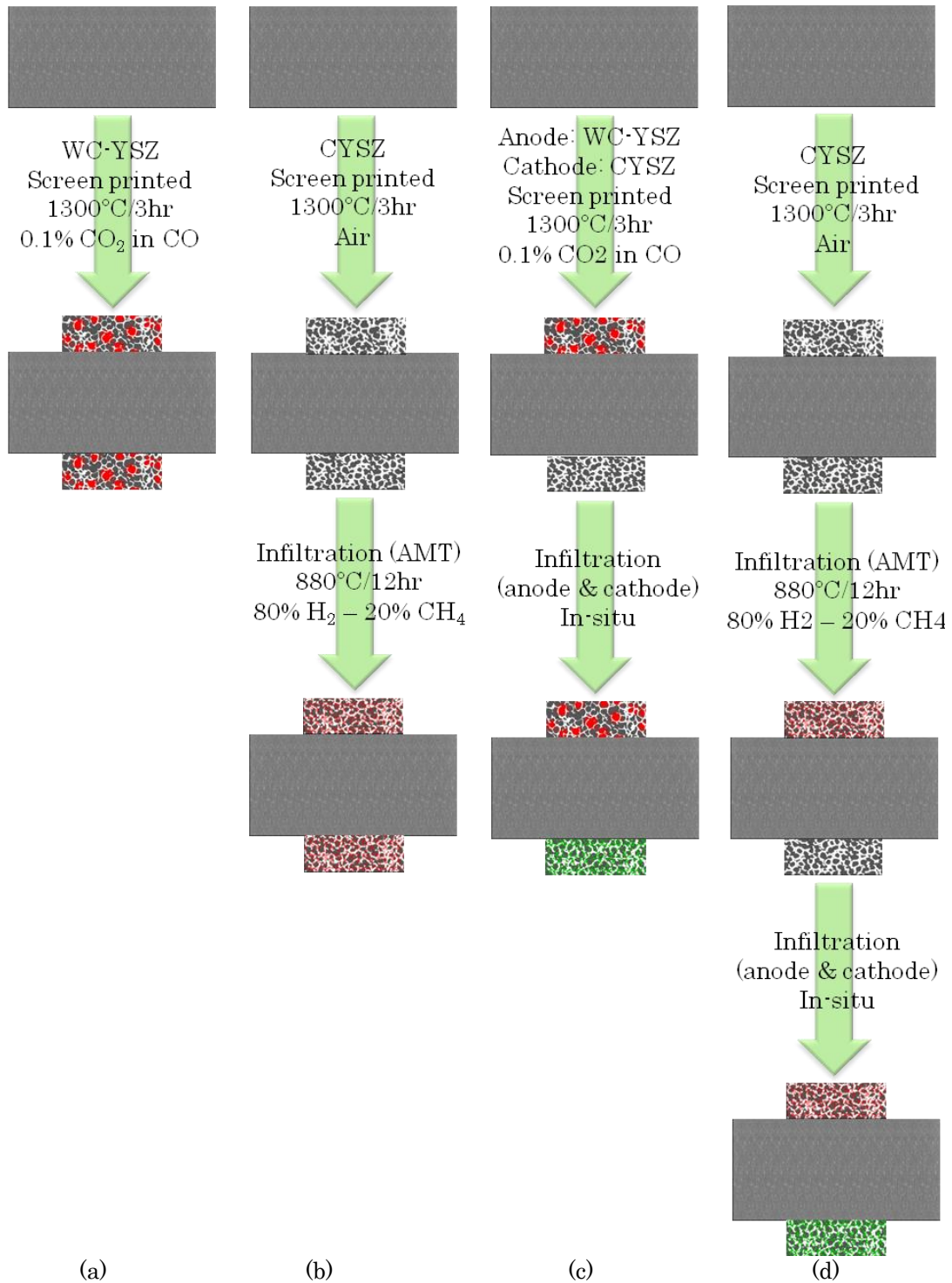


**Fig. 1.5.** Schematic cell fabrication procedure: (a) conventional symmetrical cell, (b) infiltrated symmetrical cell, (c) conventional full cell, (d) infiltrated full cell.

## References

- [1] N.Q. Minh, *J. Am. Ceram. Soc.* 76 (1993) 563.
- [2] B.C.H. Steele, A. Heinzl, *Nature* 414 (2001) 345.
- [3] J. Larminie, A. Dicks, *Fuel cell systems explained*, 2nd edition, John Wiley & Sons (2003).
- [4] O. Yamamoto, *Electrochim. Acta* 45 (2000) 2423.
- [5] F. Kreith, D. Y. Goswami, *Handbook of energy efficiency and renewable energy*, CRC Press (2007).
- [6] S. McIntosh, R.J. Gorte, *Chem. Rev.* 104 (2004) 4845.
- [7] S.C. Singhal, K. Kendall, *High temperature solid oxide fuel cells: fundamentals, design and application*, Elsevier, (2003).
- [8] R. J. Gorte, J. M. Vohs, *Annu. Rev. Chem. Biomol. Eng.*, 2 (2011) 9.
- [9] R.J. Kee, H. Zhu, A.M. Sukesini, G.S. Jackson, *Combust. Sci. and Tech.* 180 (2008) 1207.
- [10] C. Sun, U. Stimming, *J. Power Sources* 171 (2007) 247.
- [11] R.J. Gorte, J.M. Vohs, *J. Catal.* 216 (2003) 477.
- [12] F. Zhao, A. V. Virkar, *J. Power Sources* 141 (2005) 79.
- [13] S.P. Jiang, S.H. Chan, *J. Mat. Sci.* 39 (2004) 4405.
- [14] J.B. Goodenough, Y.H. Huang, *J. Power Sources* 173 (2007) 1.
- [15] D. Simwonis, F. Tietz, D. Stover, *Solid State Ionics* 132 (2000) 241.
- [16] K. Haga, S. Adachi, Y. Shiratori, K. Itoh, K. Sasaki, *Solid State Ionics* 179 (2008) 1428.
- [17] D. Sarantaridis, A. Atkinson, *Fuel Cells* 7 (2007) 246.
- [18] C.M. Finnerty, N.J. Coe, R.H. Cunningham, R. M. Ormerod, *Catal. Today* 46 (1998) 137.
- [19] R. Kikuchi, N. Koashi, T. Matsui, K. Eguchi, T. Norby, *J. Alloys Compd.* 408-412 (2006) 622.
- [20] M. Mogensen, K. Kammer, *Annu. Rev. Mater. Res.* 33 (2003) 321.

- [21] M.L. Toebes, J.H. Bitter, A.J.V. Dillen, K.P. de Jong, *Catal. Today* 76 (2002) 33.
- [22] M. D. Gross, J. M. Vohs, R. J. Gorte, *J. Mater. Chem.* 17 (2007) 3071.
- [23] J. Liu, B. D. Madsen, Z. Ji, S. A. Barnett, *Electrochem. Solid State Lett.* 5 (2002) A122.
- [24] R. J. Gorte, H. Kim, J. M. Vohs, *J. Power Sources* 106 (2002) 10.
- [25] J. Liu, S. A. Barnett, *Solid State Ionics* 158 (2003) 11.
- [26] H. Kim, C. Lu, W. L. Worrell, J. M. Vohs, R. J. Gorte, *J. Electrochem. Soc.* 149 (2002) A247.
- [27] E. Nikolla, J. Schwank, S. Linic, *J. Electrochem. Soc.* 156 (2009) B1312.
- [28] H. Kan, H. Lee, *Appl. Catal. B* 97 (2010) 108.
- [29] K. Sasaki, K. Susuki, A. Iyoshi, M. Uchimura, N. Imamura, H. Kusaba, Y. Teraoka, H. Fuchino, K. Tsujimoto, Y. Uchida, N. Jingod., *J. Electrochem. Soc.* 153 (2006) A2023.
- [30] J. Dong, Z. Cheng, S. Zha, M. Liu, *J. Power Sources* 156 (2006) 461.
- [31] S. Zha, Z. Cheng, M. Liu, *J. Electrochem. Soc.* 154 (2007) B201.
- [32] M. Gong, X. Liu, J. Trembly, C. Johnson, *J. Power Sources* 168 (2007) 289.
- [33] J.W. Fergus, *Solid State Ionics* 177 (2006) 1529.
- [34] Q. Huang, R. Hui, B. Wang, J. Zhang, *Electrochim. Acta* 52 (2007) 8144.
- [35] R. B. Levy and M. Boudart, *Science* 181 (1973) 547.
- [36] H. H. Hwu, J. G. Chen, *Chem. Rev.* 105 (2005) 185.
- [37] Y. Hara, N. Minami, H. Itagaki, *Applied Catalysis A* 323 (2007) 86.
- [38] D. J. Ham, Y. K. Kim, S. H. Han, J. S. Lee, *Catalysis Today* 132 (2008) 117.

[39] R. Ganesan, D. J. Ham, J. S. Lee, *Electrochem. Comm.* 9 (2007) 2576.

## Chapter 2

# Effects of Porous Support Microstructure on Performance of Infiltrated Electrodes in Solid Oxide Fuel Cells

### 2.1. Introduction

The first generation of SOFCs was developed based on electrolyte supported cells in the 1980s and 1990s [1]. Because of their high ohmic polarization, however, electrode supported cells have been given a great deal of attention in the last decade, as the second generation of SOFCs. Gorte et al. [2] and Sarkar et al. [3] have recently developed a newer generation of cells for planar and tubular designs, respectively, with a similar approach, in which a thick (hundreds of microns) porous YSZ support and a thin (tens of microns) dense YSZ electrolyte are co-fabricated and co-sintered. The porous support is then impregnated with either the anode or cathode of choice.

The recent approach has been given a great deal of attention in the last few years [4-8] and reviewed lately by Jiang [9] and Vohs and Gorte

[10]. This approach shows several promising features. One distinctive characteristic of porous YSZ supported cells is electrode material flexibility. Since the electron-conductive and catalyst components are to be infiltrated in a post-firing step, the impregnated phases no longer need to experience a high temperature treatment. Consequently, a broad range of materials can be considered including those which are prone to chemical reactions with YSZ at higher temperatures. Furthermore, a nano-sized electrocatalyst network could be obtained as a result of lower temperature treatment which contributes toward enhanced performance at lower operating temperatures [11]. Perhaps even more importantly, since the mechanical support and the electrolyte are based on an identical oxide and they are to be co-sintered at desirably high temperatures, a sharply noticeable interface between the support and the electrolyte is essentially eliminated and a well connected oxide network which is mechanically robust is developed [12,13]. Accordingly, superior thermal shock and redox cycling resistance is anticipated.

The significance of microstructure in solid oxide fuel cells has been clearly appreciated [14-17]. Pore size, pore volume fraction, three phase boundary length and tortuosity are considered as the most crucial microstructural parameters that greatly affect the electrochemical performance of SOFCs [17]. Boaro et al. [15] and Corbin et al. [18] showed that irrespective of the type of pore formers, they act as templates. They indicated that there was a direct correspondence between shape and size of the pore formers and those of the resulting pore former-based cavities. In addition, unless the volume fraction of the pore formers was high enough to reach the percolation threshold, pore former-based cavities could not be

interconnected. They, therefore, argued the role of interparticle-based channels in developing a well connected porous network.

Consequently, the morphology of the porous structure is essentially the key issue in development of porous supported cells. In this study, we report the impact of porous support morphology on the electrochemical performance of symmetrical cathode cells. With the total volume fraction of open porosity identically kept in the range of 50-55% for all the cells, the effect of size, connectivity and distribution of the pores on the ohmic and polarization resistance of the cathode was investigated using ac impedance spectroscopy.

## **2.2. Experimental Procedure**

Several different porous structures with the same volume fraction of open porosity but various morphologies have been developed. Table 2.1 shows the development of five different porous structures which were investigated in this study. The starting materials were YSZ (Tosoh TZ-8Y, Grove City, OH), polymethyl methacrylate (PMMA) (Microbeads®, Spheromers CA 6 (6  $\mu\text{m}$ ), Norway), carbon black (Alfa Aesar, average particle size: 42 nm), and graphite (Sigma Aldrich, <20  $\mu\text{m}$ ). The desired open porosity was chosen to be 50-55 vol.%. For all the samples, the amount of pore former and the sintering conditions were such that the desired open porosity could be obtained. To accurately measure the porosity with Archimedes method, YSZ pellets (diameter: 12 mm, height: 6 mm) were made by slip casting.

To prepare the CYSZ-P, as received YSZ was calcined at 1500°C for 3 hr and the calcined YSZ (CYSZ) was then ball milled for 72 hr. The microstructure of both as received and calcined YSZ powders was examined with a Philips Morgagni 268 transmission electron

**Table 2.1.** Characteristics of the porous structures studied.

Name	YSZ	Pore former (vol. %)			Sintering condition	Open porosity (%)
		PMMA-6	Carbon black	Graphite		
CYSZ-P	Calcined	20	0	0	1300°C/3hr	50-55
YSZ-P	As-received	50	0	0	1300°C/3hr	50-55
YSZ-C	As-received	0	50	0	1350°C/3hr	50-55
YSZ-PC	As-received	20	10	0	1200°C/3hr	50-55
YSZ-PG	As-received	20	0	10	1200°C/3hr	50-55

microscope (TEM). Particle size measurement was carried out by an ALV/CGS-3 Compact Goniometer System (ALV GmbH, Langen, Germany).

For the sake of simplicity, symmetrical electrolyte supported cells have been used. To prepare the YSZ pastes, YSZ powder and the proper amount of pore former (Table 2.1) were mixed in ethanol for 30 min using a planetary ball mill (Retsch, PM 100). After drying the mixed powder, a homemade ink ( $\alpha$ -terpineol + 5 wt% ethylcellulose) was added (10 g powder + 10 g ink) and they were well mixed in a mortar and pestle for 30 min. YSZ coatings (diameter: 10 mm, average thickness: 25  $\mu$ m) were then screen printed onto YSZ discs (FuelCellMaterials, Lewis Center, OH, diameter: 25 mm, average thickness: 0.3 mm) and sintered under the conditions mentioned in Table 2.1.  $\text{La}_{0.8}\text{Sr}_{0.2}\text{MnO}_3$  (LSM), as a well studied cathode material, was chosen to be impregnated into the porous YSZ structure.  $\text{Mn}(\text{NO}_3)_2 \cdot x\text{H}_2\text{O}$ ,  $\text{La}(\text{NO}_3)_3 \cdot 6\text{H}_2\text{O}$ , and  $\text{Sr}(\text{NO}_3)_2$  from Alfa Aesar were used as the starting precursors to prepare a solution based on Pechini's method [19]. The molar ratio of metal cations, complexing agent (citric acid) and ethylene glycol was chosen to be 1:4:4 in the solution. A small amount of the solution was dried and then heated to 700°C in air. The synthesized powder was examined by X-ray diffraction (XRD) that confirmed the presence of LSM as the only phase. The porous structure

was repeatedly impregnated by incipient wetness until 20 vol.% LSM was embedded into the YSZ network with the LSM phase to be formed in-situ. Finally, the cathode layer was coated with a laboratory-made gold paste as a current collector.

The electrochemical behavior of the cells was studied by ac impedance spectroscopy (Solartron frequency response analyzer 1255 in combination with a Solartron electrochemical interface 1287) on symmetrical cells with a four probe configuration. Impedance measurements were carried out under open circuit condition over a frequency range from 0.1 Hz to 100 kHz and a 10 mV ac perturbation. The microstructure of the porous structures before impregnation and after electrochemical testing were examined on fractured surfaces with a JEOL 6301F field emission scanning electron microscope (FE-SEM).

Finally, nitrogen adsorption/desorption isotherms at 77 K and surface area measurements on as received Tosoh YSZ, calcined and milled YSZ, and synthesized LSM powder were performed by Quantachrome Autosorb-1. Additionally, in order to quantitatively analyze the porous microstructures, surface area measurements and pore size distribution analysis were carried out on YSZ pellets before and after impregnation using the Brunauer-Emmett-Teller (BET) technique (nitrogen adsorption/desorption isotherms at 77 K). The samples were degassed at 250°C for two hours to remove physisorbed gases prior to the measurement. To get accurate BET results, the amount of samples was high enough so that a total surface area of 5-10 m<sup>2</sup> could be obtained. The BET experiment repeated three times to ensure the validity of the results and the reported numbers include the average and the standard deviation.

### 2.3. Results and Discussion

The straightforward approach to create a porous support is to use as received YSZ powder and an adequate amount of pore former. The microstructure of such a support (YSZ-P) is illustrated in Figure 2.1. Since this was based on as received YSZ and was to experience a 1300°C firing temperature, 50% PMMA pore former was needed to obtain the desired interconnected porous network. The specific surface area of this support was  $0.50 \pm 0.04$  m<sup>2</sup>/g. As illustrated in Figure 2.1, the porous network is made of one type of cavity which is based solely on the PMMA pore former. Here, 50 vol.% pore former virtually guarantees that the cavities remain connected. In addition, YSZ particles are well sintered and, therefore, isolated unless they are located in the vicinity of pore former-based cavities. The presence of these isolated YSZ particles in the support is undesirable since they are not able to play a role in electrochemical reactions.

A reasonable approach to avoid isolated YSZ particles is to reduce the sinterability of as received Tosoh YSZ powder by a calcination-milling process. The TEM micrographs of both as received and calcined and milled YSZ are illustrated in Figure 2.2, and the effect of such calcination is summarized in Table 2.2. As is clearly observed, YSZ

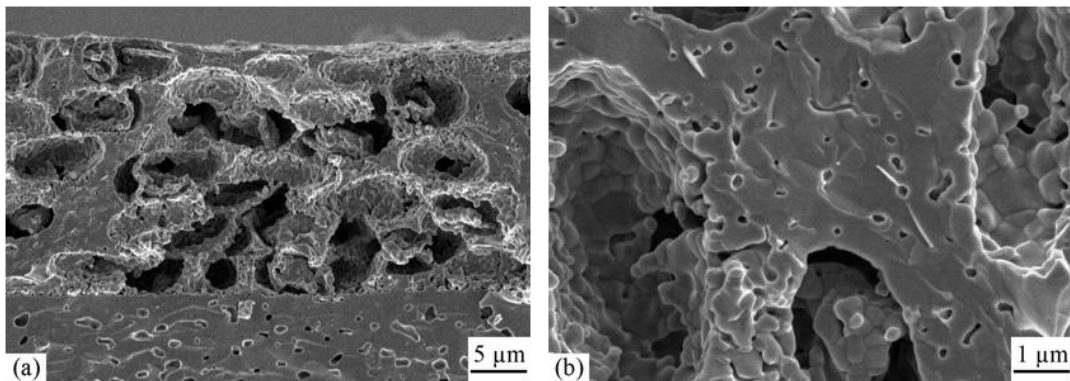


**Fig. 2.1.** SEM micrographs of YSZ-P.

experiences a considerable increase in particle size during calcination, which results in much lower sinterability. As has been discussed elsewhere [12], with no pore former, as received YSZ-based structures have no open porosity after sintering at 1350°C for 3 hr; however, 25-30% open porosity remains in calcined YSZ-based structures for similar sintering conditions. This simply means that to create a 50-55% porous structure, much less pore former is needed. Figure 2.3 shows the microstructure of CYSZ-P, the calcined YSZ-based structure with 20 vol.% PMMA. The specific surface area of such a porous support was  $0.91 \pm 0.02 \text{ m}^2/\text{g}$ . As opposed to YSZ-P, the porosity network is comprised of two types of pores: pore former-based and calcined-based. The former here is spherical with a diameter of about 5  $\mu\text{m}$ . There is essentially a direct correspondence between shape and size of the mono-size PMMA pore former and those of the pore former-based cavities [15]. The calcined-based, however, are randomly shaped submicron cavities between the calcined YSZ particles. Since the amount of pore former (20 vol.%) does not reach the percolation threshold in CYSZ-P, pore-former based cavities are mainly interconnected via calcined-based channels. Clearly, CYSZ-P has a very uniform microstructure in which both calcined particles and pores are well connected.

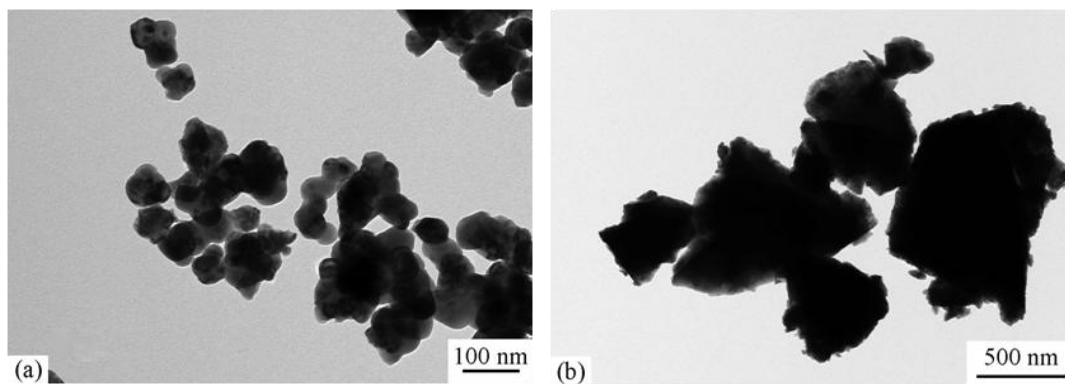


**Fig. 2.2.** TEM micrographs of (a) as received YSZ and (b) calcined and milled YSZ.

**Table 2.2.** Particle size and surface area of as received YSZ and calcined and milled YSZ powder.

YSZ	Mean particle size (nm)	Surface area (m <sup>2</sup> /g)
As received	250	12.3
Calcined & milled	750	3.2

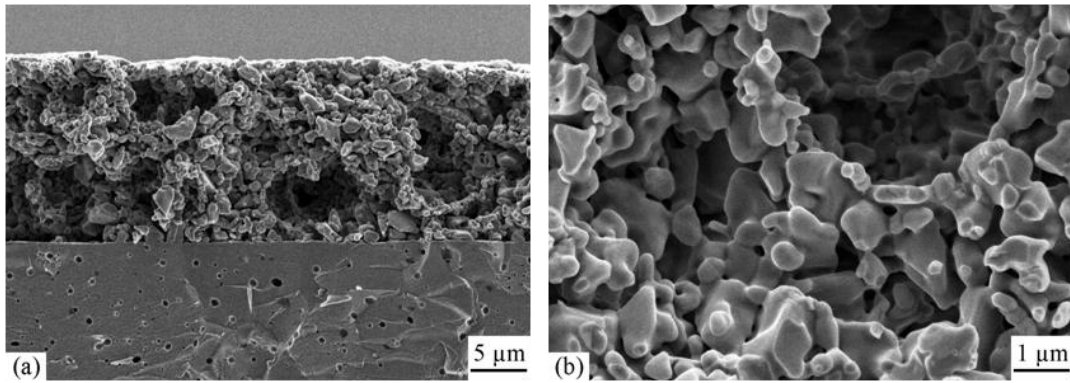


**Fig. 2.3.** SEM micrographs of CYSZ-P.

Another strategy to prevent YSZ particles from being isolated is using a pore former with a very high surface area. In YSZ-P, the size of the PMMA spheres is much larger than that of as received YSZ particles. Thus, there is a great possibility that YSZ particles become surrounded by other YSZ particles rather than cavities. The idea of using nano-sized carbon black instead of micron-sized PMMA was, therefore, to avoid YSZ particles being surrounded by each other and, consequently, to minimize fully isolated YSZ particles. Similar to YSZ-P, YSZ-C was based on as received YSZ and 50 vol.% pore former; however, carbon black instead of PMMA. Since the specific surface area of carbon black was considerably higher than that of as received YSZ (75 m<sup>2</sup>/g as opposed to 12.4 m<sup>2</sup>/g), thorough mixing resulted in YSZ particles well covered with carbon black. As a result, the sintering of this support was really challenging. At first, the porous support totally delaminated

from the electrolyte. To avoid such delamination, once the support was screen printed onto the electrolyte and dried, it was covered by 5 g of coarse calcined YSZ (not milled) powder. A 20 g alumina load was then put on the calcined powder and the support was sintered with such an arrangement. Although this addressed the delamination problem, the attachment between the electrolyte and the porous support was relatively poor. The specific surface area of this support was  $1.4 \pm 0.03$  m<sup>2</sup>/g. The microstructure of such a structure is shown in Figure 2.4. Again, there is just one type of pore based on carbon black pore former. The YSZ network is surrounded by well connected submicron- to micron-sized cavities; however, this structure is no longer based on individual YSZ particles but on YSZ agglomerates, which explains why YSZ-C had poor mechanical strength and weak attachment to the electrolyte.

The other possible approach to obtain a desirable morphology is to decrease the sintering temperature. 20-25% open porosity remained in an as received-based YSZ structure when the sintering conditions were 1200°C/ 3hr and the porous network was still well attached to the electrolyte. As received YSZ-based structures with 30 vol.% pore former and the low temperature firing profile, therefore, were

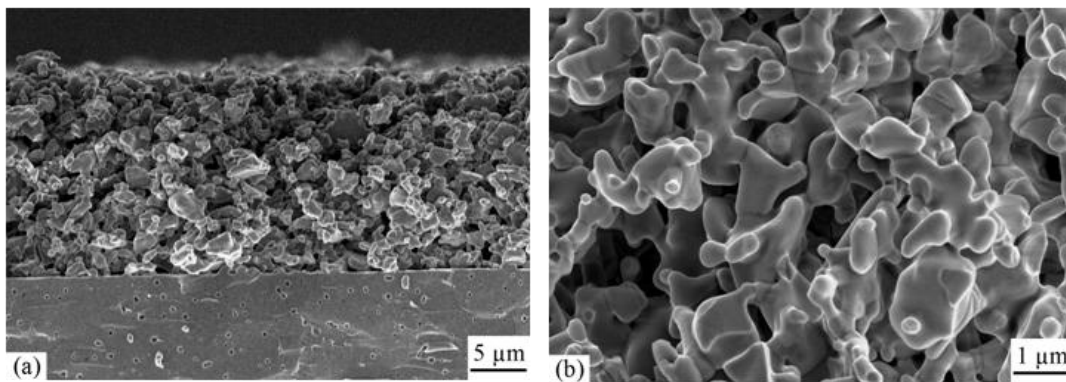


**Fig. 2.4.** SEM micrographs of YSZ-C.

interesting to study. Figures 2.5 and 2.6 illustrate YSZ-PC and YSZ-PG microstructures, respectively. They both are as received YSZ-based structures with 30 vol.% pore former: 20 vol.% PMMA + 10 vol.% carbon black in YSZ-PC and 20 vol.% PMMA + 10 vol.% graphite in YSZ-PG. The specific surface areas of such supports are  $2.81 \pm 0.02$  and  $2.19 \pm 0.03$  m<sup>2</sup>/g, respectively. Two types of pores are present in both YSZ-PC and YSZ-PG networks: micron-sized pore former-based and nano-sized interparticle-based. As can be seen in Figures 2.5 and 2.6, the distinct feature of YSZ-PG in comparison to YSZ-PC is the crossing effect of graphite-based void channels, which results in much better connectivity between pore former-based cavities.

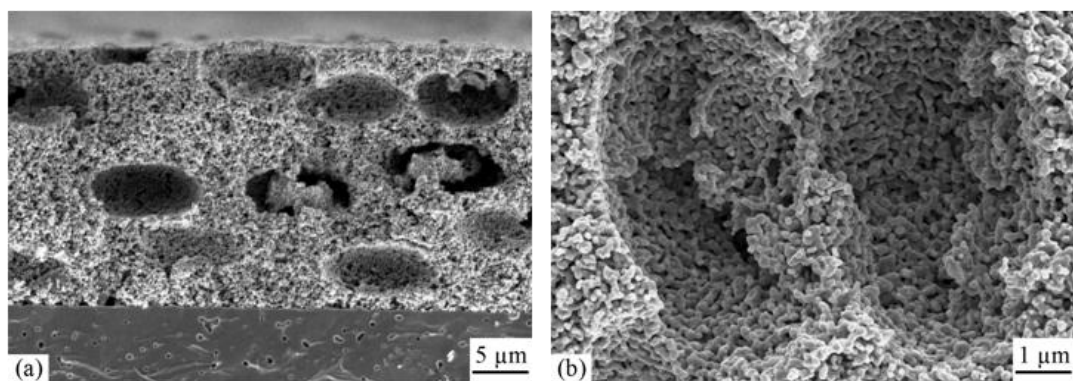


**Fig. 2.5.** SEM micrographs of YSZ-PC.

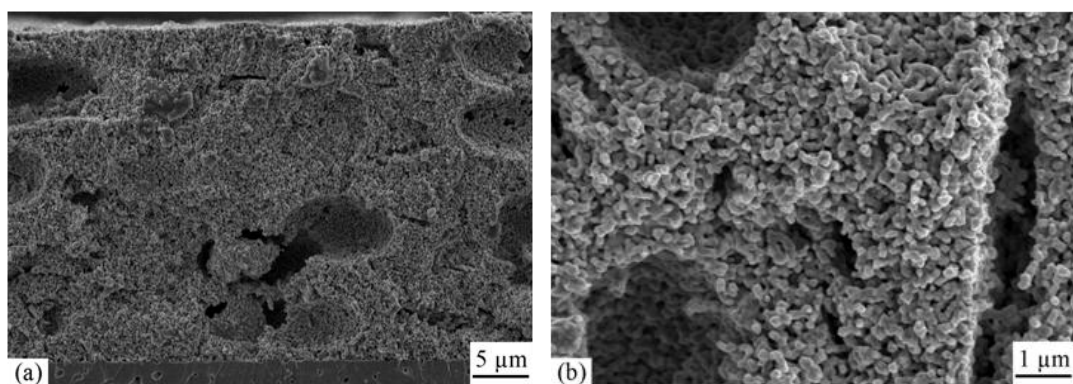


**Fig. 2.6.** SEM micrographs of YSZ-PG.

The 900°C and 800°C ac impedance spectra of these porous YSZ structures after impregnation with LSM are illustrated in Figure 2.7(a) and (b), respectively. This dramatically reveals the impact of the morphology of porous structures based on the large difference in electrochemical behavior among the cells. The impedance comprises two semicircles: a relatively large arc in the high-medium frequency range and a very small arc in the low frequency range. When J. D. Kim et al. [20] characterized the ac impedance behavior of LSM-YSZ composites, they showed that the impedance spectra were actually composed of three arcs: a high frequency arc, an intermediate frequency one and a low frequency semicircle. These arcs were attributed to oxygen ion transfer from the TPB to the electrolyte, oxygen ion surface diffusion along the LSM surface, and gas phase diffusion, respectively. Adler [21] also reported the same spectra components for LSC cathodes. Therefore, the observed large semicircle in the high-intermediate frequency range is a convoluted arc. Figure 2.7 clearly indicates that the high-medium frequency resistances were strongly dependent on morphology and temperature. The low frequency resistances, however, were relatively unchanged (about 10 m $\Omega$ ) and remained independent of morphology and temperature. This is understandable because gas diffusion limitation is not expected at normal oxygen partial pressure in air (0.2 atm) under OCV condition [22] and also gas phase diffusion is a low activation energy process [20]. Table 2.3 summarizes the ohmic and polarization resistances of the cells both at 900°C and 800°C. Temperature dependence of the area specific resistance (polarization or  $R_p$ ) of the LSM infiltrated CYSZ electrode is also shown in Figure 2.7 (c). Jiang [9] compared the electrode polarization of various cathodes at different temperatures and discussed that, at 700°C, the polarization of conventional LSM-YSZ and LSM-GDC electrodes were 2.5  $\Omega \cdot \text{cm}^2$  and 1.1  $\Omega \cdot \text{cm}^2$ ,

respectively. As illustrated in Figure 2.7(c), the polarization of the LSM infiltrated CYSZ electrode at 700°C is  $0.5 \Omega \cdot \text{cm}^2$  which is significantly lower than that of LSM-based electrodes reported by Jiang [9].

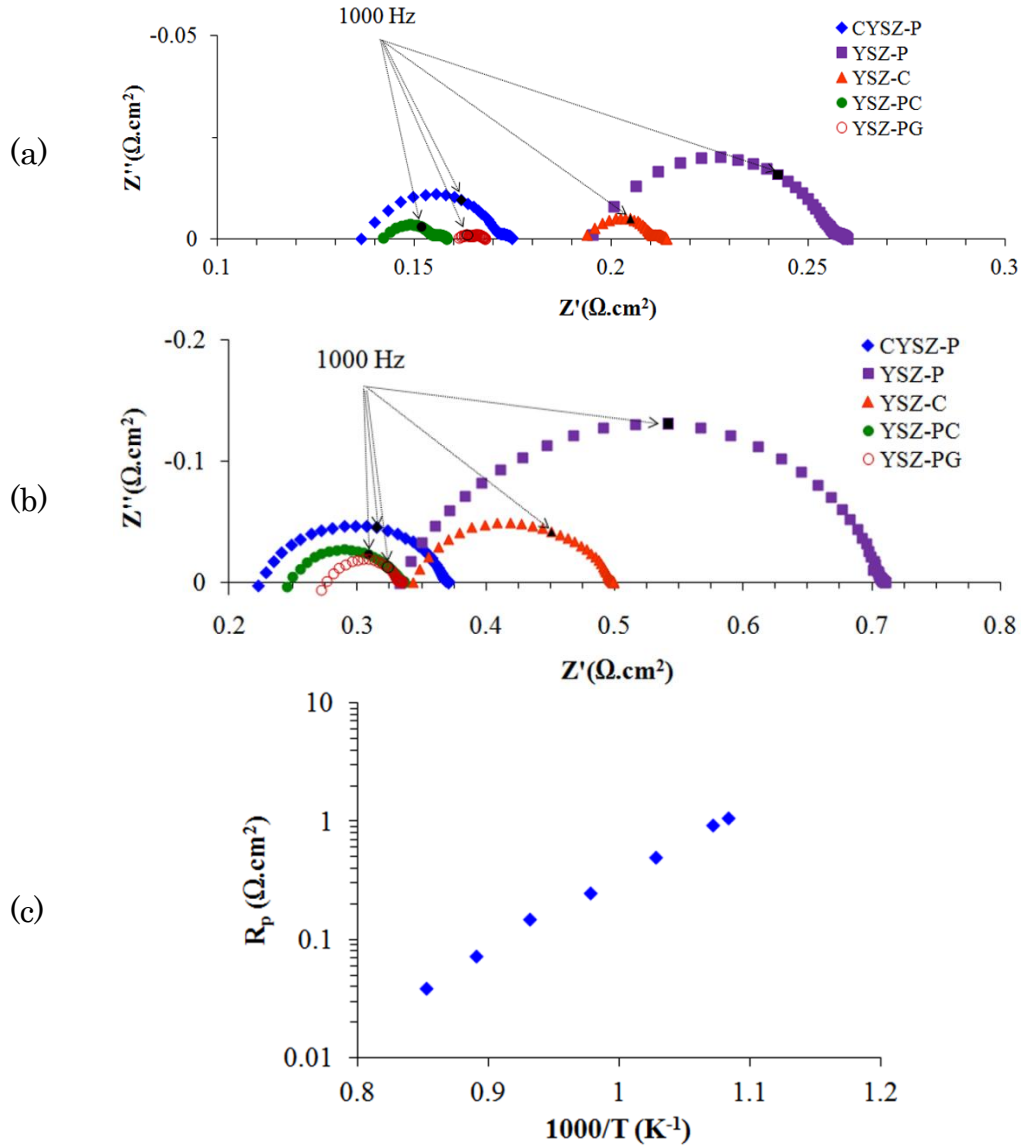


**Fig. 2.7.** (a) ac impedance spectra of the cells at 900°C, (b) ac impedance spectra of the cells at 800°C, and (c) area specific resistance (polarization) of CYSZ at different temperatures.

**Table 2.3.** Ohmic and polarization resistance of symmetrical cells.

Cell	900°C		800°C	
	$R_{\Omega}(\text{m}\Omega.\text{cm}^2)$	$R_p(\text{m}\Omega.\text{cm}^2)$	$R_{\Omega}(\text{m}\Omega.\text{cm}^2)$	$R_p(\text{m}\Omega.\text{cm}^2)$
CYSZ-P	135	38.5	224.5	147.5
YSZ-P	195	65	336.5	377.5
YSZ-C	192.5	21	341.5	156
YSZ-PC	141.5	16.5	247	89
YSZ-PG	161	7	275.5	60

For the sake of comparison, the specific surface areas of the studied porous supports before and after infiltration with LSM are summarized in Table 2.4. As qualitatively indicated by the SEM images, quantitative measurements of the surface areas based on BET theory accurately revealed that there is a sharp distinction among the supports. This information can be exploited to explain the different electrochemical behavior of the studied cells. Table 2.4 also includes the surface area of the supports after impregnation (the weight percentage of LSM in infiltrated YSZ pellets is included). As indicated, after impregnation the surface area is higher in all of the samples which implies that the impregnated LSM is highly porous in all cases. Huang et al. [23] have shown that depending on the calcination temperature, the morphology of the LSM coating could be different. While a porous LSM network can be obtained by lower temperature treatment, a dense coating formed at higher calcination temperatures.

**Table 2.4.** SSA of the porous structures before and after LSM infiltration.

Name	SSA ( $\text{m}^2/\text{g}$ )	Wt% of impregnated LSM	SSA after LSM impregnation ( $\text{m}^2/\text{g}$ )
YSZ-P	$0.50 \pm 0.04$	10.2	1.1
CYSZ-P	$0.91 \pm 0.02$	13.1	3.7
YSZ-C	$1.4 \pm 0.03$	11.3	3.2
YSZ-PC	$2.81 \pm 0.02$	10.5	4.5
YSZ-PG	$2.19 \pm 0.03$	9.7	3.9

The nitrogen adsorption/desorption isotherms of YSZ-P, CYSZ-P and YSZ-PG before and after impregnation are shown in Figure 2.8(a) and (b), respectively. The latter shows a higher level of nitrogen adsorption in both cases. Before infiltration of LSM, the isotherms of YSZ can be classified as type II in accordance with the IUPAC classification [24]. Such a reversible isotherm is the typical one obtained by a macroporous support. After impregnation, however, the isotherms can be classified as type IV with a type H4 hysteresis characteristic associated with narrow slit-like pores. This behavior which was observed in all the studied supports simply means that infiltration introduces mesoporosity into the macroporous supports. As will be illustrated later, the SEM studies show that these slit-like mesopores are located within the nano-sized LSM network.

The Barrett-Joyner-Halender (BJH) method can be used to calculate the pore size distribution. Figure 2.9(a) shows the cumulative pore volume distribution which is linked to the volume occupied by pores as a function of their size and Figure 2.9(b) shows the corresponding differential plots which are linked to the number of pores with a given size for YSZ-P, CYSZ-P and YSZ-PG before and after impregnation. As observed earlier (Figures 2.1 and 2.3-6), two types of pores are present in the supports (micron-sized pore former-based and submicron-sized interparticle-based) which both can be categorized as macropores (more than 50 nm). Because of the limitation of the BJH method which works best for mesoporous materials, the micron-sized pore former-based porosity which is directly dependent on the shape and size of the pore former is not included in the illustrated pore size distribution. Moreover, since the interparticle-based cavities are mostly more than 50 nm, they also cannot be considered as mesopores. That is why the volume occupied by mesopores (2-50 nm) is not

considerable (Figure 2.9(a)). Nevertheless, it is interesting that in all of the LSM infiltrated supports, a relatively sharp peak appears (Figure 2.9(b)) in the mesopore region and as a matter of fact such mesoporosity causes the appearance of a hysteresis loop in the adsorption/ desorption isotherms of infiltrated supports (Figure 2.8) [25]. The peak corresponds to 3.8 nm pores for all of the LSM impregnated samples. This means that the mono-sized mesopores are located between the LSM nanoparticles.

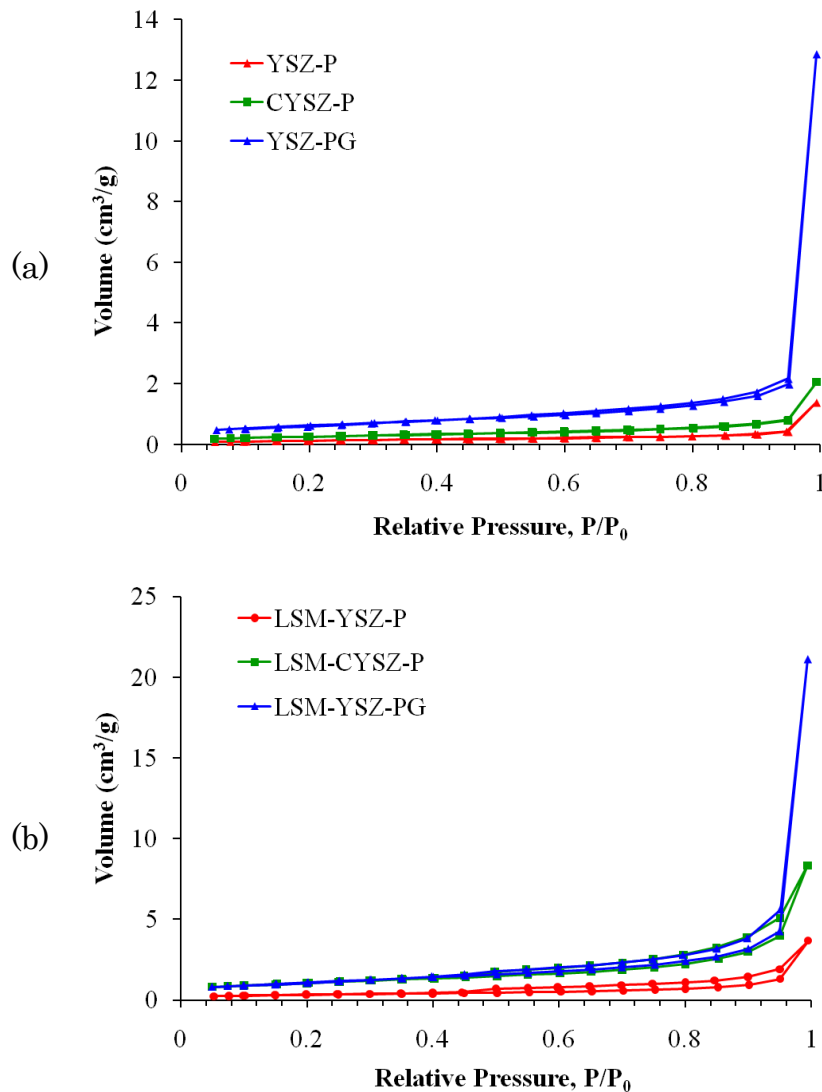


**Fig. 2.8.** Adsorption/desorption isotherms of YSZ-P, CYSZ-P and YSZ-PG (a) before and (b) after LSM impregnation.

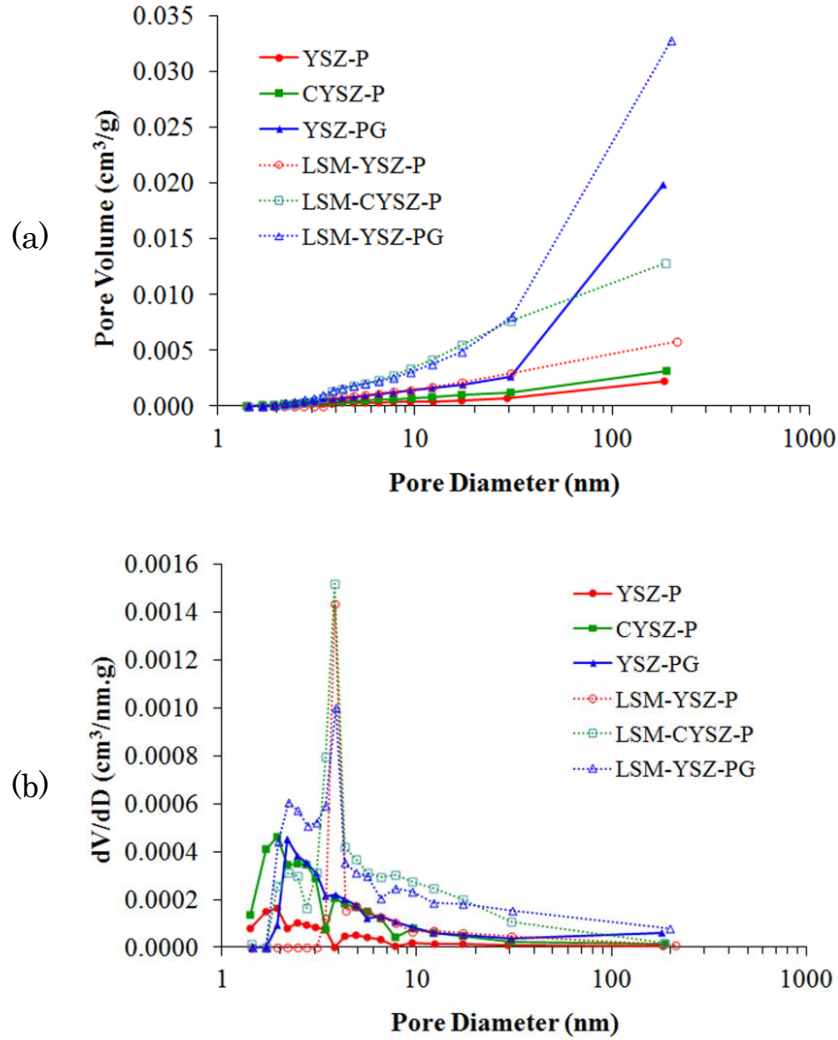


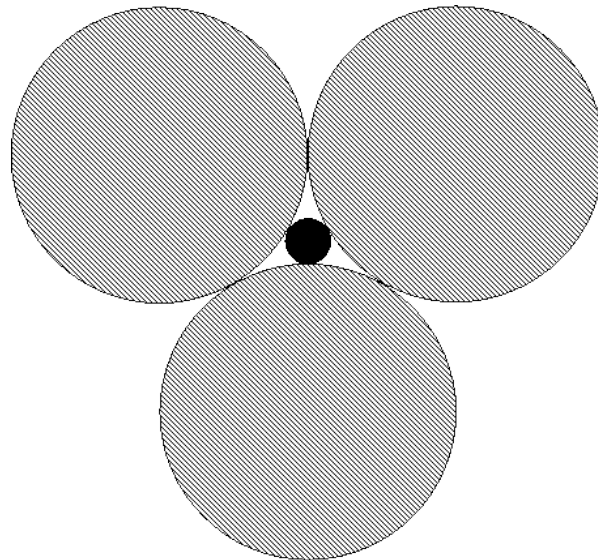
**Fig. 2.9.** BJH pore size distribution of YSZ-P, CYSZ-P and YSZ-PG before and after LSM impregnation: (a) cumulative pore volume distribution and (b) differential pore volume distribution.

To further investigate the LSM-based mono-sized mesopores, the LSM powder was separately synthesized with exactly the same solution used for the infiltration and the same heat treatment profile. The BET measurement revealed that the specific surface area of the synthesized LSM nano-powder was 23 m<sup>2</sup>/g. This can be converted to equivalent particle size according to the following equation:

$$D_{\text{BET}} = 6000/\rho_{\text{LSM}} \cdot S_{\text{BET}} \quad (2.1)$$

where  $D_{\text{BET}}$  is the average particle diameter in nm,  $\rho_{\text{LSM}}$  is the density of LSM in  $\text{g}/\text{cm}^3$  and  $S_{\text{BET}}$  is the specific surface area in  $\text{m}^2/\text{g}$ . Thus the calculated average particle size of the LSM would be about 40 nm. Assuming that the LSM nanoparticles are all mono-sized half spheres and their arrangement on the surface of the support is closed packed, one can calculate the size of the mono-sized cavities between the nanoparticles (Figure 2.10). For 40 nm LSM particles the calculated pore size would be about 6 nm which is in reasonable agreement with the measured mesopore size (3.8 nm).

In order to analyze the electrochemical behavior of the cells, the microstructure of the LSM impregnated YSZ network had to be closely investigated. These are shown in Figure 2.11(a) to (e).



$$x = \left( \frac{2\sqrt{3}}{3} - 1 \right) r$$

**Fig. 2.10.** Schematic illustration of LSM half spheres closed-packed arrangement (the dashed circles are monosized LSM particles with a radius of  $x$  and the black circle is the interparticle cavity with a radius of  $r$ .)

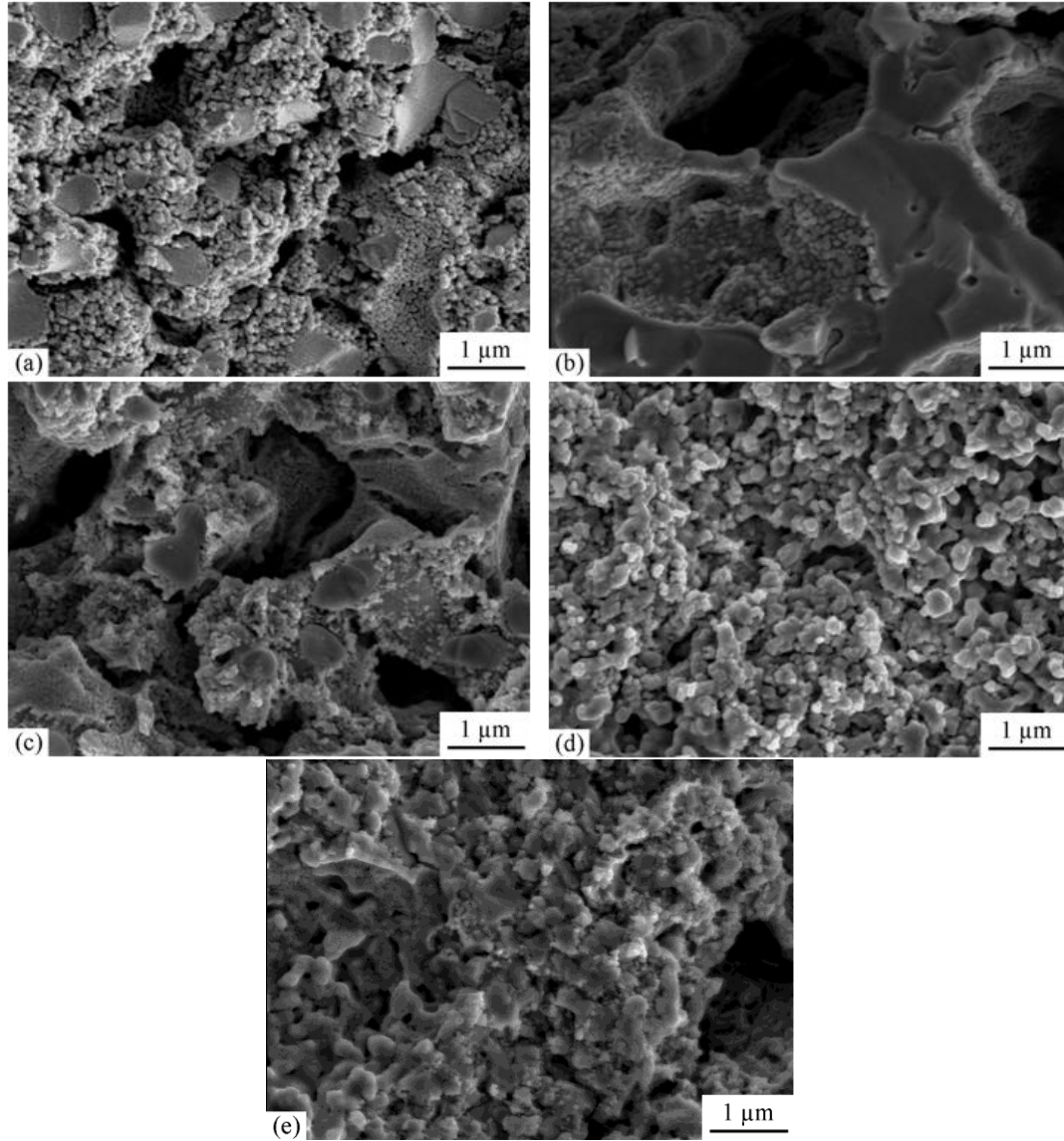


**Fig. 2.11.** SEM micrographs of LSM impregnated porous YSZ structures: (a) CYSZ-P (b) YSZ-P (c) YSZ-C (d) YSZ-PC and (e) YSZ-PG.

In CYSZ-P, the LSM nanoparticles are homogeneously distributed throughout the YSZ network and they are well connected (Figure 2.11(a)). However, in YSZ-P, although the cavities are well covered with LSM nanoparticles, isolated YSZ particles which are fully sintered are essentially LSM free (Figure 2.11(b)). As discussed earlier, such a support has the lowest surface among them all (Table 2.4). Therefore, three phase boundaries (TPBs), where the ion-conducting

phase (YSZ), the electron-conducting phase (LSM) and the gas phase (oxygen) coexist, are minimal in this type of structure. Since the oxygen reduction reaction predominantly occurs at TPBs in LSM-based cathodes [1,10,11], such morphology leads to the greatest polarization resistance. In addition, since the ionic conductivity of YSZ is considerably lower than the electronic conductivity of LSM, the morphology is responsible for the higher ohmic resistance in YSZ-P.

As illustrated in Figure 2.11(c), the LSM nanoparticles uniformly cover the YSZ agglomerates in YSZ-C. As indicated in Table 2.4, the specific surface area of such a support is higher than that of CYSZ-P which results in a larger TPB length once the support is infiltrated with the LSM electrocatalyst. A lower polarization resistance is then expected for YSZ-C in comparison with CYSZ-P, which is not the case here. Additionally, the ohmic resistance of YSZ-C is the highest of all. As discussed earlier, because of very high surface area of the pore former, the attachment between the electrolyte and the porous support and also between the YSZ agglomerates were relatively weak. This basically increases the interfacial polarization and deteriorates the electrochemical performance.

The very low polarization resistance in the low temperature sintered cells (YSZ-PC and YSZ-PG) is also the inevitable corollary of TPBs (Figure 2.11(d) and (e)). Lower temperature treatment of the cells results in a much finer YSZ network. This simply means that there is more YSZ surface area available to be covered by LSM (already confirmed by BET measurements). The amount of TPBs is, therefore, much greater than high temperature treated cells, which is basically responsible for the lower polarization resistance. Figure 2.12 shows a PMMA-based cavity in both YSZ-PC (a) and YSZ-PG (b). As the microstructures indicate, the pore wall is LSM free in YSZ-PC, but well

covered with LSM in YSZ-PG. Since the interparticle cavities are nano-sized and essentially not much larger than LSM particles, they are greatly prone to be blocked by infiltrated LSM particles. This could be the case for both YSZ-PC and YSZ-PG cells; however, the presence of graphite-based planar cavities in the latter, which are much larger than LSM particles, can effectively address the blocking issue. Therefore, although the original surface area of the YSZ-PC support is higher than that of YSZ-PG, the readily available surface area of YSZ-PC is not necessarily higher because of the blocked cavities. That is why YSZ-PC shows a higher polarization resistance in comparison with YSZ-PG.

As shown in Figure 2.7, the ohmic resistance of the low temperature sintered cells is higher than CYSZ-P. To cast light on this, two higher magnification micrographs of CYSZ-P and YSZ-PG are shown in Figure 2.13. Since the YSZ surface area is much lower in CYSZ-P, for the same volume fraction of LSM, multilayers of LSM particles cover the YSZ network (Figure 2.13(a)); in YSZ-PG, there is much more YSZ surface area available and multilayer coverage is not observed (Figure 2.13(b)). Such multilayer LSM coverage leads to the lower ohmic resistance in CYSZ-P.

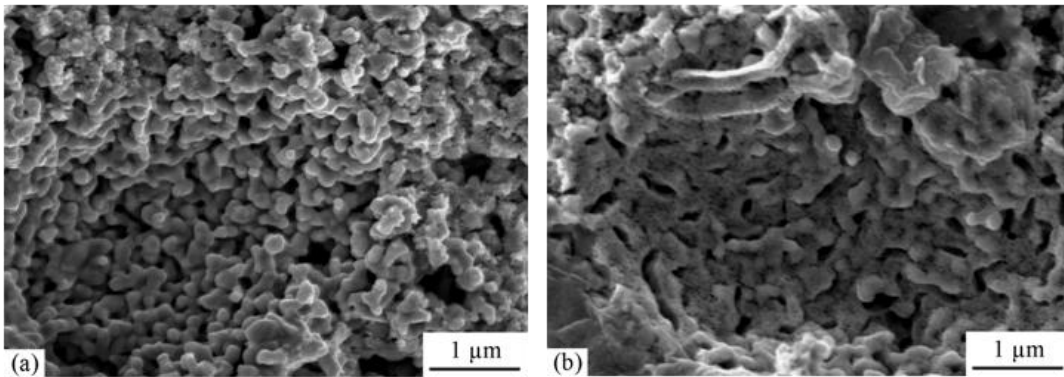


**Fig. 2.12.** SEM micrographs of (a) YSZ-PC showing an LSM-free PMMA-based cavity and (b) YSZ-PG showing a PMMA-based cavity covered with LSM nanoparticles.

Since the LSM phase was developed in-situ and the maximum treatment temperature had been set at 900°C, it was also worth studying the stability of the cells and observing whether the morphology would have an impact on the stability. Figure 2.14(a) shows how the ac impedance spectra of CYSZ-P and YSZ-PG change within a 72 hr period at 800°C. The increase in ohmic resistance is 2.5% and 3.3% for CYSZ-P and YSZ-PG, respectively, which most likely has to do with sluggish sintering of gold particles in the current collector film. The increase in polarization resistance was only 2.7% for CYSZ-P, while that for YSZ-PG was 9.1%. The variation in polarization resistance of these cells is illustrated Figure 2.14(b). This implies that although both cells are reasonably stable, the calcined YSZ-based cell showed greater stability.

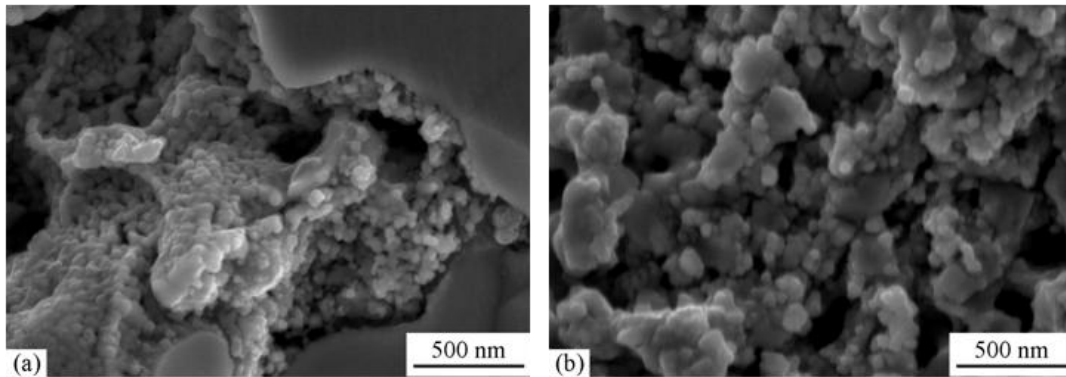


**Fig. 2.13.** SEM micrographs of (a) CYSZ-P showing a multilayer LSM coverage and (b) YSZ-PG showing no multilayer LSM coverage.

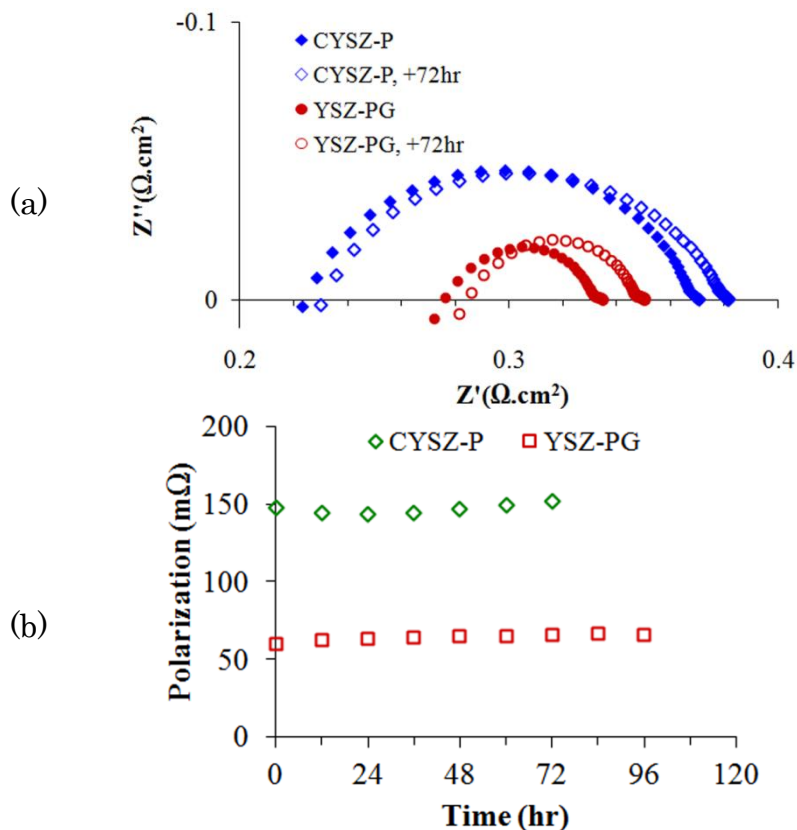


**Fig. 2.14.** (a) ac impedance spectra of CYSZ-P and YSZ-PG at 800°C within a 72 hr period and (b) stability of CYSZ-P and YSZ-PG.

Although the importance of the role of TPB in the electrochemical behavior of SOFCs has been reported [17], how the morphology of the porous YSZ network could affect the surface area of the support and, therefore, the three phase boundary length is definitely one of the more significant outcomes of this study. As was indicated by BET analysis and confirmed by SEM studies, the LSM nanoparticles can be reasonably assumed to be mono-sized half spheres with closed packed arrangement on the surface of the support. Making such an assumption and knowing the specific surface area of the YSZ support as well as the LSM powder, one can calculate the weight percentage needed for a monolayer LSM coverage on the YSZ supports. Table 2.5 shows the calculated amount of LSM required for a monolayer

coverage. Not only does such information give a reasonable estimate of how much infiltration is needed, but it also can provide new insights into the potential TPB length for each support which is also listed in Table 2.5. Considering the fact that the amount of LSM in the symmetrical cells was 20 vol.% which corresponds to 28 wt.%, the comparison between the ratio of specific surface areas (or TPBs) and that of polarization resistances is interestingly informative.  $S_{\text{BET,CYSZ-P}}:S_{\text{BET,YSZ-P}}$ ,  $S_{\text{BET,YSZ-PG}}:S_{\text{BET,YSZ-P}}$  and  $S_{\text{BET,YSZ-PG}}:S_{\text{BET,CYSZ-P}}$  are 1.82, 4.38 and 2.41, respectively (Table 2.4). Comparably,  $R_{\text{p,YSZ-P}}:R_{\text{p,CYSZ-P}}$ ,  $R_{\text{p,YSZ-P}}:R_{\text{p,YSZ-PG}}$ , and  $R_{\text{p,CYSZ-P}}:R_{\text{p,YSZ-PG}}$  are 2.56, 6.29 and 2.46, respectively (Table 2.3, 800°C). The reason that YSZ-C and YSZ-PC were not included in this comparison is that they, as explained earlier, do not follow the expected trend. This argument makes better sense when the SEM images of these impregnated supports are compared (Figure 2.11 (a), (b) and (e)). The important outcome of such an argument is that when infiltration of a support is considered, specific surface area of the support can give reasonable insights about the TPBs and, consequently, the electrochemical performance of a cell. Having the highest specific surface areas, low temperature sintered YSZ cells provide the most populated TPBs especially along the interface. Thus low temperature treatment of the porous YSZ structure would bring about the lowest polarization resistance. It is noteworthy, however, that in practice, cells are not mechanically supported by the electrolyte, but by the porous YSZ network. This means that cells eventually have to experience sintering above 1300°C not only to obtain a mechanically robust porous support, but also to yield a gas-tight thin electrolyte; therefore, a calcined YSZ-based porous support would remain the best practical alternative!

**Table 2.5.** Calculated amount of LSM required for a monolayer coverage and the corresponding TPB length.

Name	SSA of YSZ support (m <sup>2</sup> /g)	SSA of synthesised LSM (m <sup>2</sup> /g)	Calculated LSM needed (wt%)	Calculated TPB length (m/g)
YSZ-P	0.50 ± 0.04	23	6	5×10 <sup>7</sup>
CYSZ-P	0.91 ± 0.02	23	12	9.1×10 <sup>7</sup>
YSZ-C	1.4 ± 0.03	23	18	1.4×10 <sup>8</sup>
YSZ-PC	2.81 ± 0.02	23	36	2.81×10 <sup>8</sup>
YSZ-PG	2.19 ± 0.03	23	28	2.19×10 <sup>8</sup>

Moreover, since the porous YSZ support is to be impregnated by the electron-conducting phase and the catalyst phase (if different from the electron-conducting phase), not only does the connectivity of the pores matter, but the size of the cavities is also important. In as received YSZ-based structures treated at lower temperatures, YSZ particles are in the submicron range and the majority of interparticle cavities caused by particle bridging are essentially nano-sized. Even using nano-sized carbon black pore former to increase the size of the interparticle channels is not a successful approach. These nano-sized cavities, therefore, are prone to be blocked by impregnated materials. This leads to a non-homogenous microstructure. Although using planar-shaped graphite pore former could address the issue to some extent, uniformity would still remain a concern in such fine porous supports. The presence of submicron-sized calcined-based cavities in the CYSZ network, however, could reasonably guarantee a uniform post-infiltration structure.

## 2.4. Conclusions

The following conclusions could be drawn from the current study:

- I. The morphology of the porous YSZ network greatly affects the surface area of the support, density of the three phase boundary and, therefore, electrochemical performance of the cells.
- II. The calcined YSZ-based support showed a very uniform microstructure both before and after LSM infiltration. The submicron calcined-based cavities guaranteed a homogenous distribution of a mesoporous LSM network. LSM infiltration introduced a very narrow monomodal mesoporosity (about 4 nm) and therefore, LSM nanoparticles were reasonably estimated to be mono-sized (about 40 nm).
- III. The specific surface area of a support and the configuration of LSM nanoparticles can give reasonable insights about the TPBs and, consequently, the electrochemical performance of a cell.
- IV. Having the largest specific surface areas, lower temperature treated supports with an as received YSZ-based structure (YSZ-PC and PG) performed with the lowest polarization resistance. However, the calcined YSZ-based impregnated support had the lowest ohmic resistance.

## References

- [1] S. C. Singhal and K. Kendall, High temperature solid oxide fuel cells: fundamentals, design and applications, p. 42, Elsevier Ltd., Oxford U.K. (2003).
- [2] R. J. Gorte, S. Park, J. M. Vohs and C. Wang, Adv. Mater. 12 (2000) 1465.
- [3] P. Sarkar, L. Yamarte and G. Amow, Proc. 2009 CF/DRDC International Defence Materials Meeting, p. 55, Victoria, BC, Canada (2009).
- [4] M. Shah and S. A. Barnett, Solid State Ionics 179 (2008) 2059.
- [5] Z. Liu, Z. W. Zheng, M. F. Han and M. L. Liu, J. Power Sources 195 (2010) 7230.
- [6] T. Z. Sholklapper, V. Radmilovic, C. P. Jacobson, S. J. Visco and L. C. De Jonghe, Electrochem. Solid-State Lett. 10 (2007) B74.
- [7] Y. Huang, J. M. Vohs and R. J. Gorte, Electrochem. Solid-State Lett. 9 (2005) A237.
- [8] T. Z. Sholklapper, C. Lu, C. P. Jacobson, S. J. Visco and L. C. De Jonghe, Electrochem. Solid-State Lett. 9 (2006) A376.
- [9] S. P. Jiang, Mater. Sci. Eng. A 418 (2006) 199.
- [10] J. M. Vohs and R. J. Gorte, Adv. Mater. 21 (2009) 943.
- [11] T. Z. Sholklapper, H. Kurokawa, C. P. Jacobson, S. J. Visco and L. C. De Jonghe, Nano Lett. 7 (2007) 2136.
- [12] A. R. Hanifi, A. Torabi, T. H. Etsell, L. Yamarte and P. Sarkar, Solid State Ionics 192 (2011) 368.
- [13] A. R. Hanifi, A. Shinbine, T. H. Etsell and Partha Sarkar, Int. J. Appl. Ceram. Technol., DOI: 10.1111/j.1744-7402.2011.02617.x (2011).
- [14] N. Q. Minh, J. Am. Ceram. Soc. 76 (1993) 563.
- [15] M. Boaro, J.M. Vohs and R.J. Gorte, J. Am. Ceram. Soc. 86 (2003) 395.

- [16] M. Brown, S. Primdahl and M. Mogensen, *J. Electrochem. Soc.* 147 (2000) 475.
- [17] J. R. Smith, A. Chen, D. Gostovic, D. Hickey, D. Kundinger, K. L. Duncan, R. T. DeHoff, K. S. Jones and E. D. Wachsman, *Solid State Ionics* 180 (2009) 90.
- [18] S. F. Corbin, J. Lee and X. Qiao, *J. Am. Ceram. Soc.* 84 (2001) 41.
- [19] M. P. Pechini, U.S. Patent No. 3,330,697 (1967).
- [20] J. D. Kim, G. D. Kim, J. W. Moon, Y. I. Park, W. H. Lee, K. Kobayashi, M. Nagai and C. E. Kim, *Solid State Ionics* 143 (2001) 379.
- [21] S. B. Adler, *Solid State Ionics* 111 (1998) 125.
- [22] S. Primdahl and M. Mogensen, *J. Electrochem. Soc.* 146 (2000) 2827.
- [23] Y. Huang, J. M. Vohs, R. J. Gorte, *J. Electrochem. Soc.* 152 (2005) A1347.
- [24] K. S. W. Sing, D. H. Everett, R. A. W. Haul, L. Moscou, R. A. Pierotti, J. Rouquerol and T. Siemieniewska, *Pure Appl. Chem.* 57 (1985) 603.
- [25] I. M. Hung, D. T. Hung, K. Z. Fung and M. H. Hon, *J. Europ. Ceram. Soc.* 26 (2006) 2627.

## Chapter 3

# Electrochemical Behavior of Tungsten Carbide-based Materials as Candidate Anodes for Solid Oxide Fuel Cells

### 3.1. Introduction

To date, the most advanced SOFCs are clearly those based on Ni-YSZ composite anodes [1-3] since they demonstrate exceptional catalytic activity under hydrogen fuels and excellent electrical and thermal conductivity. In the cermet, Ni is an electrocatalyst for hydrogen oxidation which simultaneously provides electronic conductivity. The roles of YSZ, on the other hand, are to introduce oxygen ionic conductivity throughout the composite anode, to provide a structural support to suppress the sintering of Ni, and to better match the thermal expansion of the composite anode to that of other cell components.

Compared to other fuel cell systems, one of the exceptional advantages of solid oxide fuel cells is the ability to internally reform hydrocarbon

fuels and then utilize the produced  $H_2$  and CO as well as the possibility to directly burn hydrocarbon fuels (direct oxidation) [4]. However, carbon deposition resulting from competitive catalytic cracking of hydrocarbon is a serious problem associated with Ni-based anodes and hydrocarbon fuels [5]. Not only does the buildup of carbon fibers lead to blocking of active sites on the anode resulting in a loss of cell performance, but also the formation of carbon fibers detaches Ni from the support and degrades the microstructure [6].

In addition to carbon deposition, performance degradation is also a critical concern in long term operation of Ni-YSZ based SOFCs. The major cause of such degradation is microstructural change due to Ni phase coarsening. It has been confirmed that this agglomeration is mainly because of the poor wettability of YSZ by nickel metal [7,8]. The sintering of Ni particles will result in the formation of isolated islands and thus reduce the anode conductivity. Although optimization of the cermet microstructure can markedly address this problem, cell operation at high current densities and fuel utilization can still lead to Ni phase coarsening [2].

In 1973, Levy and Boudart [9] showed the resemblance between Pt and tungsten carbide in surface catalysis. Since then, many attempts have been made to investigate the catalytic characteristics of Groups IV-VI carbides. It is now well established that the catalytic attributes of these carbides are greatly similar to those of Pt-group precious metals [10], particularly in reactions which deal with transformation of C-H bonds of hydrocarbons. Particularly, molybdenum and tungsten carbide have been given a great deal of attention as electrocatalysts for low temperature fuel cells including proton exchange membrane (PEM) and direct methanol (DM) fuel cells [11-13]. However, to the best of the

authors' knowledge, they have not been deeply investigated as a possible anode material for SOFCs

In 1996, Naoumidis et al. [14] reported the utilization of WC-YSZ as an anode material for SOFCs. They showed that a carbide-based anode could potentially perform better than a Pt anode under 90% CO – 10% CO<sub>2</sub> as a fuel. Although they discussed that oxidation of the carbide phase could be a problematic issue, they claimed that the carbide phase is thermodynamically stable at  $CH_4/H_2O > 0.2$  and concluded that a reasonable yield of oxidation products can be achieved with carbide-based anodes. Cheng et al. [15] studied the stability of a variety of metal carbides as sulphur resistant anodes for SOFCs. They discussed that most of the metal carbides could not be considered as potential anodes for SOFC application simply because the corresponding oxides were much more stable under typical SOFC anode atmospheres. The only exception, however, were W and Mo carbides.

What has motivated us to study WC as an SOFC anode is its compelling characteristics. Firstly, the catalytic resemblance between this carbide and precious metals is strongly intriguing. In addition, in spite of being a ceramic, the electronic conductivity of tungsten carbide is similar to that of metals ( $0.52 \times 10^5 \text{ S} \cdot \text{cm}^{-1}$  for WC vs.  $1.43 \times 10^5 \text{ S} \cdot \text{cm}^{-1}$  for Ni). Furthermore, the very high melting point of WC (2870°C) could potentially guarantee the long term microstructural stability at high operating temperatures. Finally, no carbon formation is expected on tungsten carbide under hydrocarbon fuels. In this study, therefore, we report the electrochemical behavior of WC-based electrodes under mixed hydrogen-methane and methane fuels and subsequently discuss the potential advantages and challenges.

### 3.2. Experimental Procedure

The tungsten carbide (WC) used in this study was obtained from Inframat Advanced Materials, Manchester, CT (nanocrystalline tungsten carbide powder, 99.95%, particle size: 200 nm, crystal size: 40-70 nm). The yttria stabilized zirconia (YSZ) was supplied by FuelCellMaterials, Lewis Center, OH (yttria stabilized zirconia 8 mole%, fine grade (YSZ8-U1), particle size: 300-500 nm). In order to prepare conventional WC-YSZ composites, 7.26 g of the carbide and 2.74 g of the oxide (equal volume percentage of WC and YSZ) were put in a 50 mL polypropylene jar. 10 g of zirconia balls (Tosoh YTZ grinding media, 3 mm) and 10 mL ethanol were added and they were mixed for an hour at 500 rpm using a planetary ball mill (Retsch, PM 100). The WC-YSZ mixture was dried and the dried agglomerates were manually ground in an alumina mortar and pestle.

To prepare symmetrical cells, YSZ discs (FuelCellMaterials, Lewis Center, OH, diameter: 25 mm, average thickness: 0.3 mm) were used as the electrolyte as well as the mechanical support. A homemade ink ( $\alpha$ -terpineol + 5 wt% ethylcellulose) was added to the mixed powder (10 g powder + 10 g ink) and they were well mixed in a mortar and pestle for an hour. WC-YSZ electrodes (diameter: 10 mm, average thickness: 25  $\mu$ m) were then symmetrically screen printed onto the discs. The coated discs were dried at 150°C for 30 min and sintered at 1350°C for 3 hr under different atmospheres which will be discussed later.

To investigate how other active electrocatalysts can promote the electrochemical performance of WC-YSZ cells, they were infiltrated with ceria and/or Ru. A 0.25M solution of cerium ammonium nitrate (Alfa Aesar) in ethanol was prepared as a precursor for ceria. The WC-YSZ support was infiltrated with the ceria solution using a micro-

syringe and subsequently dried at 150°C for 15 min followed by a heat treatment at 350°C for another 15 min. To obtain 10 wt% ceria, the infiltration-heat treatment cycle was repeated 10 times. Similarly, a 0.1 M solution of  $\text{RuCl}_3 \cdot x\text{H}_2\text{O}$  ( $x \leq 1$ ) (Sigma-Aldrich) in ethanol was prepared. The support was then impregnated by this solution using a micro-syringe and dried at 150°C for 15 min. The impregnation was repeated 5 times and the final Ru gain was about 3 wt%.

In this study, the behavior of WC infiltrated YSZ porous supports was also investigated. The preparation procedure of such porous YSZ supports was explained in detail elsewhere [16]. Briefly, calcined-milled YSZ (CYSZ) was used as the starting material to make the support. To prepare the CYSZ, as received YSZ (Tosoh TZ-8Y, Grove City, OH) was calcined at 1500°C for 3 hr and the calcined YSZ was then ball milled for 72 hr. 20 vol.% polymethyl methacrylate ((PMMA), Microbeads®, Spheromers CA 6, Norway) was added to CYSZ powder as a pore former. This exact procedure was followed to make electrolyte supported symmetrical cells. These cells were then sintered at 1300°C for 3 hr in air. For these cells, ammonium metatungstate was used (Informat Advanced Materials, Manchester, CT) as the starting precursor to prepare a solution based on Pechini's method [17]. The molar ratio of metal cations, complexing agent (citric acid) and ethylene glycol was chosen to be 1:4:4 in the solution. A small amount of the solution was dried and then heated to 600°C in air. Ar was then introduced to flush out the air and lastly an 80%  $\text{H}_2$  – 20%  $\text{CH}_4$  atmosphere was introduced. The final treatment was 880°C for 12 hr [18]. The synthesized powder was examined by X-ray diffraction (XRD) (Rigaku rotating anode) and the presence of WC as the only phase was confirmed. The porous structure was repeatedly impregnated by

incipient wetness until 20 vol.% carbide was embedded into the YSZ network.

The electrochemical behavior of the cells was studied by ac impedance spectroscopy (Solartron frequency response analyzer 1255 in combination with a Solartron electrochemical interface 1287) on symmetrical cells with a four electrode configuration. It is noteworthy that a laboratory-made gold paste was used as a current collector (atomised gold powder, Technic Inc., Cranston, Rhode Island). Impedance measurements were carried out under open circuit condition over a frequency range from 0.1 Hz to 100 kHz with a 10 mV ac perturbation. Also, to see the effect of polarization, galvanostatic test was done under 1, 5 and 10 mA. The microstructure of the electrodes both before and after electrochemical testing was examined on fractured surfaces with a JEOL 6301F field emission scanning electron microscope (FE-SEM). Bulk phase study was done by XRD and surface analysis was performed by X-ray photoelectron spectroscopy (XPS) (Axis 165 X-ray Photoelectron Spectrometer, Kratos Analytical).

### **3.3. Results and Discussion**

#### **3.3.1. Sintering**

The first challenge was how to sinter the conventional WC-YSZ cells. Sintering of WC-oxide composites has been reported under vacuum [19] and argon [20]. Moskała and Pyda [21], however, showed that sintering a WC-ZrO<sub>2</sub> composite in argon resulted in decomposition of the carbide phase due to reaction with the zirconia matrix. In the present work, when WC-YSZ cells were sintered under argon, XRD analysis after sintering did reveal that part of the carbide had

decomposed to tungsten metal. Sintering in 95% Ar – 5% H<sub>2</sub> was also unsuccessful as WC completely decomposed to tungsten. Eventually, a CO-CO<sub>2</sub> atmosphere was chosen to sinter the composites. Thermodynamically, a possible reaction between the carbide phase and the CO-CO<sub>2</sub> atmosphere is as follows:



At 1350°C, the equilibrium partial pressure of carbon monoxide is 0.997, which means that the CO content of the mixed atmosphere must be  $\geq 99.7\%$  to keep the carbide phase stable. Thus 1000 ppm CO<sub>2</sub>, balance CO was used and subsequent phase analysis confirmed that WC-YSZ was successfully sintered.

### 3.3.2. WC-YSZ composite electrodes

Figure 3.1(a) shows the ac impedance spectra of WC-YSZ at 800°C in humidified hydrogen (3% H<sub>2</sub>O) for two cells sintered at 1300 and 1400°C initially and after 20 hr. The first direct implication of the impedance spectra is that 1300°C is an adequate sintering temperature for the WC-YSZ composites. While the ohmic resistance of the cells sintered at 1300 and 1400°C is nearly the same, the polarization resistance of the cell sintered at 1400°C is more than twice as high as the one sintered at 1300°C. Secondly, comparing the impedances after 20 hr reveals that the activity in hydrogen is not stable. Figure 3.1(b) shows the XRD pattern of WZ-1300 after a 100 hr test in humidified hydrogen. As the phase analysis reveals, most of the carbide phase was decomposed to tungsten metal which explains the instability of the carbide under humidified hydrogen at 800°C.

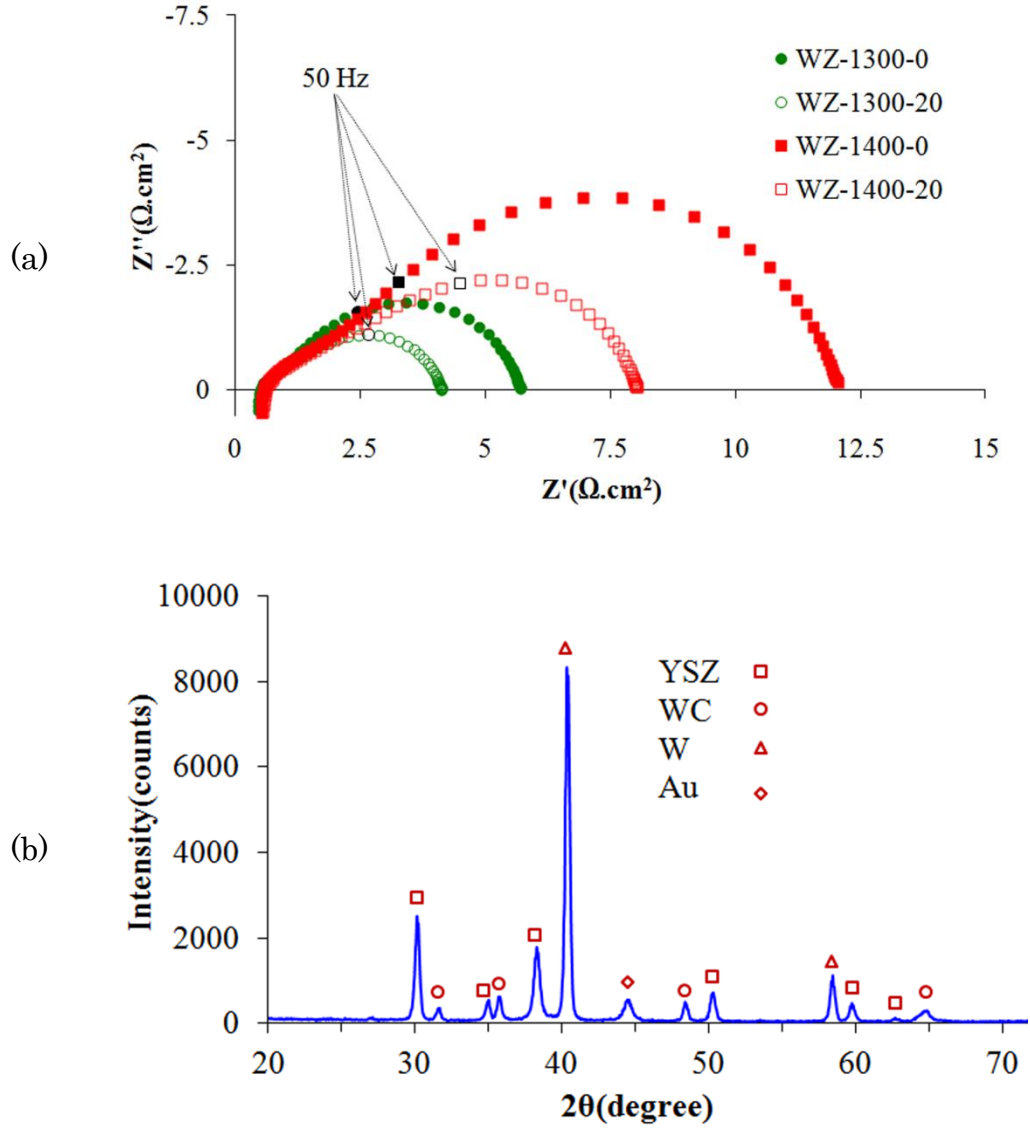


**Fig. 3.1.** (a) Ac impedance spectra of WC-YSZ at 800°C in humidified hydrogen for two cells sintered at 1300 and 1400°C, (b) XRD pattern of WZ-1300 after a 100 hour test in humidified hydrogen.

Thermodynamically, three possible reactions in humidified hydrogen are as follows:





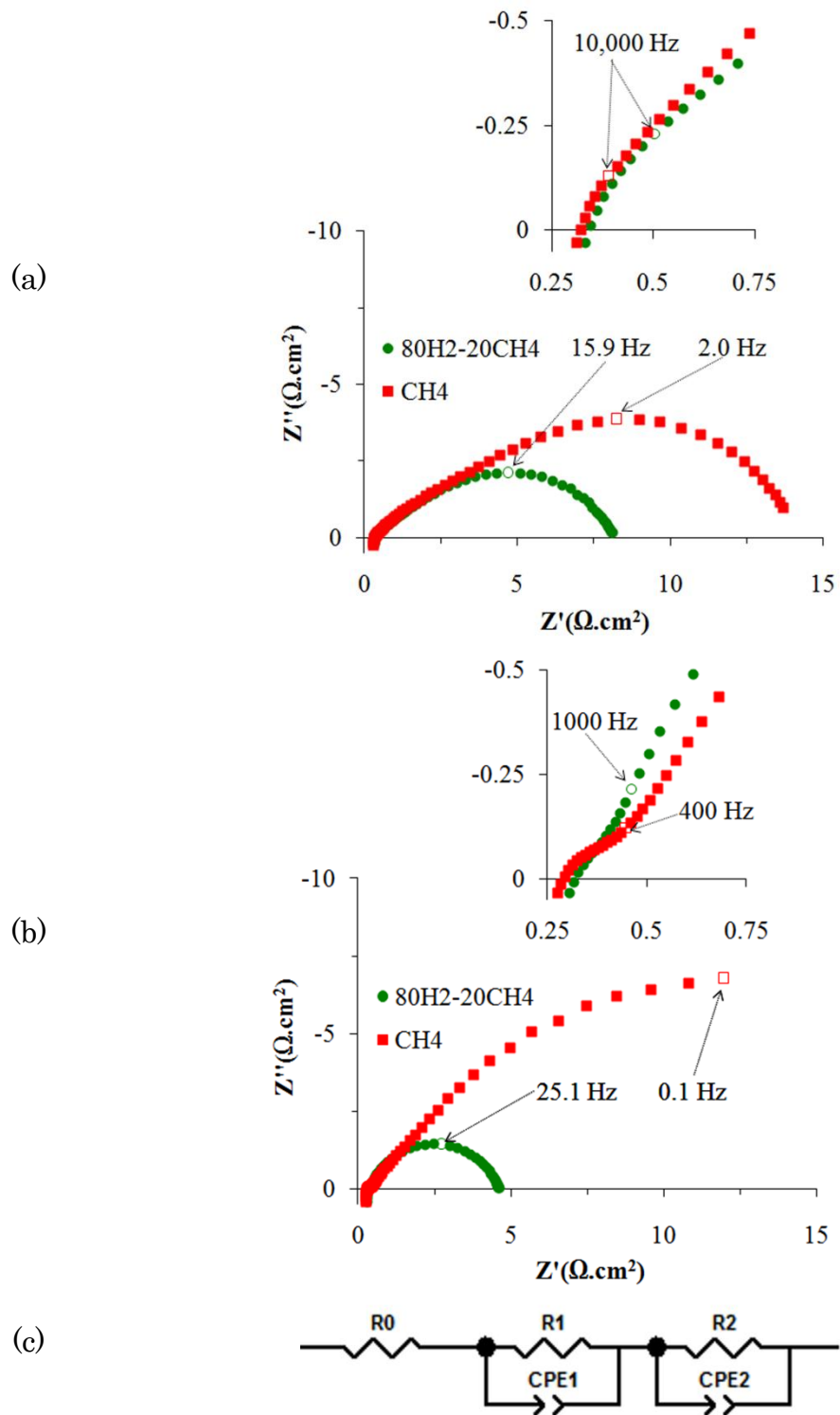
The standard Gibbs free energy for these reactions at 800°C are +66,170, +17,725, and -45,876 J, respectively. According to the 2<sup>nd</sup> and 3<sup>rd</sup> reactions, the equilibrium partial pressures of methane and carbon monoxide are 0.0006 and 0.0042 atm (H<sub>2</sub> and H<sub>2</sub>O were 0.97 and 0.03 atm, respectively), respectively. Additionally, based on the 4<sup>th</sup> reaction (methane reforming), 0.025 atm CH<sub>4</sub> is needed to form the required amount of CO (0.0042 atm) in humidified hydrogen (3% H<sub>2</sub>O – 97% H<sub>2</sub>) at 800°C. This means that if a slight amount of methane (>2.5%) is introduced into the humidified hydrogen atmosphere, the carbide phase will remain unchanged under open circuit voltage condition. Therefore, to assure the stability of the carbide phase, the study was performed under either a humidified 80% H<sub>2</sub> – 20% CH<sub>4</sub> mixed atmosphere or humidified methane.

Figure 3.2(a) compares the activity of a conventional WC-YSZ composite cell under humidified 80% H<sub>2</sub> – 20% CH<sub>4</sub> and humidified CH<sub>4</sub>. In order to accurately analyze the impedance spectra, a similar test was performed with WC-infiltrated porous YSZ electrodes and the electrochemical activity of such a cell is illustrated in Figure 3.2(b). No matter whether the cell is conventional or infiltrated, the impedance comprises two semicircles: a small arc in the high-medium frequency range and a relatively large arc in the low frequency range. This is the case for both the mixed and methane atmospheres. To attribute the semicircles, an equivalent circuit is shown in this figure (3.2(c)) which includes the ohmic resistance corresponding to the YSZ electrolyte (R<sub>0</sub>), and the non-ohmic polarization corresponding to the composite electrode (R<sub>1</sub> and R<sub>2</sub>). Table 3.1 summarizes the resistances for the conventional cell and the infiltrated one. Although the volume ratio of WC:YSZ is 50:50 in the conventional cell and 20:80 in the infiltrated

one, their ohmic resistance remains the same. Since the thickness of the electrode layer is 25-30  $\mu\text{m}$  in these cells, they are essentially thick enough to reveal the potential percolation problem in the infiltrated cell. Similar low ohmic resistance of these cells, however, indicates that the carbide phase remains well connected in the infiltrated cell. This argument is well supported by comparison between the SEM micrographs of these two cells in Figure 3.3.

As for the non-ohmic polarization, the small arc in the high-medium frequency range can be attributed to charge transfer resistance ( $R_1$ ) corresponding to electron transfer and ion transfer processes occurring at the interfaces [22,23]. As discussed elsewhere [16], when a porous YSZ support and a dense electrolyte layer are co-sintered at high temperatures, a much lower interface resistance can be obtained. That is why the infiltrated cell showed a much smaller charge transfer resistance. Furthermore, as expected, the interfacial resistance remains about the same under various fuels which is the case for both cells.

The large arc in the low frequency range of the impedance spectra is predominantly attributed to non-charge transfer processes including surface reactions and solid state and gas phase diffusion [22-24]. As indicated by Table 3.1, the non-charge transfer resistance ( $R_2$ ) not only is affected by the type of cell (conventional or infiltrated), but it also remarkably varies from hydrogen-rich fuel to methane fuel. Since a gas diffusion limitation is not expected under OCV conditions, it is suggested that the low frequency arc is due to surface reactions. Therefore, the considerable difference between  $R_2$  under hydrogen-rich and methane fuels for both cell types is simply because methane is much harder to activate at 800°C [25].



**Fig. 3.2.** (a) and (b) Ac impedance of a conventional WC-YSZ composite cell and a WC-infiltrated porous YSZ cell under humidified 80% H<sub>2</sub> – 20% CH<sub>4</sub> and humidified CH<sub>4</sub>, (c) an equivalent circuit model.

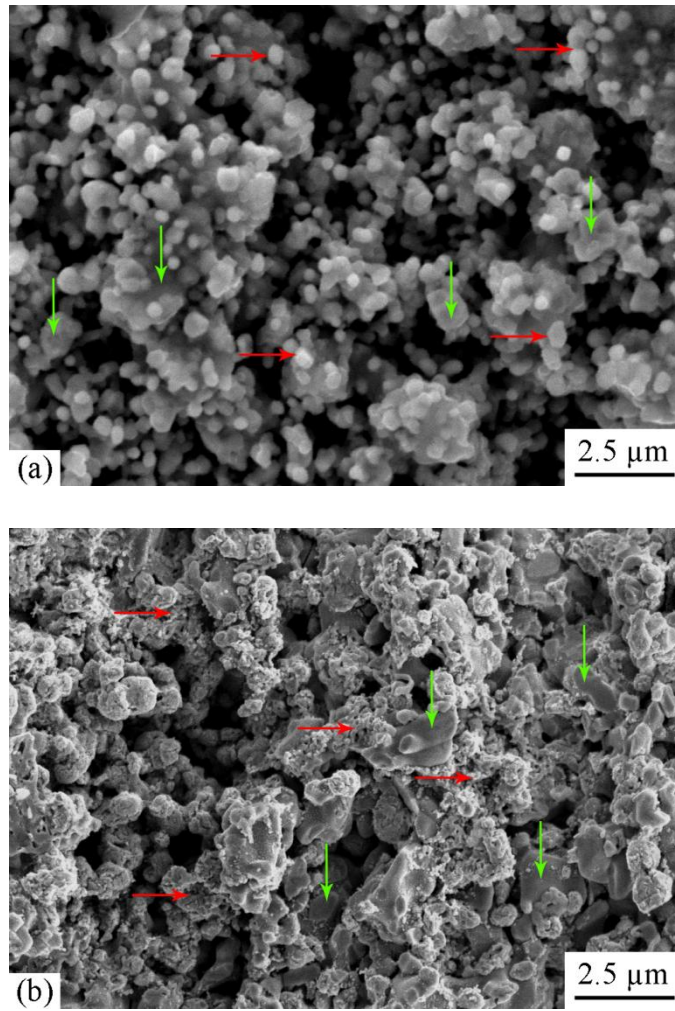


**Fig. 3.3.** SEM micrographs of (a) a conventional WC-YSZ composite cell and (b) a WC-infiltrated porous YSZ cell. Vertical arrows point to YSZ and horizontal ones point to WC.

**Table 3.1.** Ohmic and non-ohmic polarization of conventional and infiltrated carbide symmetrical cells.

Name	R0 ( $\Omega\cdot\text{cm}^2$ )		R1 ( $\Omega\cdot\text{cm}^2$ )		R2 ( $\Omega\cdot\text{cm}^2$ )	
	80-20 mix	CH <sub>4</sub>	80-20 mix	CH <sub>4</sub>	80-20 mix	CH <sub>4</sub>
Conventional WZ	0.33	0.31	1.2	1.3	6.5	12.9
Infiltrated WZ	0.33	0.28	0.1	0.1	4.2	25.5

Figure 3.4 illustrates the impedance spectra of a conventional WC-YSZ composite in a humidified 80% H<sub>2</sub> – 20% CH<sub>4</sub> mixed atmosphere at three different temperatures. The configuration of the impedance spectra remains the same at these temperatures: a small semicircle in the high-medium frequency range and a relatively large one in the low frequency range. A similar equivalent circuit model (Figure 3.2(c)) was used to calculate the ohmic and non-ohmic polarization at different temperatures. The area specific resistances of this cell as function of temperature are illustrated in Figure 3.5. The non-ohmic polarization (R1 + R2) is much larger than the ohmic resistance. Also, the charge transfer polarization (R1) is considerably smaller than the non-charge transfer polarization (R2).

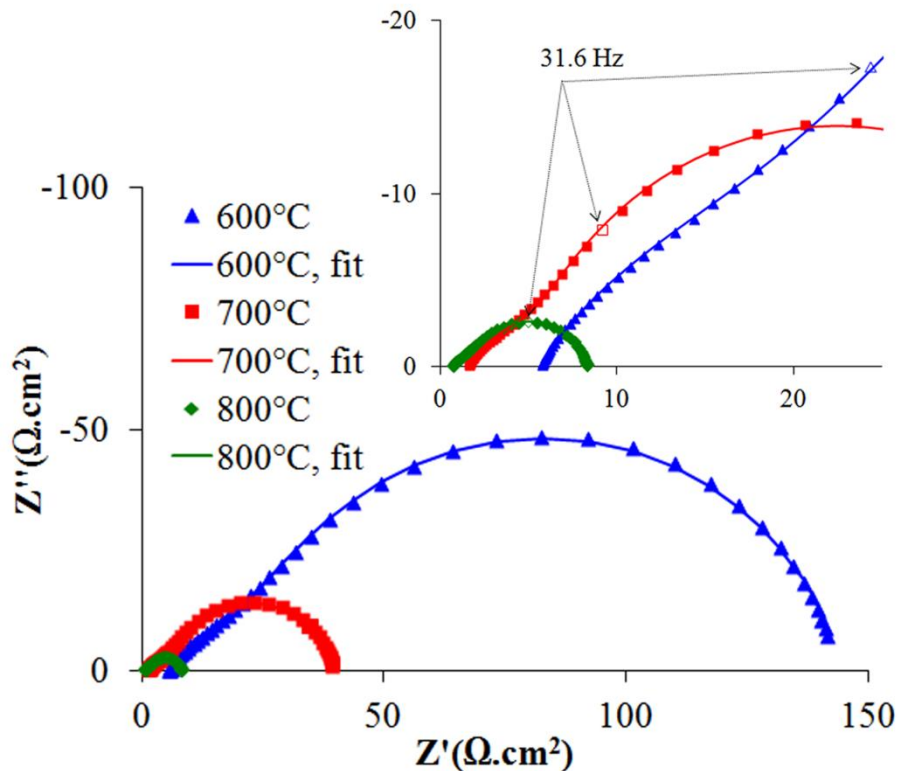


**Fig. 3.4.** Effect of temperature on the ac impedance of a conventional WC-YSZ composite cell.

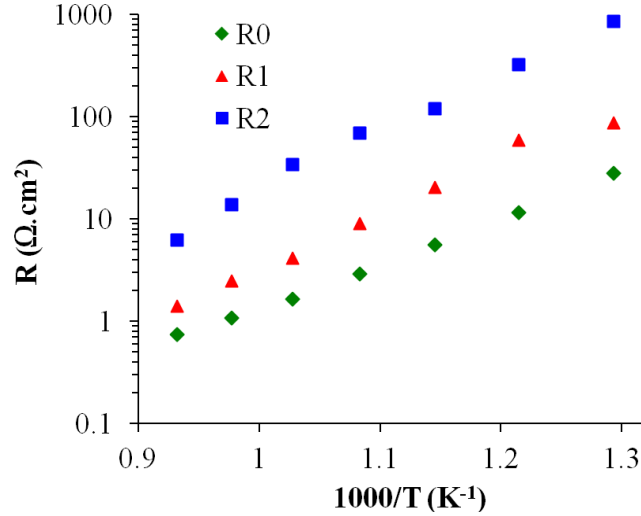


**Fig. 3.5.** Area specific resistances of a conventional WC-YSZ composite cell as a function of temperature.

### 3.3.3. Electrocatalyst incorporation

As already discussed, although the ohmic resistance of a tungsten carbide-based electrode is reasonably low, the contribution of non-ohmic polarization to the electrochemical performance is rather large and needs to be improved by incorporation of active electrocatalysts into the carbide-based electrode. Figure 3.6 shows the impedance spectra of different carbide-based symmetrical cells under (a) humidified 80% H<sub>2</sub> – 20% CH<sub>4</sub> mixed atmosphere, and (b) humidified methane at 800°C. WZ, CWZ, RWZ and RCWZ are conventional WC-YSZ composite, 10 wt% ceria infiltrated WZ, 3 wt% Ru infiltrated WZ, and 10 wt% ceria and 3 wt% Ru infiltrated WZ, respectively. As expected, the incorporation of an active electrocatalyst into the carbide-based electrode noticeably improves the electrochemical performance of the electrode both under the mixed atmosphere and methane. For the sake of comparison, the ohmic (R0) and non-ohmic (R1 and R2) polarization are summarized in Table 3.2. The polarization is

calculated based on the equivalent circuit model shown in Figure 3.2(c) and the corresponding fit data.

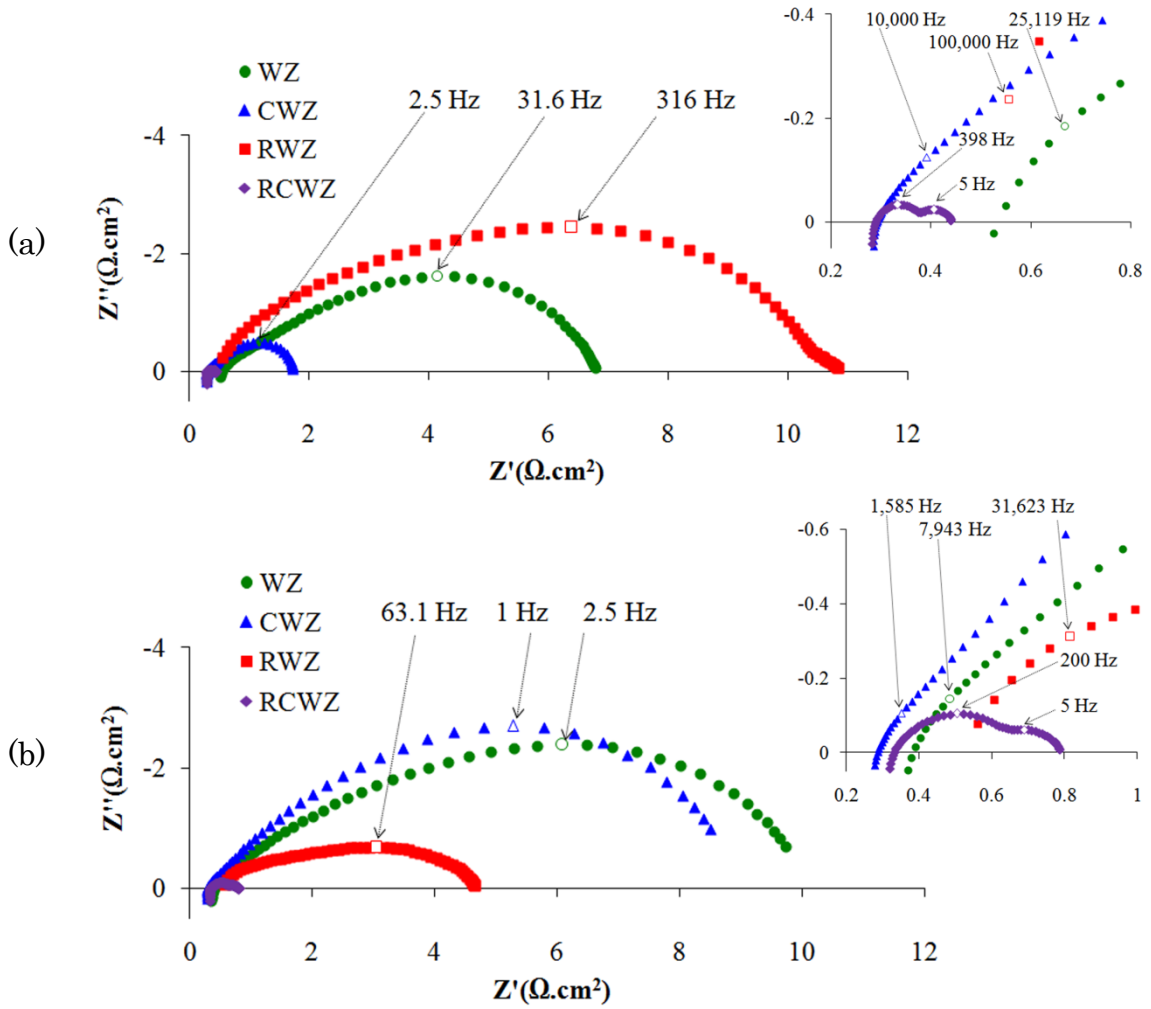


**Fig. 3.6.** Ac impedance spectra of different carbide-based symmetrical cells under (a) humidified 80% H<sub>2</sub> – 20% CH<sub>4</sub> mixed atmosphere, and (b) humidified methane at 800°C.

**Table 3.2.** Ohmic and non-ohmic polarization of different carbide-based symmetrical cells.

Name	R0 (Ω.cm <sup>2</sup> )		R1 (Ω.cm <sup>2</sup> )		R2 (Ω.cm <sup>2</sup> )	
	80-20 mix	CH <sub>4</sub>	80-20 mix	CH <sub>4</sub>	80-20 mix	CH <sub>4</sub>
WZ	0.6	0.4	1.8	1.1	9	8.8
CWZ	0.3	0.3	0.2	0.8	1.25	7.9
RWZ	0.4	0.5	1	1	9.4	3.2
RCWZ	0.35	0.35	0.1	0.35	0.25	0.1

Ceria is known as one of the active electrocatalysts in hydrocarbon fuels [4]. Thus incorporation of ceria into the carbide-based electrode was a reasonable approach to follow. When using the humidified 80% H<sub>2</sub> – 20% CH<sub>4</sub> mixed fuel, the addition of ceria to the carbide-based electrode reduced both the charge transfer and non-charge transfer polarization to a great extent. Such improvement, however, was much lower when humidified methane was used as the fuel, which is related to CH<sub>4</sub> being more difficult to activate [5].

Precious metals such as Pd, Ru and Rh are renowned as excellent heterogeneous catalysts for hydrocarbon fuels with Ru being the least expensive of the three metals [26-28]. For example, a study of propane conversion over Ru as a promoter of anodic processes in SOFCs showed that no carbon deposits formed during operation of the anode in direct oxidation and internal reforming processes [29]. Herein, the effect of Ru infiltration into the carbide-based electrode was accordingly studied. Surprisingly, when the electrode was impregnated with Ru, the electrochemical activity of the cell degraded in the mixed atmosphere. To ensure the accuracy of the result, this test was repeated twice and the exact same behavior was observed. Although the addition of Ru did not affect the charge-transfer polarization, the non-charge transfer overpotential markedly increased compared to the ceria infiltrated cell in the 80-20 mixture. This, however, was not the case under humidified methane fuel. The electrochemical activity of Ru infiltrated carbide-based electrode showed a great improvement compared to the cells with no Ru (Figure 3.6(b)).

Not only are ceria-based materials active catalysts for hydrocarbon fuels, they also are renowned as structural and electronic promoters of heterogeneous catalytic reactions [30]. Therefore, in another experiment, the carbide-based electrode was infiltrated first with 10

wt% ceria and then with 3 wt% Ru. He et al. [31] showed that a solution of  $(\text{NH}_4)_2\text{Ce}(\text{NO}_3)_6$  in ethanol resulted in the most uniform ceria film on a YSZ porous support. That is why the cerium ammonium nitrate solution in ethanol was used to cover the WC-YSZ support. As indicated by Figure 3.6 and Table 3.2, the performance of the ceria-Ru infiltrated cell dramatically improved in both mixed and methane atmospheres. The synergistic behavior of ceria-Ru coexistence is usually attributed to strong metal-support interactions (SMSIs) which are typically observed for ceria loaded with Pt group metals [32]. Figure 3.7 shows an SEM micrograph of the ceria-Ru infiltrated WC-YSZ electrode. Ceria forms a uniform nano-particle (10-30 nm) network over the carbide-based electrode. This uniform ceria coating acts as a structural and electronic promoter of Ru which results in a great improvement in the electrochemical performance in both mixed and methane fuels.

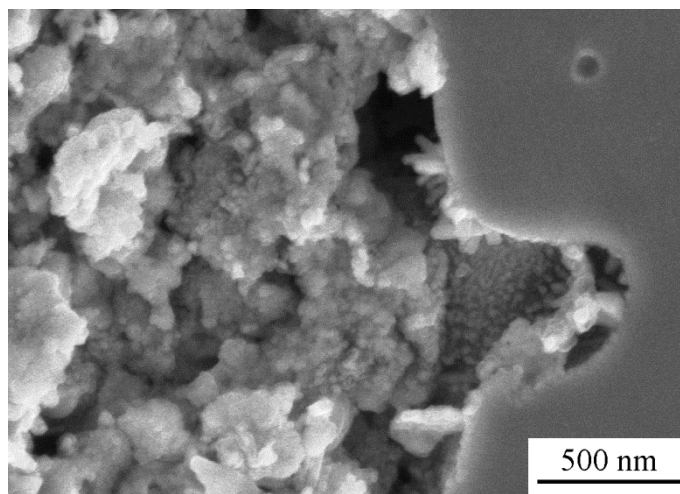


**Fig. 3.7.** SEM micrograph of RCWZ cell (electrode/electrolyte interface). As an example, the dip in YSZ electrolyte is well covered with very small ceria particles.

### 3.3.4. Electrode performance stability

Since this study is based on symmetrical cell analysis, the drawback of this technique should be considered. When an electrode material behaves in a hysteretic manner, the correlation between symmetrical cell study and normal fuel cell analysis is rather poor [33]. Therefore, it is important to investigate if the carbide-based electrodes are sensitive to polarization. A  $10 \text{ mA cm}^{-2}$  current was applied to the carbide-based cells mentioned in Table 3.2 for a period of 12 hr under methane fuel at  $800^\circ\text{C}$ . It is noteworthy that when a current is applied to a symmetrical cell, one electrode is polarized anodically and the other cathodically. Figure 3.8 illustrates the stability of the potential under the applied current for these cells. Interestingly, the cells with no Ru behaved quite erratically under current whereas the performance of Ru infiltrated cells remained unchanged.

Figure 3.9 shows the impedance spectra of (a) WZ and (b) RCWZ before and after the current was applied with methane fuel. Both ohmic and non-ohmic resistances were affected by polarization of the WC-YSZ

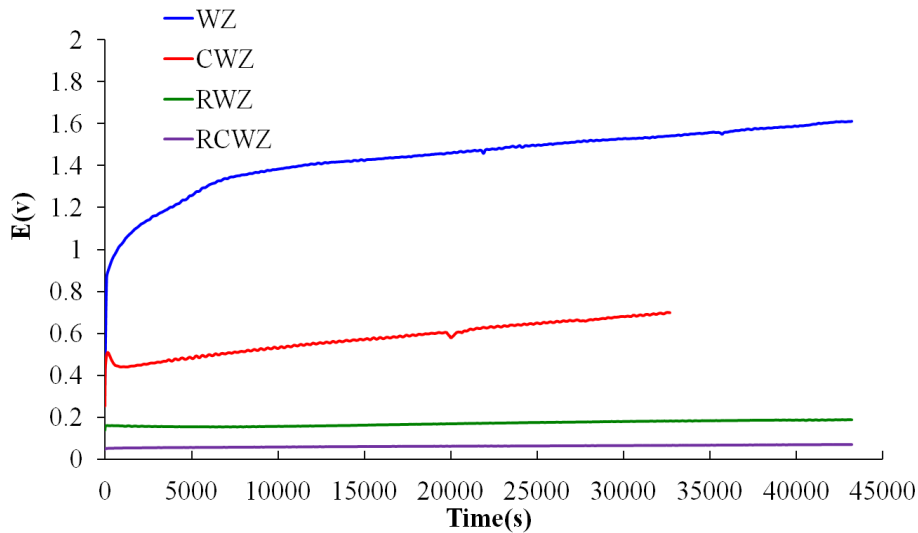


**Fig. 3.8.** The stability of WZ, CWZ, RWZ and RCWZ (respectively from top to bottom) under an applied current.

electrodes: a rather small increase in ohmic resistance and a very large increase in non-ohmic resistance. Ceria-Ru infiltrated WC-YSZ electrodes, however, remained unaffected by the polarization. A subtle decrease in the ohmic resistance and a small increase in non-ohmic resistance are both due to slight carbon formation during the 12 hr test under methane. Ceria infiltrated WC-YSZ (CWZ) behaved similarly to the conventional WC-YSZ and Ru infiltrated WC-YSZ (RWZ) resembled the ceria-Ru infiltrated one (the results for CWZ and RWZ are not shown here).

To shed light on this, bulk phase analysis (XRD) and surface chemical analysis (XPS) were done after each test. Figure 3.10(a) shows the XRD pattern of the ceria-Ru infiltrated WC-YSZ (RCWZ) cell. Although tungsten carbide remained the major tungsten-based phase, tungsten metal and tungsten oxide phases were present as minor phases. XPS analysis, however, revealed that the small changes in the carbide phase only occur on the surface. The XPS spectra of tungsten (W4f) are illustrated in Figure 3.10(b) before and after ion etching. The in-situ etching was done using a 4 keV Ar ion beam, scanned over an area of 1-2 mm<sup>2</sup> for a period of 1800 s. The sputter rate was about 2-3 nm/min. Before etching, four peaks were detected: the first two at lower binding energies are characteristic of the W-C chemical state (carbide) and the other two at higher binding energies are characteristic of the W-O chemical state (oxide). On the other hand, once the exposed surface was etched, no oxide state was detected. This simply means that oxidation of the carbide phase is superficial. Such behavior was almost always the case for all of the carbide-based electrodes. It should be mentioned that since the binding energy for tungsten carbide and tungsten metal are rather close, W-C and W-W peaks cannot be discriminated.

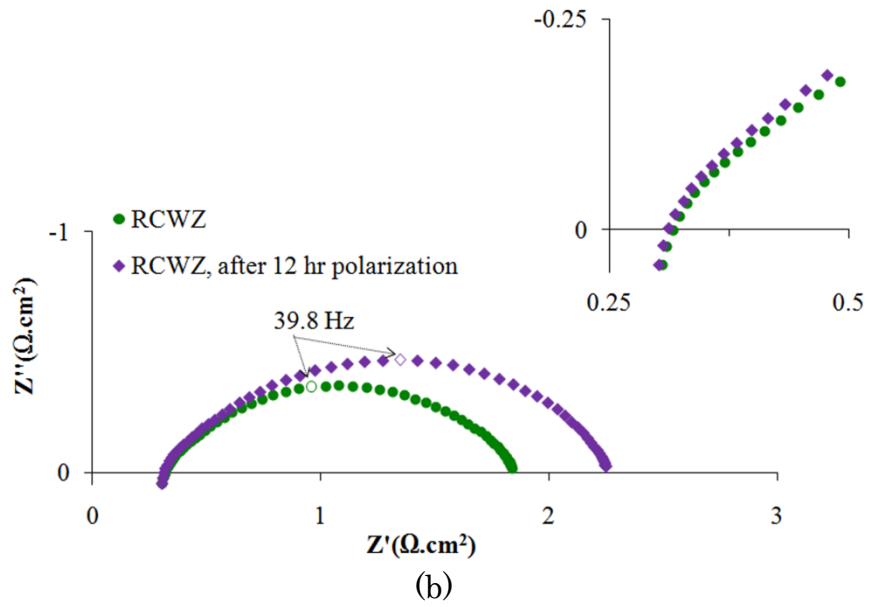
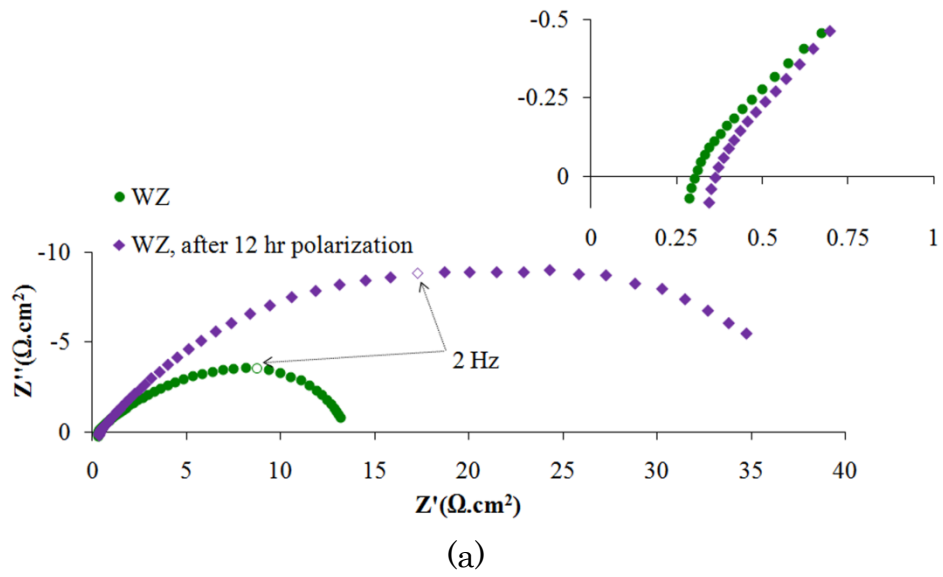
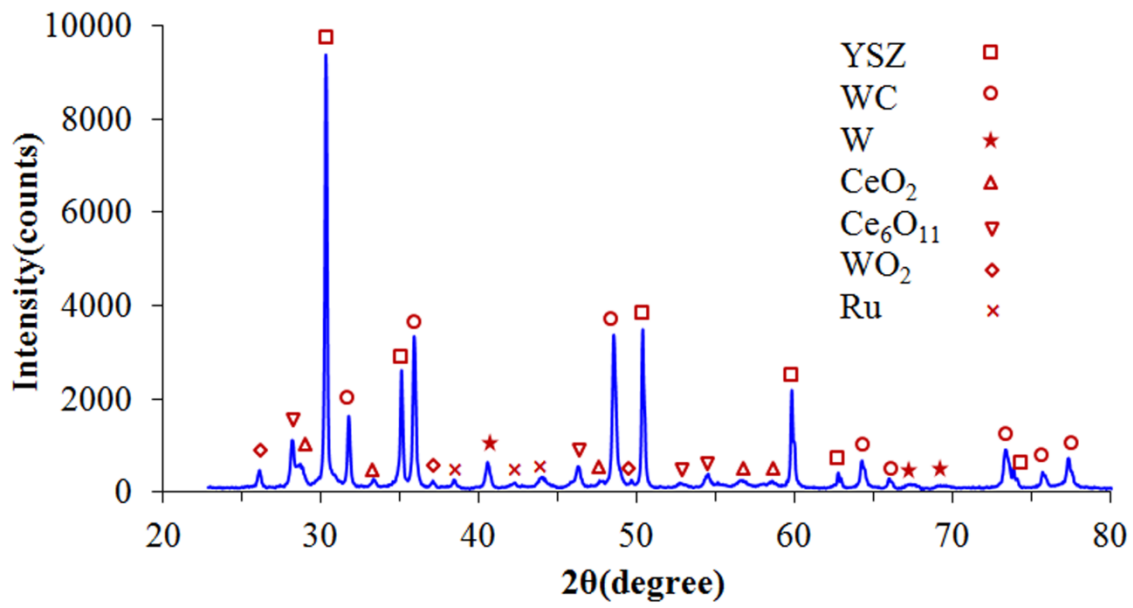
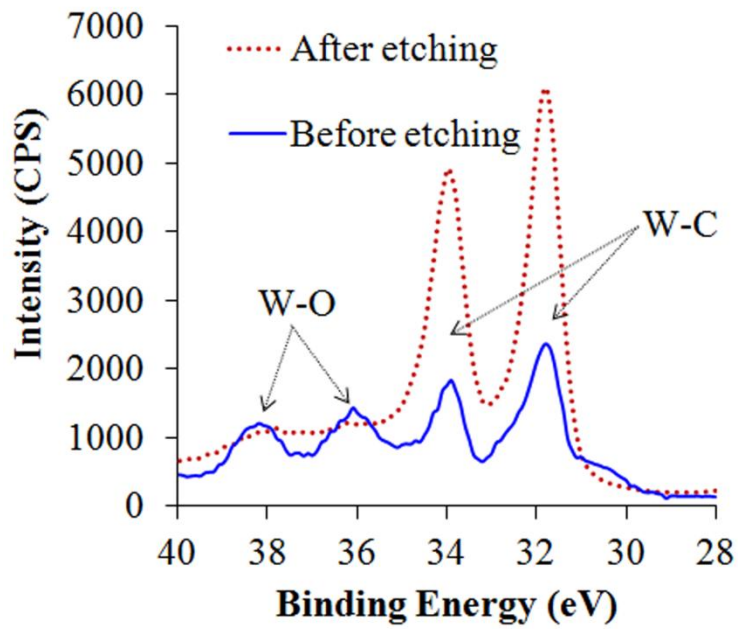


**Fig. 3.9.** Ac impedance spectra of (a) WZ and (b) RCWZ before and after current was applied.



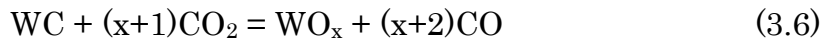
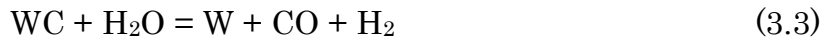
(a)



(b)

**Fig. 3.10.** (a) XRD pattern of RWCZ cell after performing the test, (b) XPS spectra of tungsten (W4f) before and after ion etching.

Since the stability of the carbide phase is one of the major concerns about the potential application of tungsten carbide-base electrodes in solid oxide fuel cells under hydrocarbon fuels, it is helpful to determine the stability of WC when exposed to various reforming gases, including H<sub>2</sub> and CO as reducing and carburizing gases and H<sub>2</sub>O and CO<sub>2</sub> as oxidizing gases. The possible reactions could be as follows:



Since H<sub>2</sub>O and CO<sub>2</sub> are the two oxidizing gases, an oxidizing ratio was defined as  $R = (\text{H}_2\text{O} + \text{CO}_2)/(\text{H}_2 + \text{CO})$ . Four different mixed atmospheres with various oxidizing ratios were utilized. Table 3.3 summarizes the composition of these atmospheres and the corresponding oxidizing ratio. 5 g of the carbide powder was treated for 12 hr at 800°C under each atmosphere and phase analysis was done after each treatment. The XRD spectra for the treated powders are shown in Figure 3.11. As indicated in the Figure, the carbide remained the major phase; nonetheless, a slight amount of oxide phase was present in all the treated powders. The oxide state was WO<sub>2</sub> when the oxidizing ratio was 0.88 and 1.2, and the amount of the oxide phase was about 1 wt%. On the other hand, when the oxidizing ratio was 1.67 and 2.63, the oxide state was WO<sub>3-x</sub> (x = 0-0.3) and the amount of the

oxide phase was about 3-4 wt%. It is obvious that the oxide is quite superficial because the amount of oxide is small even when the carbide is exposed to oxidizing gases.

Additionally, in another experiment, two carbide-based discs were treated in the 3<sup>rd</sup> atmosphere with R=1.67 for 36 hr at 800°C. The first disc was a conventional WC-YSZ composite whereas the second one was a 3 wt% Ru infiltrated WC-YSZ disc. Again, as expected, a slight oxide phase was present in the conventional cell; nonetheless, no oxide phase was detected in the infiltrated sample, which indicates the further significance of having Ru on the carbide-based electrodes.

**Table 3.3.** Oxidation of WC in different gas mixtures.

Atmosphere	H <sub>2</sub> (%)	CO (%)	H <sub>2</sub> O (%)	CO <sub>2</sub> (%)	Ar (%)	R	Composition
1	2.85	2.85	3	2	89.3	0.88	1 wt% WO <sub>2</sub>
2	1.75	1.75	3	1.2	92.3	1.2	1 wt% WO <sub>2</sub>
3	1.14	1.14	3	0.8	93.92	1.67	3-4 wt% WO <sub>3-x</sub>
4	0.57	0.57	3	0.4	95.46	2.63	3-4 wt% WO <sub>3-x</sub>

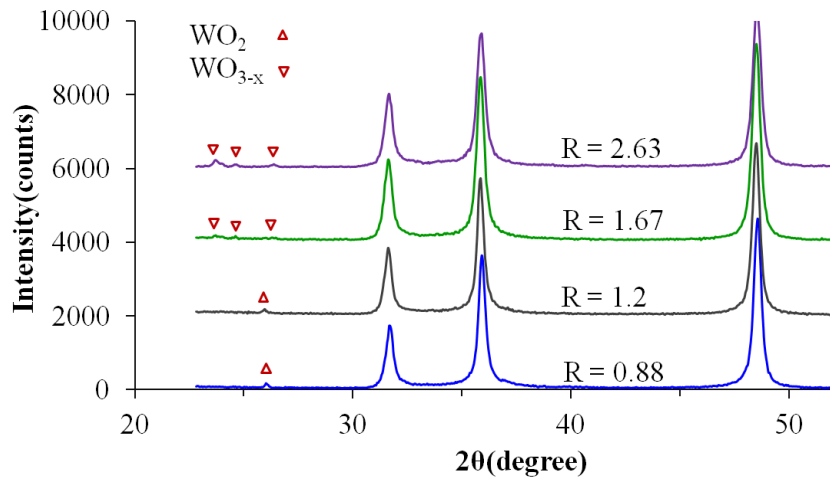


**Fig. 3.11.** XRD spectra for WC powders treated under atmospheres with oxidizing ratios of 0.88, 1.2, 1.67 and 2.63.

### 3.3.5. Electrode reaction mechanisms

Ever since the similarity between Pt and tungsten carbide in surface catalysis was shown [9], many attempts have been made to investigate the catalytic characteristics of Groups IV-VI carbides, especially for conversion of methane to synthesis gas. Fortunately, deactivation of the carbide catalyst due to oxidation reactions and the mechanisms of methane conversion over the carbide catalyst are well studied for the CH<sub>4</sub> conversion application [34-37]. Claridge et al. [34] showed that tungsten carbide sluggishly deactivated during both dry and steam reforming due to oxidation of the carbide phase. On the other hand, the carbide catalyst remained absolutely stable at elevated pressures. They explained that such deactivation at atmospheric pressures is predominantly governed by kinetics. The oxidation reactions (equations 3.5 and 3.6) have higher rates than the recarburization reaction (equation 3.9) which causes the instability of the carbide.

Similar to the proposed mechanisms for reforming reactions over metal carbides [34], two potential mechanisms could be proposed for electrochemical oxidation of methane over tungsten carbide in a fuel cell: a redox mechanism and a noble metal mechanism. In the redox mechanism, once the charge transfer reaction of the oxygen ion takes place, the corresponding oxygen atom (O\*) adsorbs on the carbide surface and reacts with the carbon in the carbide surface. Such a reaction creates a carbon vacancy (W<sub>-</sub>) to be filled with either carbon or oxygen:





Reactions 3.12 and 3.13 result in recarburization while reaction 3.14 oxidizes the carbide phase. On the other hand, the noble metal mechanism happens when the adsorbed carbon ( $C^{*}$ ) from methane dissociation (equation 3.13) readily reacts with adsorbed oxygen ( $O^{*}$ ):



When the noble metal mechanism is considered, the surface carbon atoms from the carbide phase are not involved in the mechanism and the carbide phase remains stable.

As discussed earlier, although tungsten carbide always remained as the major phase, a slight amount of tungsten oxide phase was detected in all of the cells. This confirms that the surface carbon atoms from the carbide participate in the electrochemical reactions. Although the amount of oxide phase is rather insignificant, it is crucial to ensure that the carbide phase remains stable and does not deactivate due to a progressive oxidation process. It was observed here that not only did the Ru infiltrated cells behave reasonably stably, they also did not perform hysteretically. Based on the above mentioned mechanisms, Ru can contribute to the stability of the carbide-based electrode in two possible ways. Since the deactivation of the carbide phase is due to a slower rate of recarburization as opposed to oxidation, one explanation is that Ru can actually catalyze the recarburization reaction. It can also promote the noble metal mechanism which does not involve surface carbon atoms from the carbide phase. Ru is known to catalyze scission of C-H bond and act as a reforming promoter [29].

### 3.3.6. Overall discussion

The ability to internally reform hydrocarbon fuels and to utilize the produced H<sub>2</sub> and CO, along with the possibility to directly utilize hydrocarbon fuels (direct oxidation), represents an exceptional advantage of SOFCs over other fuel cell systems. However, carbon deposition resulting from hydrocarbon pyrolysis is a serious problem associated with hydrocarbon fuel utilization particularly with Ni-based anodes [38, 39]. The mechanism of carbon formation on nickel includes carbon deposition on the nickel surface, carbon dissolution into the nickel bulk and carbon fiber precipitation which results in metal dusting [6]. The buildup of carbon leads to blocking of active sites on the anode and results in a loss of cell performance. Further carbon deposition eventually impedes the gas flow in the anode channels which can cause a serious loss of cell performance and even failure.

Cu-based anodes have been extensively investigated [4,25] as promising anode materials under hydrocarbon fuels mainly because copper, as opposed to nickel, does not promote the formation of carbon. Nonetheless, there are several limitations concerning Cu-based anodes [5]. Firstly, the catalytic activity of copper towards hydrocarbon fuels is rather poor. Therefore, incorporation of an active heterogeneous catalyst into the copper-based electrode is necessary. Additionally, because Cu has a relatively low melting point (1085 °C), these anodes are not stable at high temperatures. Also, since the melting temperatures of copper oxides are rather low, the conventional fabrication technique which is used for Ni-based anodes based on the metal oxide cannot be utilized with Cu-based electrodes. Finally, due to the formation of catalytically inactive alloys, Cu-based anodes are not compatible with precious metals such as Pd and Ru, which are excellent catalysts for hydrocarbon oxidation [4].

From this work, similar to Cu-based anodes, WC-based anodes do not catalyze the formation of carbon and have a comparable electronic conductivity. Considering the limitations of Cu-based anodes, however, the carbide-based anodes could be quite advantageous. The very high melting point of tungsten carbide (2870°C) guarantees the high temperature stability of these electrodes for long lasting applications. Furthermore, precious metals can be easily used to enhance the performance of the carbide-based anodes under hydrocarbon fuels. On the other hand, the stability of the carbide phase could be a real concern particularly under high fuel utilization conditions. Here, it has been shown that oxidation of the carbide phase is essentially a part of the fuel oxidation process. As long as the rate of carbide oxidation and that of oxide recarburization remain about the same, cell performance will be stable. Moreover, since these oxidation/ recarburization reactions take place on the surface, the electronic conductivity of the carbide phase is not affected.

To the best of the authors' knowledge, the behavior of these carbide-based materials under hydrocarbon fuel is rather unknown. This study shows that WC-based electrodes could potentially be considered as anode materials for direct utilization of hydrocarbon fuels. Undoubtedly, one single study cannot reveal all the benefits and address all the challenges of a potential electrode material. Further investigations are required to fully exploit the potential of tungsten carbide for SOFC applications.

### 3.4. Conclusions

The following conclusions could be drawn from the current study:

- I. WC-based electrodes are not stable in hydrogen fuels. The carbide phase sluggishly reacts with  $H_2$  and decomposes to tungsten metal.
- II. The ohmic polarization of a conventional WC-YSZ cell was very low. The charge-transfer polarization was reasonably low as well. However, reaction polarization was relatively high and needed to be improved by incorporation of active catalysts.
- III. Incorporation of 10 wt% ceria and 3 wt% ruthenium into the WC-YSZ electrode remarkably improved both charge transfer and reaction polarization. This infiltrated cell performed stably under polarization and did not show hysteretic behavior.
- IV. Oxidation of the carbide phase is actually one of the possible mechanisms of the fuel oxidation process. As long as the rate of carbide oxidation and that of oxide recarburization remain about the same, the cell performance is stable.

## References

- [1] A. Atkinson, S. Barnett, R. J. Gorte, J. T. S. Irvine, A. J. McEvoy, M. Mogensen, S. C. Singhal, J. M. Vohs, *Nat. Mater.* 3 (2004) 17.
- [2] J. B. Goodenough, Y. H. Huang, *J. Power Sources* 173 (2007) 1.
- [3] C. Sun, U. Stimming, *J. Power Sources* 171 (2007) 247.
- [4] S. McIntosh, R. J. Gorte, *Chem. Rev.* 104 (2004) 4845.
- [5] M. D. Gross, J. M. Vohs, R. J. Gorte, *J. Mater. Chem.* 17 (2007) 3071.
- [6] M. L. Toebes, J. H. Bitter, A. J. van Dillen, K. P. de Jong, *Catal. Today* 76 (2002) 33.
- [7] S.P. Jiang, S.H. Chan, *J. Mater. Sci.* 39 (2004) 4405.
- [8] D. Simwonis, F. Tietz, D. Stover, *Solid State Ionics* 132 (2000) 241.
- [9] R. B. Levy and M. Boudart, *Science* 181 (1973) 547.
- [10] H. H. Hwu, J. G. Chen, *Chem. Rev.* 105 (2005) 185.
- [11] Y. Hara, N. Minami, H. Itagaki, *Appl. Catal. A* 323 (2007) 86.
- [12] D. J. Ham, Y. K. Kim, S. H. Han, J. S. Lee, *Catal. Today* 132 (2008) 117.
- [13] R. Ganesan, D. J. Ham, J. S. Lee, *Electrochem. Comm.* 9 (2007) 2576.
- [14] A. Naoumidis, F. Tietz, G. Stochniol, A. Gupta, T. Hauber, *Proceeding of the 2nd European Solid Oxide Fuel Cell Forum, oberrohrdorf, Switzerland* (1996) 727.
- [15] Z. Cheng, S. Zha, M. Liu, *J. Electrochem. Soc.* 153 (2006) A1302.
- [16] A. Torabi, A. R. Hanifi, T. H. Etsell, P. Sarkar, *J. Electrochem. Soc.* 159 (2011) B1.
- [17] M. P. Pechini, U.S. Patent No. 3,330,697 (1967).
- [18] A. J. Brungs, A. P. E. York, M. L. H. Green, *Catal. Lett.* 57 (1999) 65.
- [19] T. Venkateswaran, D. Sarkar, B. Basu, *Wear* 260 (2006) 1.

- [20] W. Acchar, A.E. Martinelli, F.A. Vieira, C.A.A. Cairo, *Mater. Sci. Eng. A* 284 (2000) 84.
- [21] N. Moskała, W. Pyda, *J. Europ. Ceram. Soc.* 26 (2006) 3845.
- [22] S. B. Adler, *Solid State Ionics* 111 (1998) 125.
- [23] T. L. Reitz, H. Xiao, *J. Power Sources* 161 (2006) 437.
- [24] Q. A. Huang, R. Hui, B. Wang, J. Zhang, *Electrochim. Acta* 52 (2007) 8144.
- [25] S. Park, R. Craciun, J.M. Vohs, R.J. Gorte, *J. Electrochem. Soc.* 146 (1999) 3603.
- [26] R. J. Gorte, J. M. Vohs, *J. Catal.* 216 (2003) 477.
- [27] T. Hibino, A. Hashimoto, M. Yano, M. Suzuki, M. Sano, *Electrochim. Acta* 48 (2003) 2531.
- [28] Y. Takagi, B. Lai, K. Kerman, S. Ramanathan, *Energy Environ. Sci.* 4 (2011) 3473.
- [29] M. L. Faro, D. La Rosa, G. Monforte, V. Antonucci, A.S. Arico, P. Antonucci, *J. Appl. Electrochem.* 37 (2007) 203.
- [30] A. Trovarelli, *Catal. Rev.* 38 (1996) 439.
- [31] H. He, J. M. Vohs, R. J. Gorte, *J. Electrochem. Soc.* 150 (2003) A1470.
- [32] M. Hatanaka, N. Takahashi, N. Takahashi, T. Tanabe, Y. Nagai, A. Suda, H. Shinjoh, *J. Catal.*, 266 (2009) 182.
- [33] Y. Huang, J. M. Vohs, R. J. Gorte, *J. Electrochem. Soc.* 152 (2005) A1347.
- [34] J. B. Claridge, A. P. E. York, A. J. Brungs, C. Marquez-Alvarez, J. Sloan, S. C. Tsang, M.L.H. Green, *J. Catal.* 180 (1998) 85.
- [35] A. R. S. Darujati, D. C. LaMont, W. J. Thomson, *Appl. Catal. A* 253 (2003) 397.
- [36] D. C. LaMont, A. J. Gilligan, A. R. S. Darujati, A. S. Chellappa, W. J. Thomson, *Appl. Catal. A* 255 (2003) 239.

- [37] J. Sehested, C. J. H. Jacobsen, S. Rokni, J. R. Rostrup-Nielsen, J. Catal. 201 (2001) 206.
- [38] C. M. Finnerty, N. J. Coe, R. H. Cunningham, R. M. Ormerod, Catal. Today 46 (1998) 137.
- [39] R. Kikuchi, N. Koashi, T. Matsui, K. Eguchi, T. Norby, J. Alloys Compd. 408-412 (2006) 622.

## Chapter 4

# Tungsten Carbide-based Anodes for Solid Oxide Fuel Cells: Preparation, Performance and Challenges

### 4.1. Introduction

Ni-YSZ composites have been the dominant anodes of choice for solid oxide fuel cell applications for more than four decades [1-3]. This is mostly because of unrivalled attributes of such anodes including excellent catalytic activity toward hydrogen fuel, high electronic and sufficient ionic conductivity, and reasonable stability under SOFC operating conditions [3-5]. In addition, low cost, relative ease of fabrication and adequate mechanical strength are other practical contributing features of these cermets which make them even more attractive.

On the other hand, there are several limitations in regard to Ni-YSZ anode materials [6]. Incompatibility with hydrocarbon fuels is one of the most significant drawbacks of conventional Ni-YSZ anodes [7].

Nickel is an excellent catalyst for pyrolysis of hydrocarbon fuels [8]. As a result of such reaction, carbon is deposited on the Ni surface, dissolves into the Ni bulk and finally precipitates from it as fibers. Although several attempts have been made to improve the compatibility of the Ni-YSZ cermets and hydrocarbon fuels [9], the intrinsic instability of these anodes and disastrous consequences of the formation of carbon filaments limit the practicality of those attempts [7]. Other significant disadvantages of Ni-YSZ anodes includes high sensitivity to fuel impurities such as  $\text{H}_2\text{S}$ ,  $\text{CH}_3\text{SH}$ ,  $\text{COS}$ ,  $\text{NH}_3$  and  $\text{Cl}_2$  [10], microstructural change due to Ni phase coarsening [11] and poor resistance against redox cycling [12].

Development of alternative anode materials is thus a practical approach to directly utilize hydrocarbon fuels. The alternatives include a variety of ceramic-metal composites and oxide ceramics [1,4-7]. Copper-based cermets have been extensively investigated as a potential candidate for direct hydrocarbon utilization [7,13]. The major advantage of Cu over Ni is that it does not promote the formation of carbon fibers. Kim et al. [14] showed that Cu-CeO<sub>2</sub>-YSZ stably performed in a wide variety of hydrocarbons. While copper mainly contributes to electronic conductivity, the major role of ceria is to catalyze the oxidation of hydrocarbon fuel [13]. Although they are compatible with hydrocarbons, there are several drawbacks concerning Cu-based anodes [15]. First, the catalytic activity of copper towards hydrocarbon fuels is rather poor. Therefore, incorporation of active electrocatalysts into the copper-based electrodes is unavoidable. Second, because Cu has a relatively low melting point (1085 °C), long term stability of these anodes at higher operating temperatures is a serious concern. Third, the conventional fabrication technique involving NiO which is used for Ni-based anodes cannot be used with

Cu-based electrodes because of the low melting temperatures of copper oxides. Finally, these cermetes are not compatible with precious metal catalysts such as Pd and Ru due to the formation of catalytically inactive alloys.

Other substitutes for the Ni-YSZ electrode are those based on oxide ceramics including fluorite- and perovskite-based structures [16,17]. Decent compatibility with oxide electrolytes, higher microstructural stability and resistance to redox cycling are the major benefits of this group of alternative anodes. On the other hand, the electronic conductivity of these oxides is several orders of magnitude lower than that of Ni-YSZ composite anodes. For the sake of comparison, the electronic conductivity of Ni-YSZ composite (50:50 vol.%), gadolinium doped ceria and yttrium doped strontium titanate are in the range of  $>1000$ ,  $0.1-1$ , and  $1-100 \text{ S cm}^{-1}$ , respectively, at  $800^\circ\text{C}$  under reducing conditions [16-18]. Furthermore, although carbon formation and poisoning by fuel impurities are generally less problematic with oxides, the catalytic activity of the majority of oxide anodes toward alternative fuels is relatively low [7,17].

Ever since Levy and Boudart [19] reported the resemblance between Pt and tungsten carbide in surface catalysis, the catalytic characteristics of Groups IV-VI carbides have been the subject of numerous studies [20]. These investigations have shown that the catalytic characteristics of these carbides are comparable with those of Pt-group precious metals [20], especially in reactions which deal with the transformation of C-H bonds of hydrocarbons. In particular, carbides of molybdenum and tungsten have been extensively investigated as electrocatalysts for low temperature fuel cells including proton exchange membrane (PEM) and direct methanol (DM) fuel cells [21-23]. These carbide ceramics,

however, have not been studied to any great extent as potential anode materials for SOFC applications.

To the best of our knowledge, the first attempt to study a tungsten carbide-based anode for SOFCs was made by Naoumidis et al. [24] in 1996. They reported that a WC-YSZ composite anode could potentially show a better performance than a Pt anode under 90% CO – 10% CO<sub>2</sub> as the fuel. While they expressed concerns about the stability of the carbide phase, they proposed that WC is thermodynamically stable at CH<sub>4</sub>/H<sub>2</sub>O > 0.2 and concluded that with such anodes, a reasonable yield of oxidation products can be obtained. Ten years later, stability of a variety of metal carbides was investigated to develop sulphur tolerant materials for SOFCs anodes [25]. It was shown that except for the carbides of Mo and W, other metal carbides cannot be used as alternative materials for SOFC anodes, solely because the corresponding oxides are much more stable under typical SOFC anode atmospheres.

Recently, we performed extensive symmetrical cell studies to investigate the electrochemical behavior of tungsten carbide-based materials for SOFC anodes [26]. The compelling attributes of WC which motivated us included catalytic resemblance between the carbide and precious metals, very high electronic conductivity (same order of magnitude as metals) and very high melting point (2870°C) which guarantees the microstructural stability during cell operation. Our preliminary results revealed that the ohmic polarization of WC-YSZ composite is comparable to that of Ni-YSZ cermets. The non-ohmic polarization, however, is relatively large and the incorporation of active electrocatalysts is unavoidable, particularly under methane fuel. We showed that addition of 10 wt% ceria and 3 wt% ruthenium into the

WC-YSZ electrode remarkably improves the electrochemical performance.

In this study, we report the performance of solid oxide fuel cells based on WC-YSZ composite anodes under mixed hydrogen-methane and methane fuels. First, the preparation of a conventional WC-YSZ and a WC infiltrated YSZ porous support is explained in detail. Then the cell performance of these conventional and infiltrated cells is compared and the effect of ceria and Ru addition into the carbide-based electrode is described. Lastly, the implications of these results and the challenges of WC-based anodes are discussed.

## **4.2. Experimental procedure**

### **4.2.1. Cell fabrication**

YSZ discs (FuelCellMaterials, Lewis Center, OH, diameter: 25 mm, average thickness: 0.3 mm) were used as the electrolyte as well as the mechanical support. Two different carbide-based anodes were studied in this work: conventional WC-YSZ composite- and infiltrated WC-YSZ-based materials. To prepare the former, tungsten carbide (WC) was obtained from Inframat Advanced Materials, Manchester, CT (nanocrystalline tungsten carbide powder, 99.95%, particle size: 200 nm, crystal size: 40-70 nm) and yttria-stabilized zirconia (YSZ) was supplied by FuelCellMaterials, Lewis Center, OH (yttria-stabilized zirconia 8 mole%, fine grade (YSZ8-U1), particle size: 300-500 nm). 7.26 g of the carbide and 2.74 g of the oxide (equal volume percentage of WC and YSZ) were put into a 50 mL polypropylene jar. 10 g of zirconia balls (Tosoh YTZ grinding media, 3 mm) and 10 mL of ethanol were added and they were mixed for an hour at 500 rpm using the planetary ball mill. Once the mixture was dried, 10 g of the laboratory-

made ink was added to 10 g of the composite powder and they were well mixed in the mortar and pestle for 30 min. WC-YSZ anodes (diameter: 10 mm, average thickness: 25  $\mu\text{m}$ ) were then screen printed onto the YSZ discs. The coated discs were dried at 150°C for 15 min and sintered at 1300°C for 3 hr under 1000 ppm CO<sub>2</sub>, balance CO.

In this study, for the infiltrated composite anodes and for the cathodes, a thin porous YSZ scaffold is used as a support. Calcined-milled YSZ (CYSZ) powder was used as the starting material to make the porous support. To prepare the CYSZ powder, as received YSZ (Tosoh TZ-8Y, Grove City, OH) was heat treated at 1500°C for 3 hr. 50 g of CYSZ, 300 g of zirconia balls (Tosoh YTZ grinding media, 5 mm) and 50 mL of distilled water were mixed in a 250 mL polypropylene jar and the mixture ball milled for 72 hr at 80 rpm. The suspension was then dried at 120°C for 24 hr and the dried agglomerates were manually ground in an alumina mortar and pestle for half an hour. To prepare CYSZ paste, 10 g of CYSZ powder, 0.5 g (20 vol.%) of polymethyl methacrylate ((PMMA), Microbeads<sup>®</sup>, Spheromers CA 6, Norway) as a pore former, 10 g of zirconia balls (Tosoh YTZ grinding media, 3 mm) and 10 mL of ethanol were added into a 50 mL polypropylene jar and they were mixed for an hour at 500 rpm using a planetary ball mill (Retsch, PM 100). After drying the mixture, a laboratory-made ink ( $\alpha$ -terpineol + 5 wt% ethylcellulose) was added (10 g powder + 10 g ink) and they were well mixed in the mortar and pestle for 30 min. YSZ coatings (diameter: 10 mm, average thickness: 25  $\mu\text{m}$ ) were then screen printed onto YSZ discs and sintered at 1300°C for 3 hr.

To prepare the WC infiltrated porous YSZ electrodes, ammonium metatungstate (AMT) was used (Inframat Advanced Materials, Manchester, CT) as the starting precursor. 1 g of distilled water was added to 3 g of the precursor in a 10 mL glass container. Using a

regular laboratory ultrasonic cleaner for 10 min, AMT was completely dissolved in the water to leave a clear solution. 0.15 g of Triton (X-45, Union Carbide Chemicals and Plastics Co. Inc., Danbury, CT) was then mixed into the solution to play a role as a surfactant. The solution was heated up to 100°C in an oil bath and this hot solution was infiltrated into the preheated (150°C) porous YSZ electrode coatings. The impregnated discs were then heat treated at 350°C for 15 min. This procedure was repeated (twice on average) until 20 vol.% WC was embedded into the YSZ network. To synthesize the carbide phase, the infiltrated discs were heated to 600°C in air. Ar was then introduced to flush out the air and lastly an 80% H<sub>2</sub> – 20% CH<sub>4</sub> atmosphere was introduced. The final heat treatment condition was 880°C for 12 hr. A heat treated coating was examined by X-ray diffraction (XRD, Rigaku Ultima IV) which confirmed the presence of a nano-sized WC phase along with YSZ.

To investigate the effect of other active electrocatalysts on the electrochemical performance of WC-YSZ cells, they were infiltrated with ceria and/or Ru. A 0.25M solution of cerium ammonium nitrate (Alfa Aesar) in ethanol was prepared as a precursor for ceria. The WC-YSZ support was infiltrated with the ceria solution using a micro-syringe and subsequently dried at 150°C for 15 min followed by a heat treatment at 350°C for another 15 min. The infiltration-heat treatment cycle was repeated 10 times to obtain 5 wt% ceria. Similarly, a 0.1M solution of RuCl<sub>3</sub> · xH<sub>2</sub>O (x≤1) (Sigma-Aldrich) in ethanol was prepared. The support was then impregnated by this solution using a micro-syringe and dried at 150°C for 15 min. The impregnation was repeated five times and the final Ru gain was about 1 wt%.

Since the focus of this work is on the anode, Pt was initially picked at first as the cathode of choice. Platinum paste was obtained from

Heraeus Materials Technology LLC, West Conshohocken, PA (OS2, CL11-5349). The cathode performance was, however, poor. Thus,  $\text{La}_{0.8}\text{Sr}_{0.2}\text{MnO}_3$  (LSM), as a well studied cathode material, was chosen to be infiltrated into the porous YSZ structure on the cathode side.  $\text{Mn}(\text{NO}_3)_2 \cdot x\text{H}_2\text{O}$ ,  $\text{La}(\text{NO}_3)_3 \cdot 6\text{H}_2\text{O}$ , and  $\text{Sr}(\text{NO}_3)_2$  from Alfa Aesar were used as the starting precursors to prepare a solution based on Pechini's method [27]. The molar ratio of metal cations, complexing agent (citric acid) and ethylene glycol in the solution was 1:4:4. A small amount of the solution was dried and then heated to 700°C in air. The synthesized powder was examined by XRD which confirmed the presence of LSM as the only phase. The thin porous support was repeatedly impregnated by incipient wetness (10 times, on average) until 20 vol.% LSM was embedded into the YSZ network with the LSM phase to be formed in-situ.

#### 4.2.2. Cell test

A laboratory made gold paste was used as a current collector (atomised gold powder, Technic Inc., Cranston, Rhode Island) on both cathode and anode sides. The anode side of the cell was sealed onto an alumina tube using a glass seal (Aremco 617). The anode electrode was exposed to humidified  $\text{H}_2$ , humidified  $\text{H}_2 - \text{CH}_4$  mixed and humidified  $\text{CH}_4$  atmospheres with a constant flow rate of 50 mL/min (a room temperature bubbler was used to humidify the fuels). Also, extra dry air flowed through the cathode electrode at a similar rate. The electrochemical behavior of the cells was studied by ac impedance spectroscopy, potentiodynamic analysis and potentiostatic analysis (Solartron frequency response analyzer 1255 in combination with a Solartron electrochemical interface 1287) at 800, 850 and 900°C on fuel cells with a four electrode configuration. Impedance measurements

were carried out under open circuit condition over a frequency range from 0.1 Hz to 100 kHz with a 10 mV ac perturbation.

#### 4.2.3. Cell characterization

The microstructure of the electrodes both before and after electrochemical testing was examined on fractured surfaces with a JEOL 6301F field emission scanning electron microscope (FE-SEM). Bulk phase study was done by XRD and surface analysis was performed by X-ray photoelectron spectroscopy (XPS) (Axis 165 X-ray photoelectron spectrometer, Kratos Analytical).

### 4.3. Results and Discussion

Conducting extensive symmetrical cell studies, we investigated the electrochemical behavior of WC-based anodes prior to this work [26]. To effectively study carbide-based anode materials, a reasonably active cathode had to be chosen. At first, a platinum cathode was picked. To solely characterize the performance of the Pt cathode, a Pt symmetrical cell was made. Figure 4.1 shows the ac impedance spectra of this symmetrical cell at 800 and 900°C. As clearly observed, the performance of such a cathode is rather poor. We then compared the symmetrical Pt cell with a symmetrical LSM infiltrated porous YSZ support cell, which is also illustrated in Fig 4.1. Since the performance of the latter is dramatically better, it was picked as the cathode of choice for the entire study.

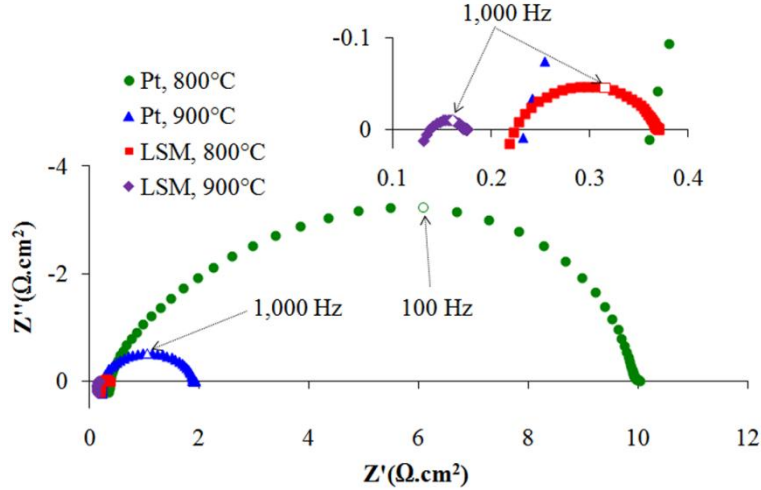


**Fig. 4.1.** Comparison between a conventional Pt cathode and a LSM infiltrated porous YSZ cathode.

Figure 4.2 shows the electrochemical performance of a conventional WC-YSZ and a WC infiltrated porous YSZ anode including (a) open circuit impedance spectra and (b) V-i characteristics and power densities at 800°C under humidified 80% H<sub>2</sub> – 20% CH<sub>4</sub> mixed atmosphere and humidified methane. As discussed elsewhere [26], the carbide phase is not stable under pure hydrogen fuel and sluggishly decomposes to tungsten metal. To preserve the carbide phase under open circuit condition, a slight amount of methane (>2.5%) must be introduced into the humidified hydrogen atmosphere. That is why humidified 80% H<sub>2</sub> – 20% CH<sub>4</sub> mixed atmosphere is used as a hydrogen rich fuel.

Using similar methodology, we have extensively studied the electrochemical behavior of symmetrical LSM infiltrated YSZ cathodes [28] and that of symmetrical WC-based anodes [26]. Considering the fact that the polarization resistance of the LSM cathode under OCP is very low (about 0.15 Ω cm<sup>2</sup>), the rather large polarization resistance of such a cell can be reasonably attributed to the anode electrode. It is noteworthy that the characteristics of the impedance spectra of the fuel

cell strongly resemble that of the symmetrical WC-based one. As observed in Figure 4.2, no matter whether the cell is conventional or infiltrated, the impedance comprises two semicircles: a small arc in the high frequency range and a relatively large arc in the low frequency range. This is also the case for both the mixed and methane atmospheres. McIntosh et al. [29] showed that the high frequency arc should be attributed to cathode processes. Similarly, the fact that running the cells under various fuels mainly affects the low-frequency lobe suggests that the small cathodic polarization is actually convoluted into the high-frequency arc.

In general, the performance of WC-YSZ anodes is relatively poor, particularly toward methane fuel. For example, the total electrode polarization resistance (the difference between the high-frequency and low frequency intercepts with the real axis) under mixed fuel at 800°C is 21.3 and 6.1  $\Omega \cdot \text{cm}^2$  for conventional and infiltrated cells, respectively (Fig. 4.2(a)). V-i characteristics of these cells also suggest that cells based on WC-YSZ anodes performed weakly. The maximum power densities at 800°C were 35 and 45  $\text{mW} \cdot \text{cm}^{-2}$  under mixed fuel, and as low as 10 and 15  $\text{mW} \cdot \text{cm}^{-2}$  under methane.

The comparison between conventional and infiltrated WC-YSZ, however, was really informative and several observations should be noted here. Firstly, although the amount of the carbide phase was much less in the infiltrated cell (20 vol.% as opposed to 50 vol.% in the conventional cell), the performance was better. Figure 4.3 shows the XRD spectra for a conventional WC-YSZ (50 vol.% WC) and an infiltrated one (20 vol.% WC). The remarkable broadening in WC diffraction peaks is due to a great decrease in carbide phase crystal size. The calculated crystal size of WC using XRD line broadening and the Scherrer equation was about 55 and 10 nm for conventional and

infiltrated samples, respectively. This suggests that the surface area of the latter should be considerably higher which can contribute to improved performance.

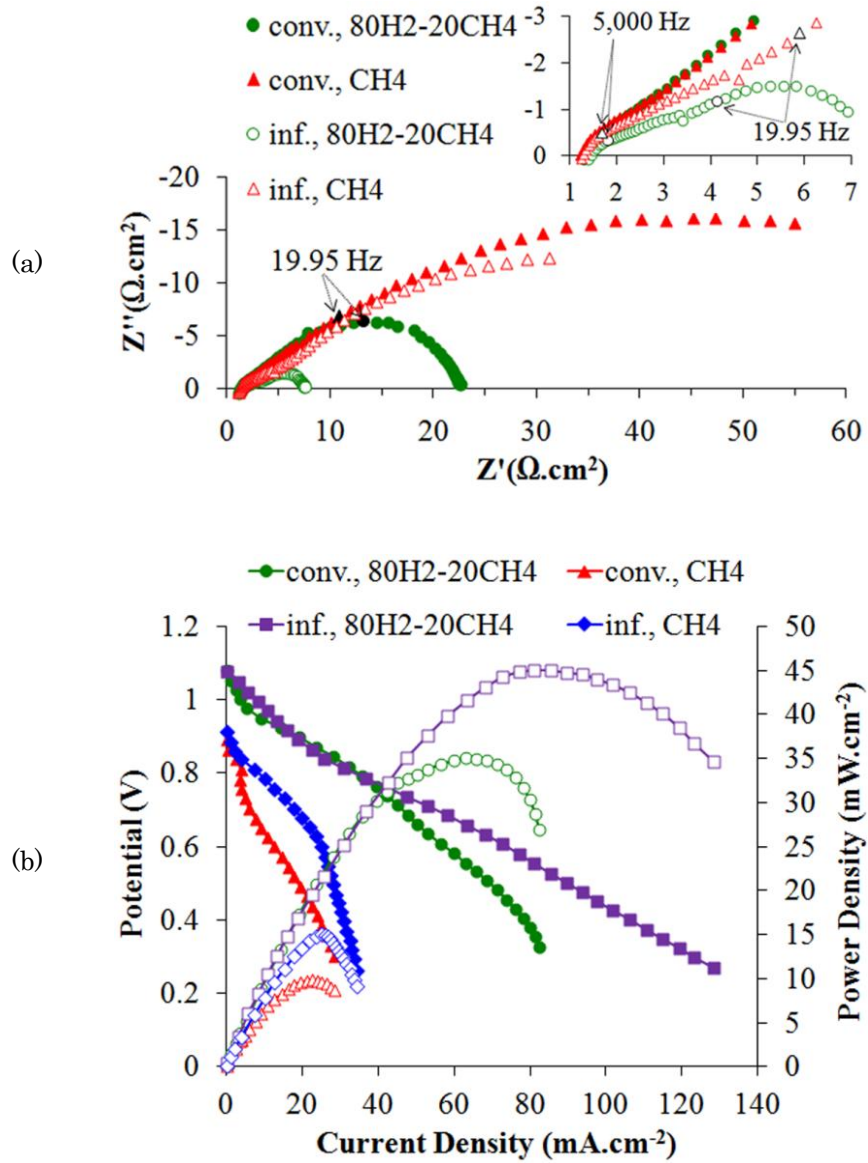


**Fig. 4.2.** Performance of cells with a conventional WC-YSZ composite anode and a WC-infiltrated porous YSZ anode at 800°C (a) Ac impedance spectra and (b) V-i characteristics.

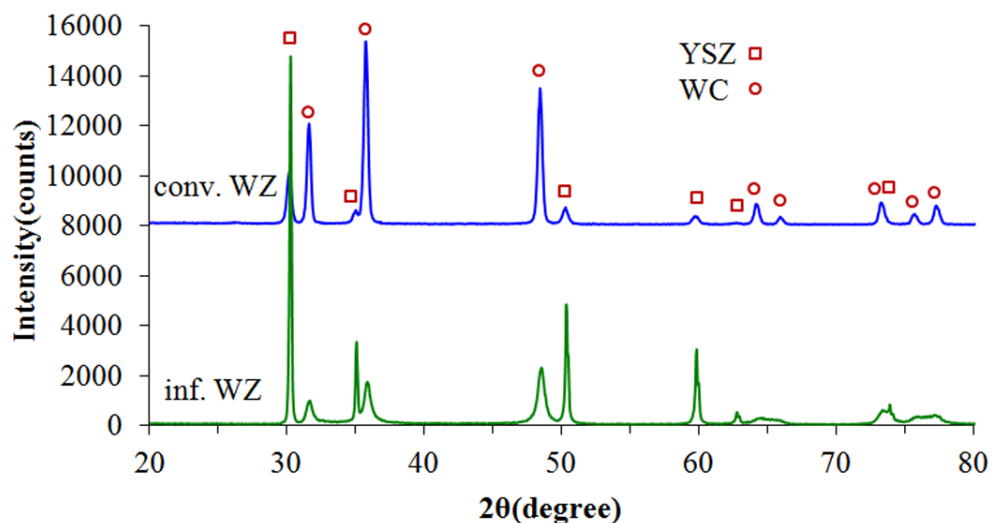


**Fig. 4.3.** XRD spectra of the conventional and infiltrated WC-YSZ composite.

In addition, the stability of conventional and infiltrated cells is quite different. Figure 4.4 shows how the power density varies over a period of 18 hr under potentiostatic condition (cell voltage = 0.7 V) in both conventional and infiltrated cells at 850°C in 80% H<sub>2</sub> – 20% CH<sub>4</sub> mixed fuel. While the conventional cell performed quite stably for the first hour, it experienced a noticeable power decrease over the next two hours and then stayed relatively constant. The infiltrated cell, on the other hand, showed a rapid initial drop in power density, followed by a recovery and stabilization at a higher power density than the conventional cell.

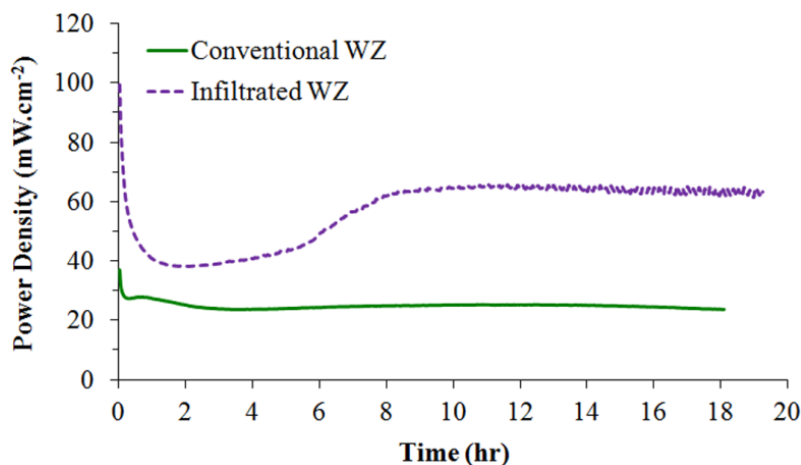


**Fig. 4.4.** Potentiostatic performance (0.7 V) of cells with the conventional WC-YSZ composite anode and a WC-infiltrated porous YSZ anode under humidified mixed fuel at 850°C.

The infiltrated cell, however, experienced a great power increase in the first half of the experiment followed by a stable performance in the second half. To cast light on this, the impedance spectra of these cells are illustrated in Figure 4.5 before and after the stability test. Comparing the impedance spectra, a remarkable increase in ohmic resistance is observed (from 0.8 to 1.65  $\Omega \cdot \text{cm}^2$ ) in the conventional cell (Fig. 4.5(a)). Also, as for the polarization arcs, a great increase is observed in the first semicircle (high frequency arc), while the second one (low frequency arc) is relatively unchanged. After this test, once the sample was cooled down and removed from the cell, the anode electrode was delaminated and detached from the electrolyte (Fig. 4.5(c)). Thus, the remarkable increase in ohmic resistance is essentially due to the WC-YSZ electrode delamination. Since the high frequency semicircle is attributed to charge transfer polarization corresponding to electron transfer and ion transfer processes occurring at the interfaces [30,31], such delamination also contribute to the marked increase in the high frequency arc.

On the other hand, the behavior of the infiltrated cell was different. As illustrated in Figure 4.5(b), the increase in ohmic resistance after the stability test is much lower. Since no tungsten oxide phase was detected in the carbide electrode after testing (to be shown later) and the infiltrated electrode was well attached to the electrolyte, such an increase in ohmic resistance is most probably due to contact resistance with the gold current collector. As opposed to the conventional cell, while the high frequency arc in the infiltrated sample is relatively unchanged, a rather large increase in the low frequency arc is observed. As discussed elsewhere [26], surface oxidation of the carbide phase is one of the two possible mechanisms of the fuel oxidation process. Before the sample is polarized, the fresh surface layer of the

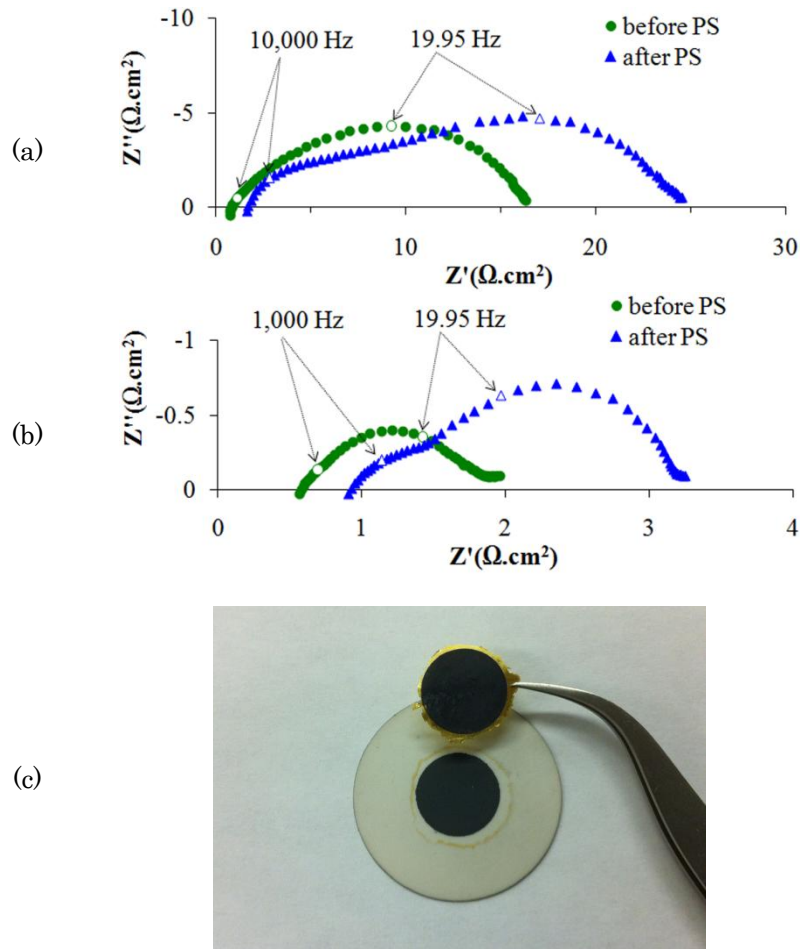
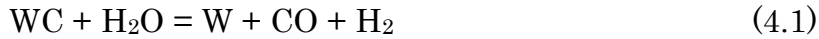


**Fig. 4.5.** (a) and (b) Ac impedance of a cell with conventional WC-YSZ composite anode and WC-infiltrated porous YSZ anode before and after a potentiostatic test under humidified mixed fuel at 800°C, (c) anode delamination in the conventional sample.

carbide nano-particles is very active toward the fuel. Once the cell is polarized for 18 hr, however, the carbide surface approaches an equilibrium oxidation state. That is why the low frequency arc which is predominantly attributed to non-charge transfer processes including surface reactions [30,32] experiences a rather large increase. This argument is more meaningful when power densities of this cell are considered which were 215 and 84.5  $\text{mW} \cdot \text{cm}^{-2}$  before and after the stability test at 850°C in mixed fuel, respectively (not shown here).

The XRD spectra of the delaminated conventional carbide electrode and the infiltrated one are shown in Figure 4.6. Interestingly, in both the conventional and infiltrated samples, nearly all of the WC phase decomposed to tungsten metal. Cheng et al. [25] explained that the Mo and W metals are more stable in the reducing SOFC anode atmosphere. They, however, considered hydrogen-based fuel. We previously discussed [26] that WC was not stable under hydrogen and decomposed to W. Accordingly, we utilized a 80% H<sub>2</sub> – 20% CH<sub>4</sub> mixed atmosphere not only to stabilize the carbide phase in the conventional cell, but also to synthesize tungsten carbide in the infiltrated cell. Thermodynamically, one possible reaction which leads to the decomposition of WC is:



The standard Gibbs free energy for this reaction at 850°C is +11.4 kJ·mol<sup>-1</sup> and the equilibrium partial pressure of CO is 0.009 atm. On the other hand, since the fuel atmosphere is humidified 80% H<sub>2</sub> – 20% CH<sub>4</sub>, a recarburization reaction may be written as follows:



Considering the partial pressure of methane and hydrogen, the Gibbs free energy for such reaction at 850°C would be -60.5 kJ·mol<sup>-1</sup> which is thermodynamically quite favourable. Thus, the fact that WC did decompose to W under polarization condition should be the inevitable corollary of kinetic factors. Note that such decomposition is responsible for the delamination of the carbide-based electrode in the conventional cell. Since the density of tungsten carbide and tungsten are 15.8 and 19.25 g·cm<sup>-3</sup>, respectively, decomposition causes a volume change of more than 20% and results in delamination of the anode electrode from the electrolyte. Figure 4.7 shows the anode/electrolyte interface for a partly delaminated WC-YSZ electrode. As can be readily observed, not

only is the anode layer detached from the electrolyte due to the internal stress caused by the volume change in the W-based phases, but several micro-cracks can also be detected within the YSZ particles! Although such decomposition also occurred in the infiltrated sample, the anode stayed well attached to the electrolyte. In the conventional WC-YSZ anode, the carbide phase is actually a structural component of the electrode. However, in the infiltrated cell, only porous YSZ contributes to the structural support and therefore, the volume change of infiltrated carbide particles does not affect the cell's integrity.

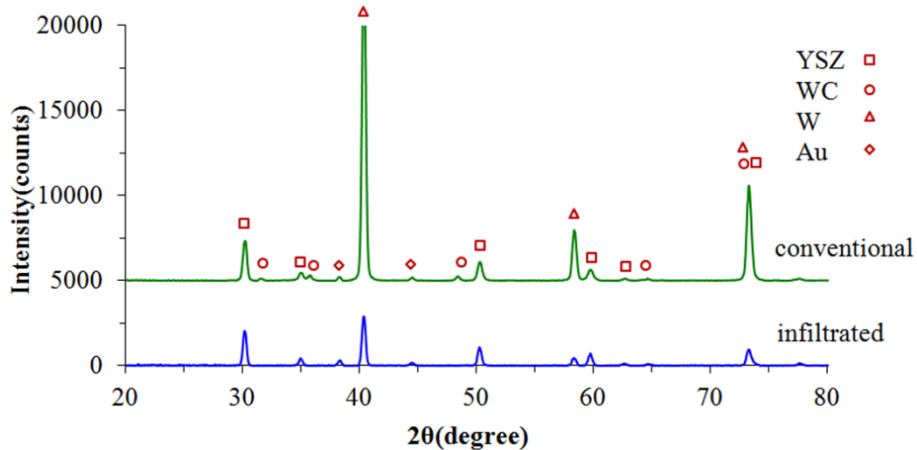


**Fig. 4.6.** XRD spectra of the conventional and infiltrated WC-YSZ composite after a potentiostatic test under humidified mixed fuel at 800°C.

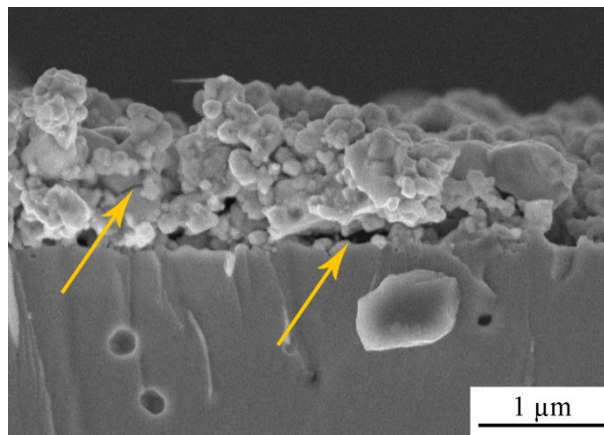


**Fig. 4.7.** SEM micrograph of the conventional WC-YSZ anode and YSZ electrolyte interface after a cell test.

When we considered investigating WC-based anode materials, one of the motivations was that we did not expect a carbide-based anode to promote carbon formation under hydrocarbon fuels. In practice, close visual inspection of the studied cells did not reveal any sign of carbon formation or coking under methane. The XPS spectra of carbon (C1s) in as-received WC powder and on a WC-YSZ anode surface is illustrated in Figure 4.8. The C1s spectrum of the former was fitted to two peaks including a carbidic type (BE = 283.0 eV, fwhm = 0.7 eV) and a graphitic type (BE = 284.7 eV, fwhm = 1.6 eV). The C1s spectrum of the latter, however, was fitted to three peaks including a carbidic type (BE = 283 eV, fwhm = 1 eV), a graphitic type (BE = 284.4 eV, fwhm = 1.7 eV) and an aromatic type (BE = 285 eV, fwhm = 4 eV). The formation of condensed aromatics has also been reported by others [33,34]. Considering the fact that the WC-YSZ electrode was tested in humidified methane for 12 hr at 800°C under open circuit condition, comparison between these two spectra confirms that coking is not promoted on the carbide phase.

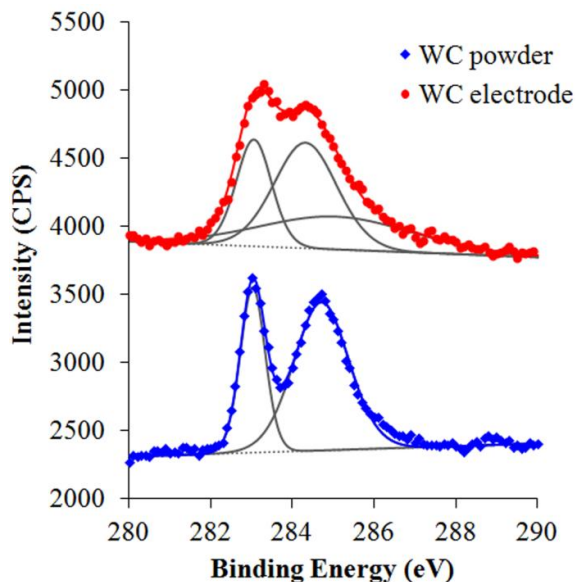


**Fig. 4.8.** XPS spectra of elemental carbon (C1s) in as-received WC powder and a WC-YSZ anode surface after cell test under humidified methane at 800°C.

As discussed above, the performance of the WC-YSZ anodes is rather poor particularly toward methane fuel and needs to be improved by incorporation of active electrocatalysts. Furthermore, it has been previously shown [26] that not only can incorporation of electrocatalysts contribute to an improved performance, but it can also affect the stability of the carbide phase. Figure 4.9 illustrates the impedance spectra of an infiltrated WC-YSZ cell which was impregnated with 5 wt.% ceria and 1 wt.% Ru (inf-RCWZ) at 800, 850 and 900°C under humidified 80% H<sub>2</sub> – 20% CH<sub>4</sub> mixed atmosphere and humidified methane, measured at open circuit voltage. As expected, a great improvement in non-ohmic polarization of the ceria-Ru infiltrated cell is observed particularly under methane. For example, the total electrode polarization (difference between the high-frequency and low frequency intercepts with the real axis) under methane at 800°C is 3.0 and 60.7 Ω·cm<sup>2</sup> (the low frequency intercept was measured by a fit semicircle) for the infiltrated WC-YSZ cell, respectively, with and without ceria-Ru. It is noteworthy that the primary change that occurred upon the addition of ceria-Ru was a dramatic decrease in the semicircle located in the lower frequency range (<100 Hz).

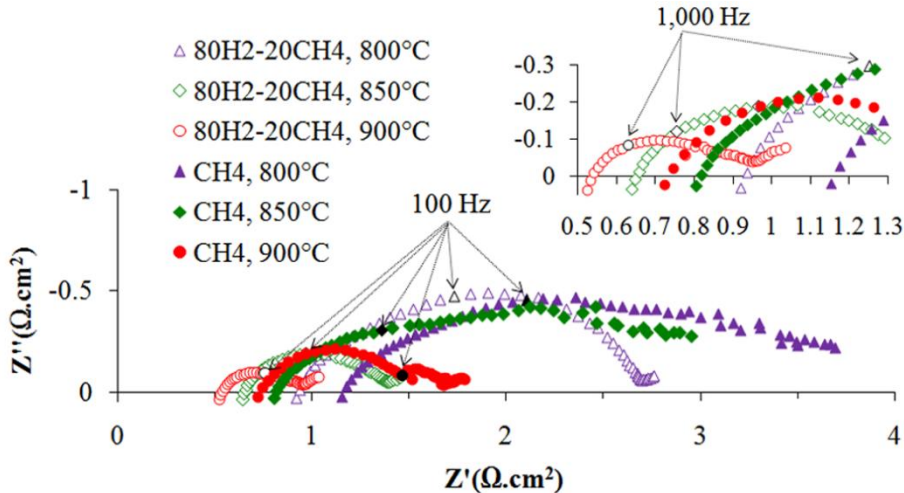


**Fig. 4.9.** Ac impedance spectra of a cell with a ceria-Ru promoted WC-infiltrated porous YSZ anode.

The corresponding V-i polarization and power density curves of infiltrated RCWZ are shown in Figure 4.10 under (a) mixed atmosphere and (b) methane. Note that these polarization measurements were all made after the cells stabilized to be certain of the reproducibility of the results. This is important because, in some cases, the performance was almost twice as high before the cell stabilized. In order for cells to stabilize, they operated under potentiostatic condition (0.7 V) for a period of 24 hr at 850°C in the mixed atmosphere. Furthermore, the ohmic resistance of the relatively thick electrolyte was not compensated in any of the reported results. Interestingly, incorporation of only 5 wt% ceria and 1 wt% Ru into the infiltrated WC-YSZ anode greatly improved the performance. For example at 850°C, the power density increased from 85 to 185 mW cm<sup>-2</sup> under hydrogen-rich fuel and from 19 to 58 mW cm<sup>-2</sup> under the methane fuel. As Gross et al. [35] pointed out, compared to higher molecular weight hydrocarbons, methane is rather difficult to activate. Thus, it is clear that the performance of the carbide-based cell under methane fuel is essentially limited by the ability of the anode to break the strong C-H bonds. While the WC-YSZ anode was not effective in methane activation, the Ru-CeO<sub>2</sub>-WC-YSZ anode performed with a reasonable activity towards methane fuel.

Figure 4.11 compares the measured open circuit voltage of the infiltrated RCWZ under humidified methane and the calculated OCV for hydrogen oxidation from the Nernst equation. As observed, the measured OCV values for methane fuel linearly decrease with increasing temperature. Interestingly, the measured OCV agrees reasonably well with the calculated hydrogen oxidation reaction. McIntosh et al. [36], and Liu and Barnett [37] showed that OCV measurements can provide some insight into the anode reactions.

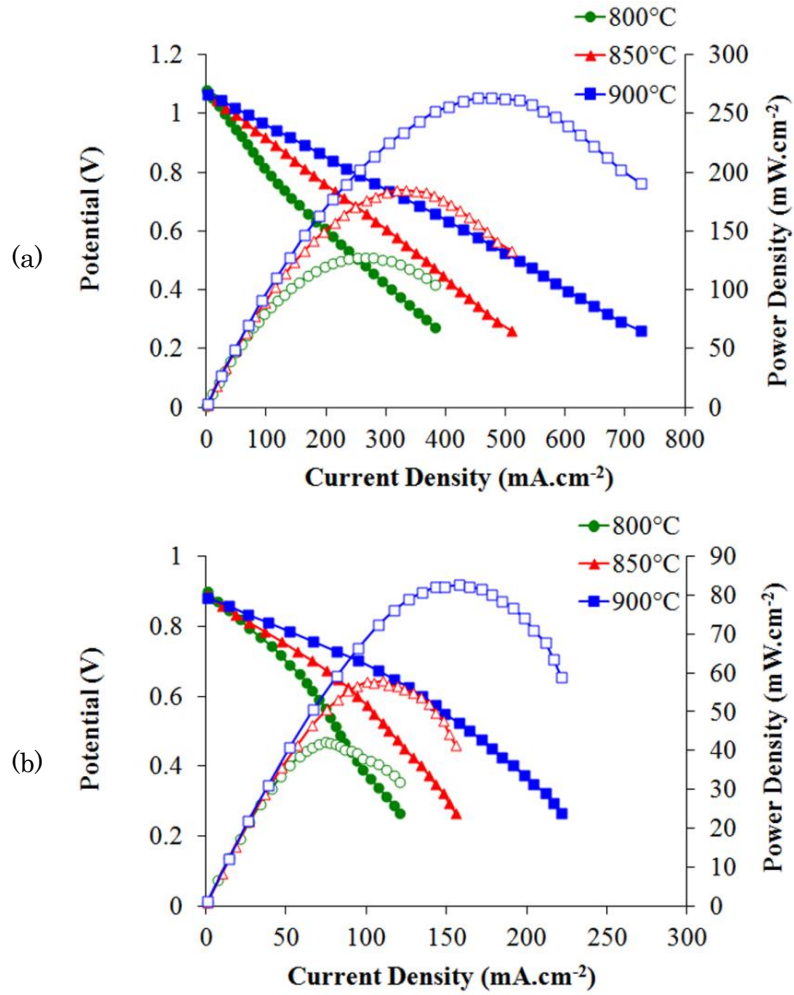


**Fig. 4.10.** V-i characteristics and power densities of a cell with the ceria-Ru promoted WC-infiltrated porous YSZ anode under (a) H<sub>2</sub>-CH<sub>4</sub> mixed atmosphere and (b) CH<sub>4</sub>.

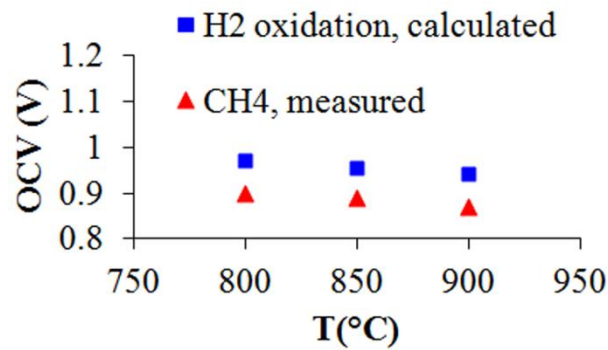


**Fig. 4.11.** Comparison between the measured OCV of a cell with the ceria-Ru promoted WC-infiltrated porous YSZ anode under humidified methane and the calculated OCV for hydrogen oxidation from the Nernst equation.

McIntosh et al. [36] argued that since the measured OCVs for a C-Pd-CeO<sub>2</sub>-YSZ anode were higher than that of calculated ones over the range of steam-reforming H<sub>2</sub>:H<sub>2</sub>O ratios, an equilibrium reaction with reformat products was not theoretically possible. In our case, however, not only were the measured OCVs at various temperatures smaller ( $\Delta V \sim 0.08$  V), they also followed a similar trend with increasing temperature. Additionally, our thermodynamic calculation revealed that if only 16% of the H<sub>2</sub>O participates in the steam-reforming reaction:



the OCV would decrease from 0.98 to 0.90 V at 800°C. Although the water content in humidified methane was just 3%, the required H<sub>2</sub>O conversion was low enough to possibly occur over the Ru-CeO<sub>2</sub>-WC-YSZ anode. It is noteworthy that, in practice, more than one anode reaction may simultaneously occur and the experimental OCV may be established by an equilibrium composition.

Figure 4.12 shows SEM micrographs (low and high magnification) of the Ru-CeO<sub>2</sub>-WC-YSZ anode after a 72 hr fuel cell test at different temperatures and under various fuels. WC, ceria and Ru nanoparticles are supported on a porous YSZ backbone. There is a well connected nano-sized WC network intimately seated on the YSZ support. Although Cheng et al. [25] mentioned that a high processing temperature could pose a challenge in Mo- and W-based carbides, it is shown here that the infiltration technique can be effectively used to address the issue. Note that since the carbide phase was formed in-situ, the maximum treatment temperature was only 900°C. EDS chemical analysis on more than 10 spots confirmed that ceria and Ru were well distributed over the WC-YSZ composite. Overall, the

normalized wt% of ceria and Ru were 3.9 and 0.94, respectively. Also, the chemical analysis helped to distinguish among the infiltrated particles. In the high magnification micrograph, WC is the nano-sized well connected network, ceria nano-particles are the smallest (10-20 nm), and Ru particles are rather larger and less populated.

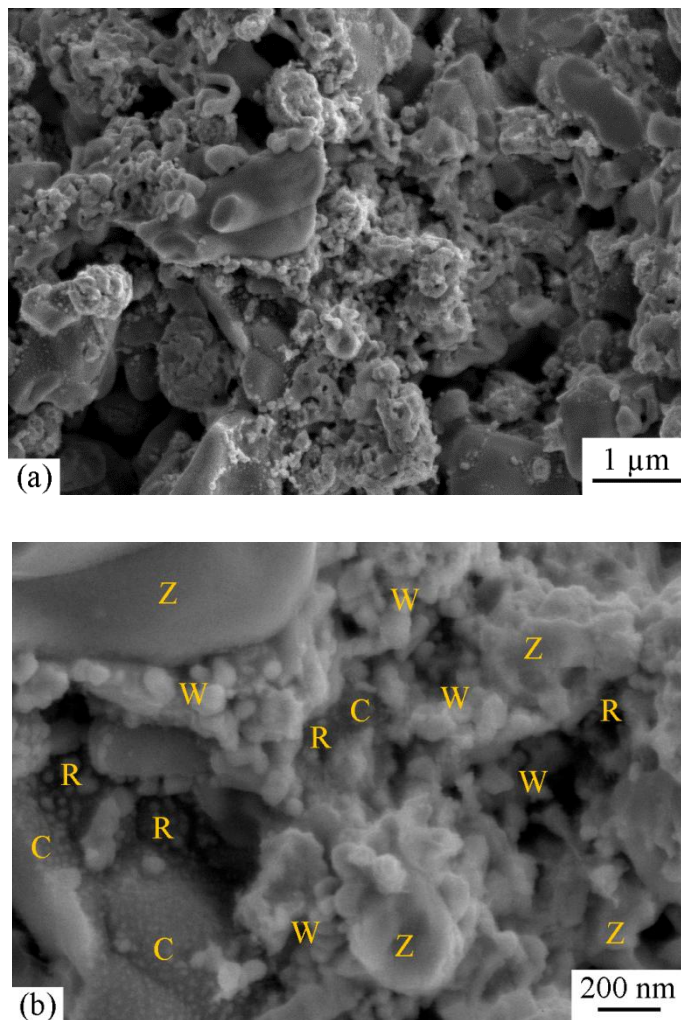


**Fig. 4.12.** SEM micrographs of the ceria-Ru promoted WC-infiltrated porous YSZ anode (R: Ru, C: CeO<sub>2</sub>, W: WC, and Z: YSZ).

Addition of ceria and Ru electrocatalysts also affects stability of the carbide phase. It was explained earlier that in a conventional WC-YSZ cell, the performance degraded over time during a 24 hr potentiostatic test. Based on the post-test analysis, the performance degradation was attributed to gradual delamination of the anode electrode due to the carbide phase decomposition. The performance of a cell with a ceria-Ru impregnated conventional WC-YSZ (con-RCWZ) anode at 850°C under humidified 80% H<sub>2</sub> – 20% CH<sub>4</sub> mixed fuel is illustrated in Figure 4.13(a). As opposed to the cell with no ceria-Ru, the con-RCWZ cell performed with reasonable stability over a period of 48 hr. Figure 4.13(b) shows the OCV impedance spectra of the cell before and after the stability test. Interestingly, while the high frequency range arc was almost unchanged, the low frequency range semicircle decreased markedly after the test. Note that a slight increase in the ohmic resistance (from 0.73 to 0.91 Ω·cm<sup>2</sup>) is most probably due to sluggish sintering of gold particles in the current collector film. As the stability result implied, in contrast with the WZ cell, no delamination occurred in the con-RCWZ cell.

Post phase analysis of the cell revealed that tungsten carbide remained as the major phase besides YSZ. The XRD spectrum of the con-RCWZ cell is shown in Figure 4.14. The amount of tungsten metal was quite minor. In addition, a small amount of WO<sub>2</sub> phase was detected. As discussed earlier, our thermodynamic calculation indicated that the carbide phase remains stable under the mixed fuel and we attributed the decomposition of WC to kinetic factors. The fact that the carbide phase remained rather stable in the presence of ceria-Ru electrocatalysts could also support this argument.

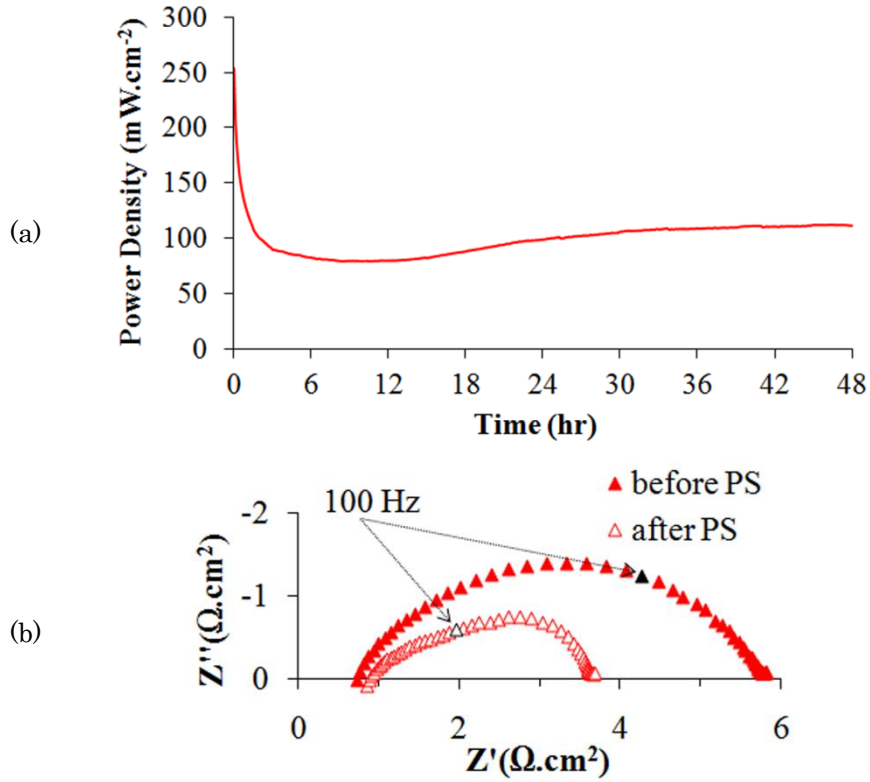


**Fig. 4.13.** (a) Potentiostatic performance (0.7 V) of a cell with the ceria-Ru impregnated conventional WC-YSZ anode at 850°C under mixed fuel, (b) OCV impedance spectra of the cell before and after the stability test.

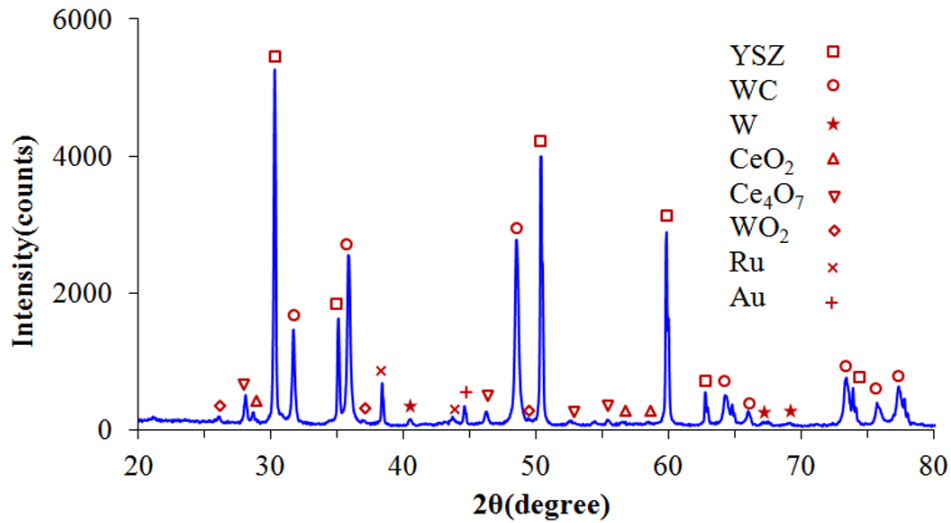


**Fig. 4.14.** XRD spectra of a cell with the ceria-Ru impregnated conventional WC-YSZ anode after a potentiostatic test under humidified mixed fuel at 850°C.

Undoubtedly, a key feature of SOFCs in comparison to other fuel cell systems is the ability to internally reform hydrocarbon fuels and to then utilize the produced H<sub>2</sub> and CO, along with the possibility to directly utilize hydrocarbon fuels (direct oxidation). Nevertheless, the build-up of carbon caused by hydrocarbon pyrolysis is a fundamental challenge associated with hydrocarbon fuel utilization particularly with Ni-based anodes as the state-of-the-art anode materials [38,39]. Our primary goal in studying carbide-based materials as alternative anodes for SOFC application was, therefore, to directly utilize hydrocarbons. Knowing the fact that the catalytic attributes of Groups IV-VI carbides are highly similar to those of Pt-group precious metals [20], particularly in reactions which deal with the transformation of C-H bonds of hydrocarbons, we were intrigued to investigate how it would perform under hydrocarbon fuels. This, nonetheless, was not the only motivation to study WC. Although it is a ceramic, the electronic conductivity of tungsten carbide is similar to that of metals ( $0.52 \times 10^5$  S·cm<sup>-1</sup> for WC vs.  $1.43 \times 10^5$  S·cm<sup>-1</sup> for Ni). Moreover, the very high melting point of WC (2870°C) could virtually guarantee the microstructural stability over long-term operation at high temperatures.

As shown earlier, however, the WC-YSZ anode performed very poorly under methane. Although the carbide-infiltrated anode showed a slight performance improvement, it was still not promising. Addition of highly active electrocatalysts was then essential to enhance the performance. The incorporation of 5 wt% ceria and 1 wt% Ru into the carbide-based anode promoted the performance by a factor of 3. We are aware that these results are still below some reported values in the literature [35,40,41]. However, considering the fact that our cells were electrolyte supported and our results were not compensated, we feel

there is certainly room for increasing the power output. For example, the synthesis conditions of the carbide phase should be optimized. Moreover, potentially more effective electrocatalysts (such as doped ceria and/or Pd) need to be investigated. Also, since methane is known to be difficult to activate, other fuels in which the C-H bond can be broken more easily should also be studied.

In addition to poor performance, instability of the carbide phase posed another challenge which perhaps was even more important. Trying to thoroughly understand the stability issue, we previously [26] performed several ex-situ tests in which WC was exposed to various reforming gases, including H<sub>2</sub> and CO as reducing and carburizing gases and H<sub>2</sub>O and CO<sub>2</sub> as oxidizing gases. The ex-situ results showed that WC remained the major phase. Only a very minor amount of WO<sub>x</sub> (3-4 wt% when (H<sub>2</sub>O + CO<sub>2</sub>)/(H<sub>2</sub> + CO) was as high as 2.63) was detected and no decomposition from carbide to metal occurred. In the present work, we tested more than 20 different cells including conventional WC-YSZ, infiltrated WC-YSZ, conventional WC-YSZ with ceria-Ru and infiltrated WC-YSZ with ceria-Ru. Depending on the fuel atmosphere, polarization condition and temperature, the W-based components were quite varied. Earlier, we presented some of the post-analysis XRD results (Fig. 4.6 and 4.14). Table 4.1 presents a conclusive summary of the phase analysis results.

**Table 4.1.** Summary of the phase analysis after fuel cell test (M: major phase, m: minor phase).

W-based component	WC-YSZ		Ru-CeO <sub>2</sub> -WC-YSZ	
	H <sub>2</sub> -CH <sub>4</sub>	CH <sub>4</sub>	H <sub>2</sub> -CH <sub>4</sub>	CH <sub>4</sub>
WC	m	m	M	M
W	M	M	m	m
WO <sub>x</sub>	-	m	-	m

Several important points should be noted from the data in Table 4.1. First, in the WZ-YSZ anode, a major phase change occurred from carbide to metal. Such a major phase change imposes serious mechanical stress on the anode/ electrolyte interface due to a 20% volume change within the anode microstructure and, therefore, results in anode/electrolyte delamination. Second, although such a major phase change similarly occurred in the infiltrated WC-YSZ anode, it did not bring about any delamination (based on SEM analysis). Note that in infiltrated WC-YSZ, the carbide is supported over a consolidated YSZ backbone and essentially does not have any structural attributes. Thus, the volume change is not problematic anymore and no delamination is observed. Third, addition of ceria-Ru electrocatalyst effectively preserved WC as the major phase and both metal and oxide phases remained minor. Finally, no oxide phase was detected in samples tested under hydrogen-methane mixed fuel, while a minor oxide phase was nearly always present in samples tested under methane.

Recently, many attempts have been made to utilize WC and Mo<sub>2</sub>C for steam and dry reforming of methane [42-45]. Claridge et al. [42] showed that at atmospheric pressure, the carbide catalyst deactivated due to oxidation reactions and indicated that such deactivation was predominantly governed by kinetics. They also indicated that methane conversion over a carbide catalyst can be explained by two different pathways: a redox mechanism and a noble metal mechanism, which both must participate in the overall reforming reaction. Here, with a similar approach, we list possible reactions for electrochemical oxidation of hydrogen and methane over WC. Once the cell is polarized, the following reactions could possibly happen on the carbide surface:





In the redox mechanism, once the charge transfer reaction of the oxygen ion takes place, the corresponding oxygen atom ( $\text{O}^*$ ) adsorbs on the carbide surface and reacts with the carbon in the carbide surface (equation 4.9). A carbon vacancy ( $\text{W}_-$ ) is created as a result of this reaction. The vacancy is then filled with either carbon or oxygen (equations 4.10 and 4.11). The adsorbed oxygens ( $\text{O}^*$ ) may also react with the active carbon species ( $\text{C}^*$  from equation 4.6), which is known as the noble metal mechanism (equation 4.8). Note that in the latter mechanism, the surface carbon atoms from the carbide phase are not involved in the mechanism and the carbide phase remains stable.

In the conventional WC-YSZ anode, since a major amount of the carbide phase was decomposed to tungsten metal (Fig. 4.6), it can be reasonably concluded that the rate of reactions 4.9 and 4.12 is greater than that of reactions 4.10 and 4.11. In the ceria-Ru infiltrated WC-YSZ electrode, however, the carbide remained as the major phase and the detected metal and oxide phases were very minor. Accordingly, one can conclude that the addition of ceria-Ru could highly enhance the recarburization reaction via equation 4.10, and/or promote the noble metal mechanism to protect carbon atoms in WC (equation 4.8).

Since, to the best of our knowledge, the current work is one of the initial investigations on potential application of carbide-based materials for SOFC anodes, a reasonable question to be addressed is how promising WC could be as an SOFC anode alternative. Obviously, the major advantages of WC include very high electronic conductivity, great stability at high operating temperature and resistance to carbon formation. In addition, compatibility with precious metals such as Pd and Ru, which are excellent catalysts for hydrocarbon oxidation, can be very beneficial (as is not the case for Cu-based anodes, for example). However, as reported here, although catalytic resemblance between WC and precious metals is well acknowledged [20] and clearly can be quite advantageous, the WC-based anode did not show reasonable performance toward methane fuel on its own and needed to be promoted by other electrocatalysts. Furthermore, since any major phase change from the carbide to either the metal or oxide could irreversibly degrade the performance, stability of WC can pose a serious challenge.

Based on this study, we think the carbide infiltrated YSZ support can be reasonably considered as a foundation for future studies. First, with a very simple and practical infiltration technique, more than 20 vol.% of the carbide can be incorporated into the porous support. Second, it eliminates the need for a high processing temperature. Third, since the final carbide network is essentially nano-sized, the performance can be promoted. Finally, if any phase change occurs in the carbide phase, the integrity of the YSZ backbone remains intact and a potential permanent degradation can be avoided.

#### 4.4. Conclusions

The following conclusions could be drawn from the current study:

- I. Conventional WC-YSZ composites cannot be considered as a potential alternative anode for direct methane utilization. Not only do they show rather poor performance under methane, but they also experience a major phase change resulting in anode/electrolyte delamination.
- II. Cells with a WC infiltrated YSZ support show a slightly better performance relative to those with conventional WC-YSZ. They also perform stably and tolerate the internal stress caused by any phase change in WC.
- III. Incorporation of 5 wt% ceria and 1 wt% Ru significantly improves the performance. Also, the presence of ceria-Ru can effectively preserve WC so that it does not go through a major phase change.
- IV. The WC infiltrated YSZ support can be considered as a foundation for further investigation into carbide-based anode materials.

## References

- [1] A. Atkinson, S. Barnett, R. J. Gorte, J. T. S. Irvine, A. J. McEvoy, M. Mogensen, S. C. Singhal, J. M. Vohs, *Nat. Mater.* 3 (2004) 17.
- [2] Z. Cheng, J. H. Wang, Y. M. Choi, L. Yang, M. C. Lin, M. Liu, *Energy Environ. Sci.* 4 (2011) 4380.
- [3] A. J. Jacobson, *Chem. Mater.* 22 (2010) 660.
- [4] C. Sun, U. Stimming, *J. Power Sources* 171 (2007) 247.
- [5] J. B. Goodenough, Y. H. Huang, *J. Power Sources* 173 (2007) 1.
- [6] W. Z. Zhu, S. C. Deevi, *Mater. Sci. Eng. A* 362 (2003) 228.
- [7] M. D. Gross, J. M. Vohs, R. J. Gorte, *J. Mater. Chem.* 17 (2007) 3071.
- [8] M. L. Toebes, J. H. Bitter, A. J. van Dillen, K. P. de Jong, *Catal. Today* 76 (2002) 33.
- [9] M. Cimenti, J. M. Hill, *Energies* 2 (2009) 377.
- [10] K. Haga, S. Adachi, Y. Shiratori, K. Itoh, K. Sasaki, *Solid State Ionics* 179 (2008) 1427.
- [11] S.P. Jiang, S.H. Chan, *J. Mat. Sci.* 39 (2004) 4405.
- [12] D. Sarantaridis, A. Atkinson, *Fuel Cells* 7 (2007) 246.
- [13] S. McIntosh, R. J. Gorte, *Chem. Rev.* 104 (2004) 4845.
- [14] H. Kim, S. Park, J. M. Vohs, R. J. Gorte, *J. Electrochem. Soc.* 148 (2001) A693.
- [15] R. J. Gorte, J. M. Vohs, *J. Catal.* 216 (2003) 477.
- [16] J. W. Fergus, *Solid State Ionics* 177 (2006) 1529.
- [17] S.W. Tao and J.T.S. Irvine, *Chem. Rec.* 4 (2004) 83.
- [18] N. Q. Minh, *J. Am. Ceram. Soc.* 76 (1993) 563.
- [19] R. B. Levy and M. Boudart, *Science* 181 (1973) 547.
- [20] H. H. Hwu, J. G. Chen, *Chem. Rev.* 105 (2005) 185.
- [21] Y. Hara, N. Minami, H. Itagaki, *Appl. Catal. A* 323 (2007) 86.

- [22] D. J. Ham, Y. K. Kim, S. H. Han, J. S. Lee, *Catal. Today* 132 (2008) 117.
- [23] R. Ganesan, D. J. Ham, J. S. Lee, *Electrochem. Comm.* 9 (2007) 2576.
- [24] A. Naoumidis, F. Tietz, G. Stochniol, A. Gupta, T. Hauber, *Proceedings of the 2nd European Solid Oxide Fuel Cell Forum, Oberrohrdorf, Switzerland (1996)* 727.
- [25] Z. Cheng, S. Zha, M. Liu, *J. Electrochem. Soc.* 153 (2006) A1302.
- [26] A. Torabi, T. H. Etsell, N. Semagina, Partha Sarkar, *Electrochim. Acta* 67 (2012) 172.
- [27] M. P. Pechini, U.S. Patent No. 3,330,697 (1967).
- [28] A. Torabi, A. R. Hanifi, T. H. Etsell, P. Sarkar, *J. Electrochem. Soc.* 159 (2011) B1.
- [29] S. McIntosh, J. M. Vohs, R. J. Gorte, *J. Electrochem. Soc.* 150 (2003) A1305.
- [30] S. B. Adler, *Solid State Ionics*, 111 (1998) 125.
- [31] T. L. Reitz, H. Xiao, *J. Power Sources* 161 (2006) 437.
- [32] Q. A. Huang, R. Hui, B. Wang, J. Zhang, *Electrochim. Acta* 52 (2007) 8144.
- [33] F. Larachi, H. O. Hassani, M. C. Iliuta, B. P. A. Grandjean, P. H. McBreen, *Catal. Lett.* 84 (2002) 183.
- [34] H. O. Hassani, S. Rakass, N. Abatzoglou, P. Rowntree, *J. Power Sources* 171 (2007) 850.
- [35] M. D. Gross, J. M. Vohs, R. J. Gorte, *J. Electrochem. Soc.* 154 (2007) B694.
- [36] S. McIntosh, J. M. Vohs, R. J. Gorte, *Electrochem. Solid-State Lett.* 6 (2003) A240.
- [37] J. Liu, S. A. Barnett, *Solid State Ionics* 158 (2003) 11.
- [38] C. M. Finnerty, N. J. Coe, R. H. Cunningham, R. M. Ormerod, *Catal. Today* 46 (1998) 137.

- [39] R. Kikuchi, N. Koashi, T. Matsui, K. Eguchi, T. Norby, J. Alloys Compd. 408-412 (2006) 622.
- [40] Y. Lin, Z. Zhan, J. Liu, S. A. Barnett, Solid State Ionics 176 (2005) 1827.
- [41] Y. Nabae, I. Yamanaka, M. Hatano, K. Otsuka, J. Electrochem. Soc. 153 (2006) A140.
- [42] J. B. Claridge, A. P. E. York, A. J. Brungs, C. Marquez-Alvarez, J. Sloan, S. C. Tsang, M.L.H. Green, J. Catal. 180 (1998) 85.
- [43] A. R. S. Darujati, D. C. LaMont, W. J. Thomson, Appl. Catal. A 253 (2003) 397.
- [44] D. C. LaMont, A. J. Gilligan, A. R. S. Darujati, A. S. Chellappa, W. J. Thomson, Appl. Catal. A 255 (2003) 239.
- [45] J. Sehested, C. J. H. Jacobsen, S. Rokni, J. R. Rostrup-Nielsen, J. Catal. 201 (2001) 206.

## Chapter 5

# Nickel Modified Tungsten Carbide-based Anode Materials for Direct Utilization of Methane in Solid Oxide Fuel Cells

### 5.1. Introduction

Fuel flexibility and use of existing fuel infrastructure to bridge the hydrogen availability gap is perhaps the most important advantage of solid oxide fuel cells (SOFCs). In principle, an SOFC can operate on any combustible fuel such as hydrocarbons; as a matter of fact, direct utilization of hydrocarbons could facilitate commercialization of SOFCs and improve their efficiency. In practice, however, exploiting such great benefit is yet to be accomplished mainly due to the incompatibility of the Ni-YSZ composite, as the-state-of-the-art fuel electrode, with hydrocarbon fuels [1]. Nickel is a renowned catalyst for pyrolysis of hydrocarbon fuels leading to formation of carbon fibers [2,3]. The undesirable complications associated with the buildup of

carbon on Ni includes blocking of active sites on the anode, loss of nickel catalyst, and loss of structural integrity [4].

In spite of such a serious drawback, Ni-based anodes are not easily given up not only because of their unrivalled intrinsic characteristics including excellent catalytic activity, high electronic conductivity and great chemical stability with respect to the electrolyte, but also for their practical attributes including relative ease of fabrication, adequate mechanical strength and low cost [5,6]. Therefore, numerous attempts have been made to modify Ni-based anodes in order to overcome the challenge of incompatibility with hydrocarbon fuels. Liu and Barnett [7] suggested that a conventional Ni-YSZ anode supported cell can be compatible with humidified methane and natural gas as long as the operating temperature remains below 700°C and the cell is operated under high current densities. They, however, emphasized that these cells are not viable at higher operating temperatures and under open circuit condition. Kim et al. [8] modified nickel by alloying with copper and showed that whereas carbon formation is suppressed to a great extent, the performance is markedly compromised. Others [9,10] reported stable performance in cells with Sn modified Ni-based anodes under hydrocarbon fuels. In addition to modifying the Ni catalyst itself, incorporation of gadolinium doped ceria (GDC) into a Ni-based anode was reported [11] to be effective in suppressing carbon deposition.

Another practical approach to directly utilize hydrocarbon fuels is to develop alternative anode materials. These mainly include ceramic-metal composites and oxide ceramics which have been well reviewed over the past decade [5,6,12-15]. There are, however, several important limitations to these alternatives [16,17] including poor catalytic activity toward fuels, insufficient electronic conductivity (particularly

for oxides), low chemical and/or microstructural stability at higher operating temperatures (particularly for cermets) and fabrication difficulties.

The catalytic behavior of Groups IV-VI carbides has been well appreciated [18]. Molybdenum and tungsten carbides have attracted a lot of interest not only as new catalysts for the conversion of methane to synthesis gas [19,20], but also as electrocatalysts for low temperature fuel cells including proton exchange membrane (PEM) and direct methanol (DM) fuel cells [21-23]. They, however, have not been investigated to any great extent as alternative anodes for SOFC applications. Recently, we have done extensive studies on WC-based anodes as a candidate for direct hydrocarbon utilization including half cell and fuel cell analysis as well as ex-situ experiments [24,25]. Based on this work, WC-based anodes show very good electronic conductivity. They also do not promote the formation of carbon fibers under methane fuel at temperatures as high as 850°C. On the other hand, WC is not a sufficiently active catalyst toward methane and needs to be modified. Stability of the carbide phase poses another important challenge, too. We showed that when a WC-based anode is modified by 1 wt% Ru and 5 wt% CeO<sub>2</sub>, not only is the cell performance significantly boosted, but the stability of WC is highly improved.

In the current work, the performance of solid oxide fuel cells based on Ni-CeO<sub>2</sub>-WC-YSZ (NCWZ) composite anodes under mixed hydrogen-methane and methane fuels is investigated. First, a symmetrical cell based on a NCWZ electrode is considered to study the half cell electrochemical behavior toward methane under open circuit condition. Then, the performance of a fuel cell based on Ni-CeO<sub>2</sub>-WC-YSZ anode/YSZ electrolyte/LSM-YSZ cathode is described and the influence of Ni on the chemical stability of the carbide phase is discussed.

Finally, the effect of oxidation-reduction-re carburization cycling on the electrochemical performance and structural integrity of the cell is studied.

## 5.2. Experimental Procedure

### 5.2.1. Cell fabrication

YSZ discs (FuelCellMaterials, Lewis Center, OH, diameter: 25 mm, average thickness: 0.3 mm) were used as the electrolyte as well as the mechanical support. A thin porous YSZ scaffold is used as a support for the anode and cathode electrodes. The fabrication procedure of the YSZ support has been explained in detail elsewhere [24]. Briefly, calcined-milled YSZ (CYSZ) powder was used as the starting material to make the porous support. As received YSZ (Tosoh TZ-8Y, Grove City, OH) was calcined at 1500°C for 3 hr and ball milled for 72 hr. To prepare a CYSZ paste, the calcined powder was well mixed with polymethyl methacrylate ((PMMA), Microbeads<sup>®</sup>, Spheromers CA 6, Norway) as a pore former (the volume ratio of CYSZ to PMMA was 80:20). A laboratory-made ink ( $\alpha$ -terpineol + 5 wt% ethylcellulose) was added to the mixed powder and they were well mixed in a mortar and pestle to leave a homogenous paste. Finally, YSZ coatings (diameter: 10 mm, average thickness: 25  $\mu$ m) were screen printed onto YSZ discs (both sides) and sintered at 1300°C for 3 hr.

To prepare the tungsten carbide infiltrated porous YSZ electrode, ammonium metatungstate (AMT) was used (Informat Advanced Materials, Manchester, CT) as the starting precursor. 3 g of AMT was dissolved in 1 g of distilled water using a regular laboratory ultrasonic cleaner for 10 min giving a clear solution. 0.15 g of Triton (X-45, Union Carbide Chemicals and Plastics Co. Inc., Danbury, CT) was then mixed

into the solution to play a role as a surfactant. While the solution was heated to 100°C in an oil bath, the electrolyte supported discs were preheated to 150°C. The hot solution was then infiltrated into the preheated porous YSZ electrode coatings. After impregnation, the cell was pre-dried in a laboratory vacuum desiccator for 15 min, dried at 150°C for 15 min, and finally heat treated at 350°C for another 15 min. This procedure was repeated (twice on average) until 85 wt% WC (with respect to the YSZ porous support) was embedded into the YSZ network (corresponding to 25 vol.% WC + 75 vol.% YSZ). Note that the WC wt% calculation was done after the WC phase was formed. To synthesize the carbide phase, the infiltrated discs were first heated to 600°C in air. Then, the oxidizing atmosphere was flushed out by Ar. The final heat treatment was done under 80% H<sub>2</sub> – 20% CH<sub>4</sub> atmosphere at 880°C for 12 hr. A heat treated coating was examined by X-ray diffraction (XRD, Rigaku Ultima IV) which confirmed the presence of nano-sized WC phase along with YSZ.

Ceria and nickel electrocatalysts were then incorporated into the WC-based electrode. For CeO<sub>2</sub>, a 0.25M solution of cerium ammonium nitrate (Alfa Aesar) in ethanol was prepared. The WC-YSZ support was infiltrated with the ceria solution using a micro-syringe and subsequently dried at 150°C for 15 min followed by a heat treatment at 350°C for another 15 min. The infiltration-heat treatment cycle was repeated 10 times to obtain 5 wt% ceria. For Ni, 6 g nickel nitrate hexahydrate (Alfa Aesar) was dissolved in 1 g distilled water using a regular ultrasonic cleaner. 0.15 g of Triton was subsequently mixed into the Ni solution and the mixture was heated up to 100°C in an oil bath to produce a highly concentrated solution. The WC-YSZ electrode was then infiltrated with the Ni solution using a micro-syringe. After impregnation, the cell was pre-dried in a laboratory vacuum desiccator

for 15 min, dried at 150°C for 15 min, and finally heat treated at 350°C for another 15 min. The infiltration-heat treatment cycle was repeated twice and the final Ni gain was about 5 wt%. Post-XRD analysis on the anode side confirmed that the carbide phase remains stable upon heat treatment in air at 350°C.

Two types of cells were prepared in this study. Symmetrical cells to study the electrochemical behavior of Ni modified WC-based electrodes as well as carbon deposition under open circuit voltage condition, and fuel cells to study the performance under potentiodynamic and potentiostatic conditions. To prepare the former, the above-mentioned procedure was symmetrically followed on both electrodes. For the fuel cell, however, this process was carried out only for the anode. For the cathode,  $\text{La}_{0.8}\text{Sr}_{0.2}\text{MnO}_3$  (LSM) was chosen to be infiltrated into the porous YSZ support.  $\text{Mn}(\text{NO}_3)_2 \cdot x\text{H}_2\text{O}$ ,  $\text{La}(\text{NO}_3)_3 \cdot 6\text{H}_2\text{O}$  and  $\text{Sr}(\text{NO}_3)_2$  (Alfa Aesar) were used as the starting precursors to prepare a solution based on Pechini's technique [26]. The molar ratio of metal cations, complexing agent (citric acid) and ethylene glycol in the solution was 1:4:4. The thin porous support was repeatedly impregnated by incipient wetness (10 times, on average) on the cathode side until 20 vol.% LSM was embedded into the YSZ network with the LSM phase to be formed in-situ. Post-XRD analysis on the cathode side confirmed the presence of nano-sized LSM phase along with YSZ

### 5.2.2. Cell test

A laboratory made gold paste was used as a current collector (atomised gold powder, Technic Inc., Cranston, Rhode Island) on both electrodes. For the symmetrical cell test, the electrochemical behavior of the cells was studied by ac impedance spectroscopy (Solartron 1255 frequency response analyzer in combination with a Solartron 1287

electrochemical interface) with a four probe configuration. The cells were heated up to 900°C under 80% H<sub>2</sub> – 20% CH<sub>4</sub> mixed atmosphere, held for an hour and cooled down to 800°C. Humidified methane was introduced at 800°C with a constant flow rate of 50 mL/min (a room temperature bubbler was used to humidify the fuels). Impedance measurements were carried out under open circuit condition over a frequency range from 0.1 Hz to 100 kHz with a 10 mV ac perturbation at 800 and 850°C.

For the fuel cell test, the anode side of the cell was sealed onto an alumina tube using a glass seal (Aremco 617). The anode electrode was exposed to humidified 80% H<sub>2</sub> – 20% CH<sub>4</sub> and CH<sub>4</sub> atmospheres with a constant flow rate of 50 mL/min. Note that the fuels used in the entire study were humidified (even when it is not specified) using a room temperature bubbler. Also, extra dry air (H<sub>2</sub>O < 10 ppm) flowed through the cathode electrode at a similar rate. Ac impedance spectroscopy as well as potentiodynamic and potentiostatic analysis were carried out on the fuel cells with a four electrode configuration to study the electrochemical behavior at 800, 850 and 900°C.

### 5.2.3. Cell characterization

Post-XRD analysis was performed to study the present phases after cell tests. Also the microstructure of the electrodes both before and after electrochemical testing was examined on fractured surfaces with a JEOL 6301F field emission scanning electron microscope (FE-SEM).

## 5.3. Results and Discussion

### 5.3.1. Symmetrical study

The ac impedance spectra of a Ni-CeO<sub>2</sub>-WC-YSZ (NCWZ) symmetrical cell at 800°C under both humidified 80% H<sub>2</sub> – 20% CH<sub>4</sub> and CH<sub>4</sub> atmospheres appear in Figure 5.1(a). It is important to note that the impedance data in Figure 5.1 represent half cell polarization. This means that all the data from a symmetrical cell with two NCWZ electrodes and a 300 μm electrolyte were halved and, therefore, it shows the polarization of only one NCWZ electrode and a 150 μm electrolyte. This is indeed the case for all the symmetrical data presented in this study. Prior to the current work, we extensively investigated the electrochemical behavior of WC-based electrodes [24]. For a WC infiltrated porous YSZ electrode, the total electrode polarization (the difference between the high-frequency and low frequency intercepts with the real axis) was 4.0 and 25.2 Ω·cm<sup>2</sup> under the mixed and methane fuels, respectively. As observed here, incorporation of Ni and ceria electrocatalysts into the WC-YSZ anode significantly promotes the activity toward the fuels. Based on the data in Figure 5.1, the total polarization of the promoted cell is 1.45 and 1.85 Ω·cm<sup>2</sup> under the mixed and methane fuels, respectively.

The impedance comprises two semicircles: One arc in the high-medium frequency range (100 kHz – 100 Hz) which is normally attributed to charge transfer resistance corresponding to electron transfer and ion transfer processes occurring at the interfaces [27,28], while the other arc in the low frequency range (100 Hz – 0.1 Hz) is predominantly attributed to non-charge transfer processes including surface reactions and solid state and gas phase diffusion [27,29]. As observed in Figure 5.1(a), under the mixed fuel, the first semicircle is rather large while

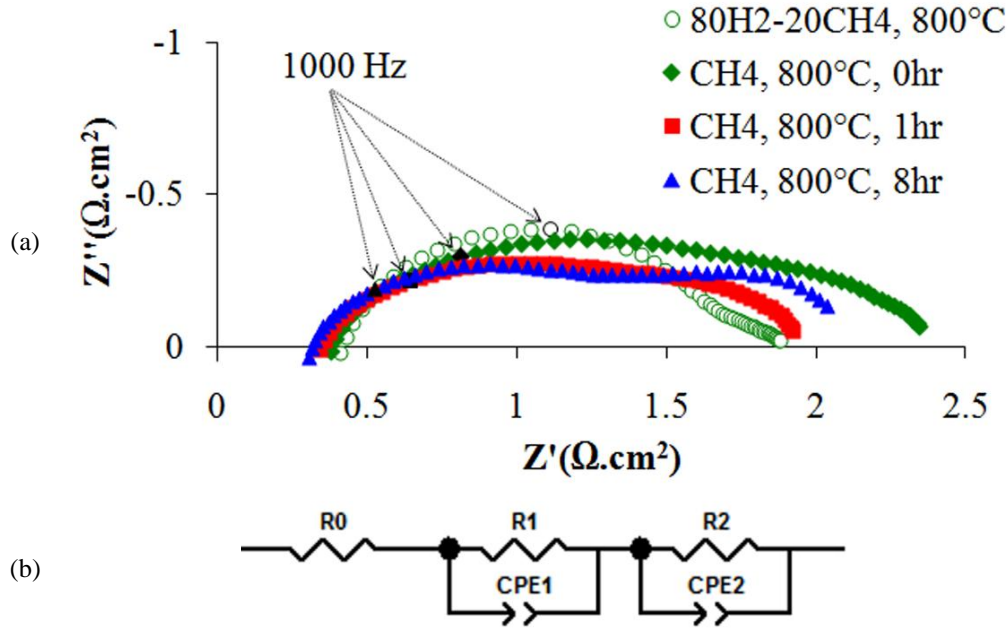


**Fig. 5.1.** (a) Ac impedance spectra of a Ni-CeO<sub>2</sub>-WC-YSZ (NCWZ) symmetrical cell at 800°C under both humidified 80% H<sub>2</sub> – 20% CH<sub>4</sub> and CH<sub>4</sub> atmospheres, (b) an equivalent circuit model.

the second one is small. However, under methane, the arcs are about the same size. An equivalent circuit is also shown in this Figure (5.1(b)) which includes the ohmic resistance corresponding to the YSZ electrolyte (R0), and the non-ohmic polarization corresponding to the composite electrode (R1 and R2). For the sake of comparison, the resistances under mixed and methane fuels are summarized in Table 5.1. It should be mentioned that the polarization data under methane are based on the fit data for the measured impedance.

Based on numerous experiences with Ni-based anode materials in our lab, we were aware that unless the gold current collector is externally pushed against the Ni-based electrode, the attachment between them is poor. Thus, as opposed to our previous observations for WC-YSZ, CeO<sub>2</sub>-WC-YSZ and Ru-CeO<sub>2</sub>-WC-YSZ [24] in which the charge transfer semicircles were dramatically smaller than the non-charge transfer ones, the fact that the high-medium frequency arc was relatively large

**Table 5.1.** Ohmic and non-ohmic polarization of a NCWZ symmetrical cell.

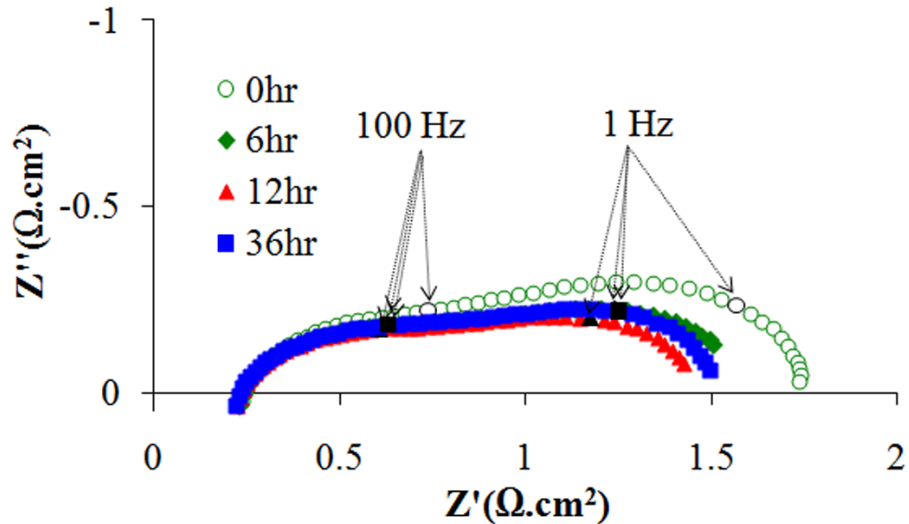
Fuel	R0 ( $\Omega \cdot \text{cm}^2$ )	R1 ( $\Omega \cdot \text{cm}^2$ )	R2 ( $\Omega \cdot \text{cm}^2$ )
80% H <sub>2</sub> – 20% CH <sub>4</sub>	0.42	1.15	0.30
CH <sub>4</sub> , 0 hr	0.38	1.15	0.88
CH <sub>4</sub> , 8 hr	0.31	1.00	0.85

in NCWZ under the mixed hydrogen-rich atmosphere was not surprising. The rather weak attachment between the NCWZ electrode and the gold current collector results in a higher charge transfer polarization at the electrode/current collector interface which affects the high-medium frequency arc. Interestingly, the way the impedance spectrum changes upon the introduction of methane fuel confirms this argument. As soon as the sample is exposed to methane, a large increase in the non-charge transfer polarization occurs while the charge transfer part is almost unchanged (Figure 5.1(a) and Table 5.1). Since a gas diffusion limitation is not expected under OCV conditions [30], such an increase in the low frequency arc (R2 from 0.30  $\Omega \cdot \text{cm}^2$  in hydrogen-rich fuel to 0.88  $\Omega \cdot \text{cm}^2$  in methane fuel) is the inevitable corollary of surface reactions. This makes reasonable sense because methane is rather difficult to activate [31]. While this arc remains rather unchanged with time under methane, a marked improvement in ohmic resistance (R0) as well as charge transfer polarization (R1) is observed. McIntosh et al. [32,33] have already reported similar performance improvement under hydrocarbon fuels and attributed it to formation of conductive carbonaceous films on the porous anode. These deposits not only increase the electrode conductivity, but they also improve the contact resistance between the electrode and current collector and, therefore, decrease the charge transfer polarization. After three hours of exposure to methane under OCV condition, the electrochemical performance became stable and no further change in polarization was observed.

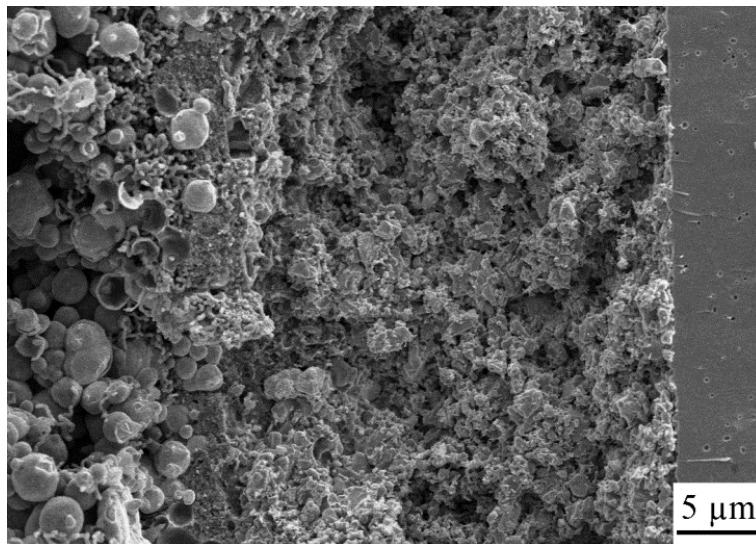
Liu and Barnett [7] have shown that conventional Ni-YSZ supported SOFCs are compatible with humidified methane and carbon deposition is limited during cell operation. They, however, observed that when the cell was maintained under OCV condition, a substantial build-up of carbon on the anode occurred. Their work suggests that carbon deposition on Ni-based anodes is mainly a concern under open circuit condition. Therefore, an impedance study under OCV was considered. Figure 5.2 shows the impedance spectra of a symmetrical NCWZ cell under OCV condition at 850°C under humidified methane. Impedance measurements were made every hour for a period of 48 hr. The result is rather astonishing: no carbon formation is observed under OCV at a temperature as high as 850°C with humidified methane. Except the initial impedance which was slightly larger, the others were about the same. While the charge transfer arc remained identical for all measurements, a very small fluctuation in non-charge transfer polarization was observed. The three spectra (after 6, 12 and 36 hr) illustrated in Figure 5.2 are only examples of measured impedances. Also, after the test, the sample was visually inspected and no coking was observed. Considering the fact that the electrode contained 5 wt% Ni, this result strongly motivated us to investigate how a fuel cell with a NCWZ anode performs under methane.

Figure 5.3 shows an SEM micrograph of the symmetrical cell after being exposed to methane under open circuit condition for a period of 48 hr at 850°C. The dense layer on the right is the YSZ electrolyte, the 30  $\mu\text{m}$  porous layer in the middle is the Ni-CeO<sub>2</sub>-WC-YSZ electrode and the layer on the left which contains large spherical particles is the gold current collector. Several observations should be noted from this figure. First, the electrode layer is quite well attached to the electrolyte and its structural integrity is maintained. Second, the NCWZ electrode

shows a very uniform microstructure and the porous YSZ support is homogeneously covered with infiltrated components (WC, Ni and ceria). Third, the electrode is sufficiently porous after incorporation of 20 vol.% WC, 5 wt% Ni as well as 5 wt% ceria. Finally, no coking is observed throughout the electrode.



**Fig. 5.2.** Ac impedance spectra of the symmetrical NCWZ cell under OCV condition at 850°C under humidified methane.



**Fig. 5.3.** SEM micrograph of the symmetrical NCWZ cell after being exposed to methane under OCV for 48 hr at 850°C.

### 5.3.2. Fuel cell study

The ac impedance spectra of a fuel cell with a Ni-CeO<sub>2</sub>-WC-YSZ anode at 850°C under humidified 80% H<sub>2</sub> – 20% CH<sub>4</sub> mixed atmosphere and humidified methane are illustrated in Figure 5.4. As described previously, the total polarization (the difference between the high frequency and low frequency intercepts with the real axis) of a half cell with the Ni-CeO<sub>2</sub>-WC-YSZ electrode is 1.45 Ω·cm<sup>2</sup> at 850°C for the mixed fuel under OCV. Also, it was shown elsewhere [34] that the total polarization of a half cell with an LSM infiltrated porous YSZ electrode is <0.1 Ω·cm<sup>2</sup> under air at the same condition. Thus, we reasonably expect that under open circuit condition, the total polarization of a cell with a Ni-CeO<sub>2</sub>-WC-YSZ anode and an LSM infiltrated porous YSZ cathode to be about 1.55 Ω·cm<sup>2</sup>. The measured total polarization is 1.5 Ω·cm<sup>2</sup> which is in a good agreement with the earlier results. Note that the cathodic contribution to the total polarization is quite small.

As observed in Figure 5.4, with both mixed and methane fuels, the impedance comprises three semicircles: one in the high frequency range, one in the medium frequency range and the last arc in the low frequency range. Interestingly, when the hydrogen-rich fuel was replaced with methane, the first two semicircles remained unchanged while a slight increase occurred in the low frequency lobe. Thus, similar to the NCWZ half cell, what actually controls the low frequency polarization is the anodic surface reactions. In addition, from the data in Figure 5.4, the ohmic resistance of the cell is 0.97 Ω·cm<sup>2</sup> under the mixed fuel and 0.94 Ω·cm<sup>2</sup> under methane. Similar to the NCWZ half cell, such a decrease in the ohmic resistance has to do with the formation of conductive carbonaceous films on the porous anode.

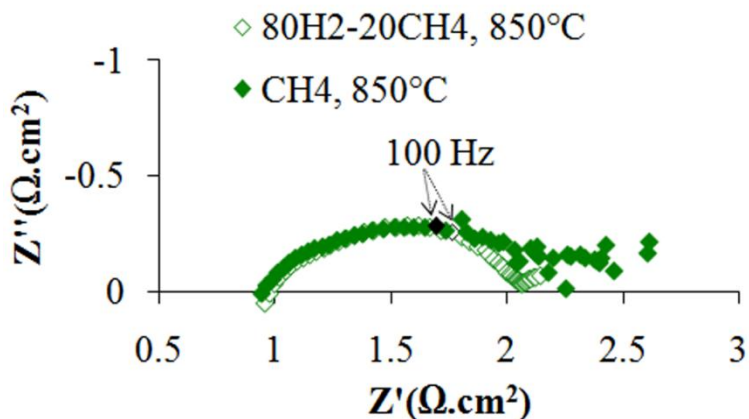


**Fig. 5.4.** Ac impedance spectra of a cell with a Ni-CeO<sub>2</sub>-WC-YSZ anode at 850°C under humidified 80% H<sub>2</sub> – 20% CH<sub>4</sub> atmosphere and humidified methane.

The V-i characteristics and power densities at 850 and 900°C under the two fuels are shown in Figure 5.5. Open circuit voltages decrease with increasing temperature. For example, under methane, the OCV is 1.00 and 0.97 V at 850 and 900°C, respectively. While the cell performance is higher with the humidified 80% H<sub>2</sub> – 20% CH<sub>4</sub> atmosphere at both temperatures, the performance under humidified methane is reasonably close (only about 15% lower). This is not surprising because, as observed in Figure 5.4, surface reaction polarization was only slightly larger under methane fuel. Table 5.2 compares the maximum power densities of this cell with a Ni-CeO<sub>2</sub>-WC-YSZ anode and an earlier cell with a Ru-CeO<sub>2</sub>-WC-YSZ anode (RCWZ, 1 wt% Ru and 5 wt% ceria) with a similar electrolyte and cathode [24]. Interestingly, performance of the cell with the Ni modified anode is markedly higher under methane (e.g. 131 mW · cm<sup>-2</sup> versus 83 mW · cm<sup>-2</sup> at 900°C).

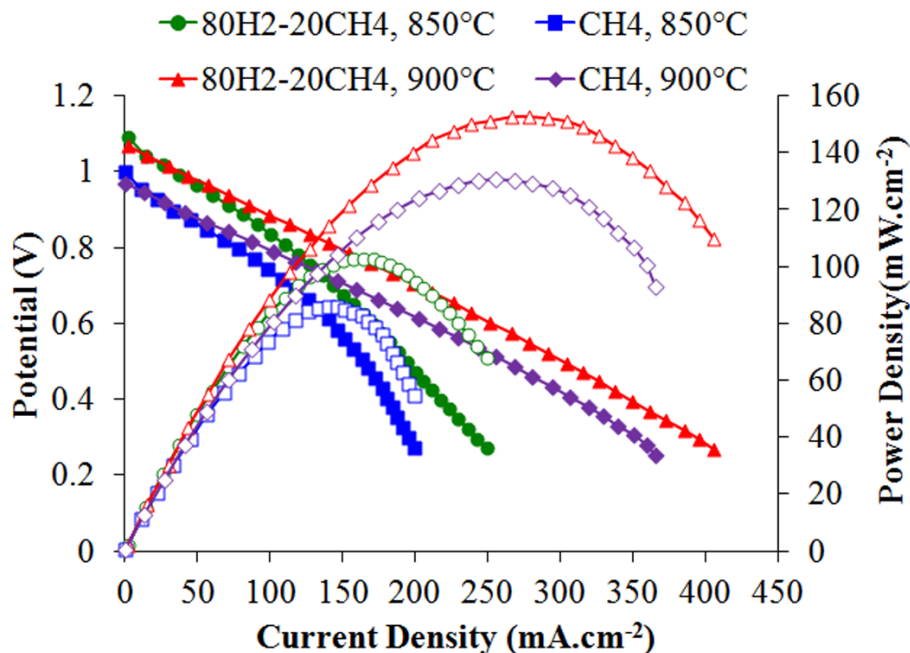


**Fig. 5.5.** V-i characteristics and power densities of the cell with a Ni-CeO<sub>2</sub>-WC-YSZ anode at 850 and 900°C under the two fuels.

**Table 5.2.** Power densities of cells with Ni-CeO<sub>2</sub>-WC-YSZ (NCWZ) and Ru-CeO<sub>2</sub>-WC-YSZ (RCWZ) [24] anodes.

Temperature (°C)	P (mW.cm <sup>-2</sup> ), NCWZ		P (mW.cm <sup>-2</sup> ), RCWZ	
	80-20 mix	CH <sub>4</sub>	80-20 mix	CH <sub>4</sub>
850	103	86	185	58
900	153	131	263	83

An SEM micrograph of a Ni-CeO<sub>2</sub>-WC-YSZ anode is illustrated in Figure 5.6. The lower magnification image shows that the porous YSZ support is uniformly covered with a connected network of the carbide phase. EDS analysis was done over numerous points throughout the anode in order to differentiate among the infiltrated phases. This was, however, quite challenging because of resolution limitations of the chemical analysis at high magnifications. Since Ni and ceria were incorporated after the carbide phase was formed, the nano-size particles dispersed throughout the WC-YSZ network are Ni or ceria.

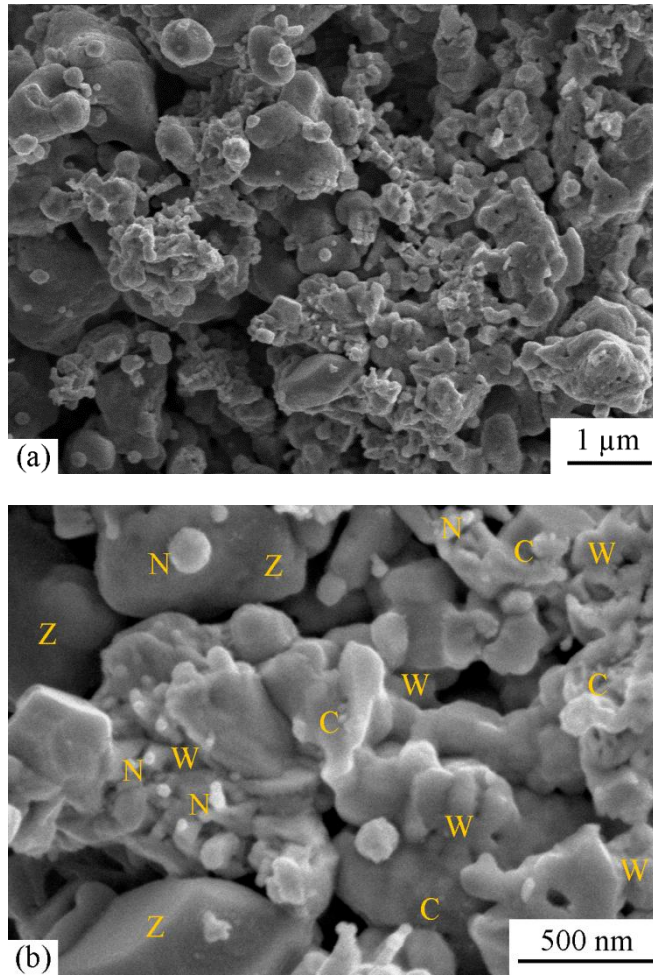


**Fig. 5.6.** SEM micrographs of the Ni-CeO<sub>2</sub>-WC-YSZ anode (N: Ni, C: CeO<sub>2</sub>, W: WC, and Z: YSZ).

Note that ceria particles are the smallest features in the range of 10-20 nm and Ni particles are those brighter ones in the range of 50-100 nm.

### 5.3.3. Stability issue

Figure 5.7 shows how stable the cell with a Ni modified anode is under humidified methane. The stability test was done under a constant voltage of 0.7 V at 850°C for a period of 24 hr. A marked decrease in power density (about 35 %) was observed in the first 15 min of the experiment. As discussed elsewhere [24], surface oxidation of the carbide phase is one of the two possible mechanisms of the fuel

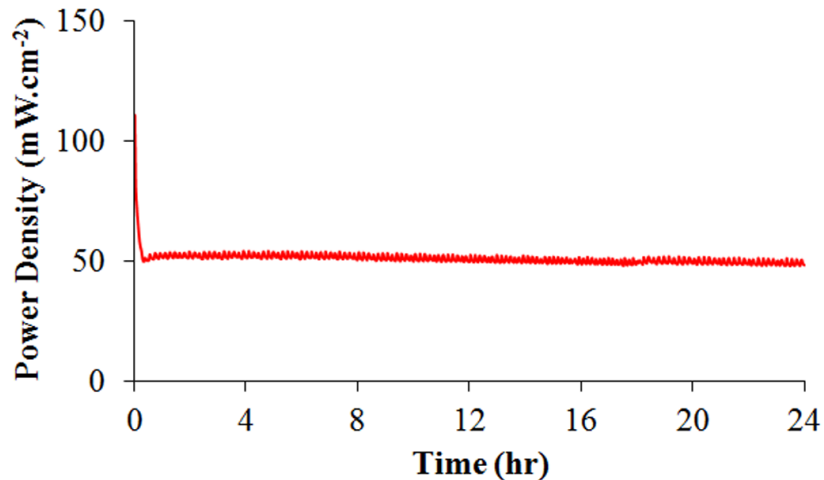


**Fig. 5.7.** Performance of the cell toward humidified methane, under a constant voltage of 0.7 V at 850°C for 24 hr.

oxidation process. Before polarization, the fresh surface layer of WC nano-particles is very active toward the fuel which is why the performance is relatively high at the very beginning. Several minutes after polarization, however, the carbide surface gradually approaches an equilibrium oxidation state and the performance stabilizes. It is quite remarkable that no degradation was observed during the course of this experiment, neither because of instability of the carbide phase nor due to carbon formation on the Ni modified WC-based anode. When WC-based materials are considered as alternative anodes, the stability of the carbide phase is one of the major concerns. As reported elsewhere [24], in a polarized cell with a WC-YSZ anode under methane fuel, a major phase change from WC to W occurs which is unavoidably governed by kinetic reasons. However, we showed that when the WC-YSZ anode is modified by Ru-ceria, the carbide phase is preserved to a great extent. Figure 5.8 shows the XRD spectrum of a NCWZ anode tested for more than a week. As observed, the carbide phase remains stable, no tungsten metal is detected and only a very minor tungsten oxide phase appears. Our previous work on WC-based anodes [24] suggests that surface oxidation of the carbide phase is

actually one of the possible mechanisms of the fuel oxidation process and as long as the rate of carbide oxidation and that of oxide recarburization remain about the same, the cell performance is stable. The rather stable performance of the Ni modified carbide based anode, thus, supports the previous argument. Figure 5.9 shows the OCV impedance spectra of the cell before and after the stability test at 850°C under methane. Intriguingly, the cell polarization remained rather unchanged. This further confirms the stable performance of the anode with no carbon deposition under methane.

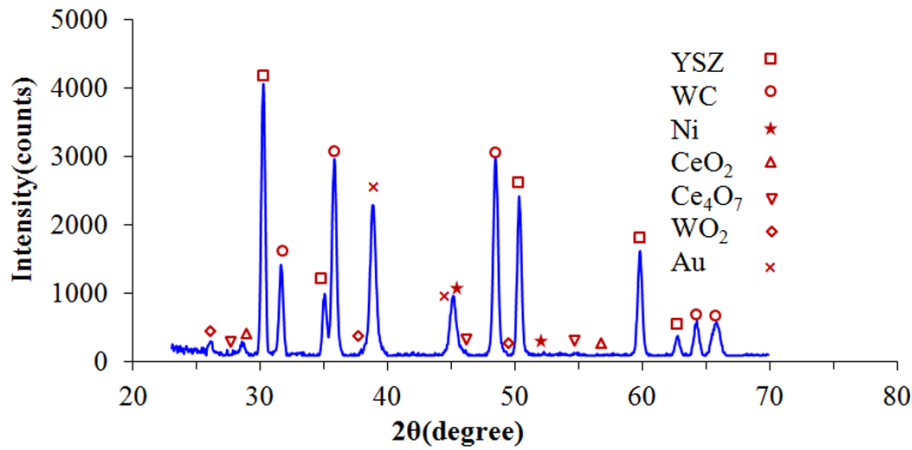


**Fig. 5.8.** XRD spectrum of a NCWZ anode tested for more than a week.

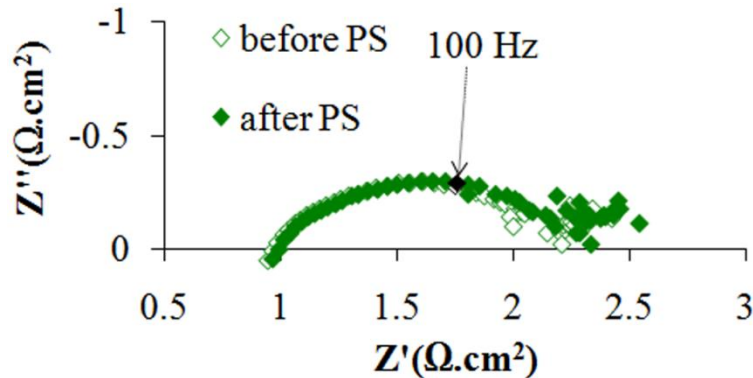


**Fig. 5.9.** OCV impedance spectra of the cell before and after the stability test at 850°C under methane.

In our previous work [24,25] we have proposed a series of electrochemical reactions which possibly occur over a carbide-based anode. Briefly, these reactions include:



As Claridge et al. [35] pointed out, methane conversion over a carbide catalyst can be explained by two different pathways: a redox mechanism (equation 5.5) in which an adsorbed oxygen atom ( $\text{O}^*$ , equation 5.1) reacts with a carbon atom from the carbide surface and a noble metal mechanism (equation 5.6) in which the oxygen atom reacts with an adsorbed carbon atom ( $\text{C}^*$ , equation 5.2). The former results in carbon vacancies in the carbide phase which are to be filled with either carbon or oxygen (equations 5.7 and 5.8). Carbon atoms from WC, however, do not play a role in the noble metal mechanism and remain intact. In practice, both of these mechanisms decisively participate in the overall reaction [35].

The stability challenge in WC-based anodes particularly under methane fuel has already been discussed [24]. Also, the problem with carbon formation in Ni-based anodes is well appreciated [1]. Surprisingly, an anode based on WC and Ni not only performs stably with no undesirable phase transformation, but also does not promote

the buildup of carbon at temperatures as high as 850°C. Nickel is a well known catalyst for the formation of carbon fibers [4]. Carbon deposition on a Ni surface is the fundamental step in carbon fiber formation. The deposited carbon is then dissolved from the surface into the bulk of the Ni catalyst and finally precipitates as carbon fibers. Gross et al. [4] further argued that what makes the Ni-based anodes incompatible with hydrocarbon fuels is in fact not carbon deposition itself, but the bulk dissolution followed by fiber precipitation. Furthermore, as discussed by Mogensen and Kammer [36], direct electrochemical oxidation of methane is normally unfavourable in nickel-based anodes; instead, methane predominantly cracks over the Ni catalyst and the cracking products contribute toward electrochemical performance.

As for the Ni modified WC-based anode, a plausible scenario could be as follows: On the one hand, carbon deposition occurs on Ni surface as expected with methane fuel at temperatures as high as 850°. On the WC surface, on the other hand, carbon vacancies are formed as the inevitable result of the redox mechanism. Since nickel is supported by the tungsten carbide network (Figure 5.6), it donates the surface carbon to the carbide with carbon shortage (equation 5.7). This is a win-win exchange: the Ni surface becomes carbon-free and can continue to play a role as an electrocatalyst while WC remains stable and can contribute to methane oxidation. The solid state reaction between transition metals such as W and Mo and an in-situ source of carbon to form carbides is not new [37,38]. For example, Zhu and Manthiram [37] showed that a polymer precursor can be used as an in-situ source of carbon instead of gas phase carburization to synthesize tungsten carbide. These works reasonably support our above mentioned scenario.

In order to ensure that WC plays a critical role in the removal of deposited carbon, behavior of an anode based solely on Ni-WC-YSZ under humidified 80% H<sub>2</sub> – 20% CH<sub>4</sub> and humidified methane fuels at 850°C was also studied. As expected, a rather large performance decrease was observed. For example, the total cell polarization under open circuit condition was 5.8 Ω·cm<sup>2</sup> for a cell with a Ni-WC-YSZ anode as opposed to 1.3 Ω·cm<sup>2</sup> for a cell with a Ni-CeO<sub>2</sub>-WC-YSZ anode, under the humidified 80% H<sub>2</sub> – 20% CH<sub>4</sub> fuel. However, quite similar to the Ni-CeO<sub>2</sub>-WC-YSZ, the anode without ceria showed a steady performance and no carbon formation was observed. Figure 5.10 demonstrates an SEM micrograph of the Ni-WC-YSZ anode operated on humidified 80% H<sub>2</sub> – 20% CH<sub>4</sub> and humidified methane fuels for 72 hr. As the image indicates, no carbon fiber is observed and the Ni particles (dispersed spherical spots which look slightly brighter) are well attached to the WC-YSZ support. In addition, phase analysis (XRD) of this anode confirmed that the WC remained chemically stable.

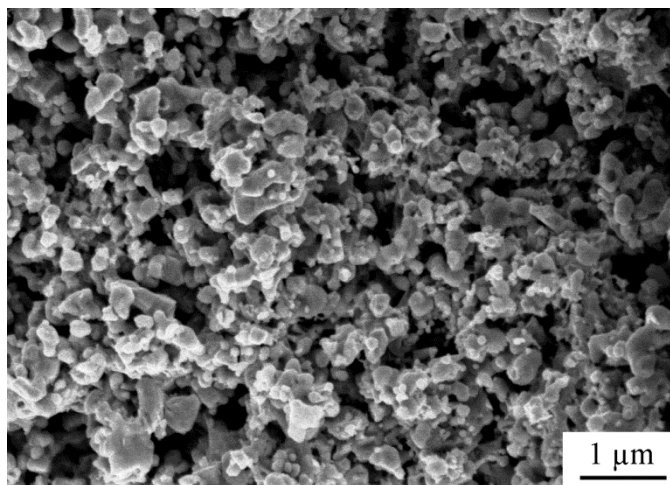


**Fig. 5.10.** An SEM micrograph of the Ni-WC-YSZ anode operated on humidified 80% H<sub>2</sub> – 20% CH<sub>4</sub> and humidified methane fuels.

Note that the possible role of ceria in suppression of carbon formation is not being overlooked. Ceria is known to be an oxygen donor in reducing atmospheres and it essentially contributes to electrochemical oxidation of the carbon [36]. Nonetheless, it was shown [25] that an anode based on CeO<sub>2</sub>-WC-YSZ suffers from chemical instability. More importantly, the facts that WC is preserved and no carbon fiber formed in anodes with and without ceria indicate that the carbide phase actively participates in removal of the deposited carbon. It should be emphasized that since the idea of an alternative anode based on WC and Ni is novel, more investigation is required to fully understand the mechanism which results in such a dual role: to suppress carbon deposition and to stabilize the carbide phase.

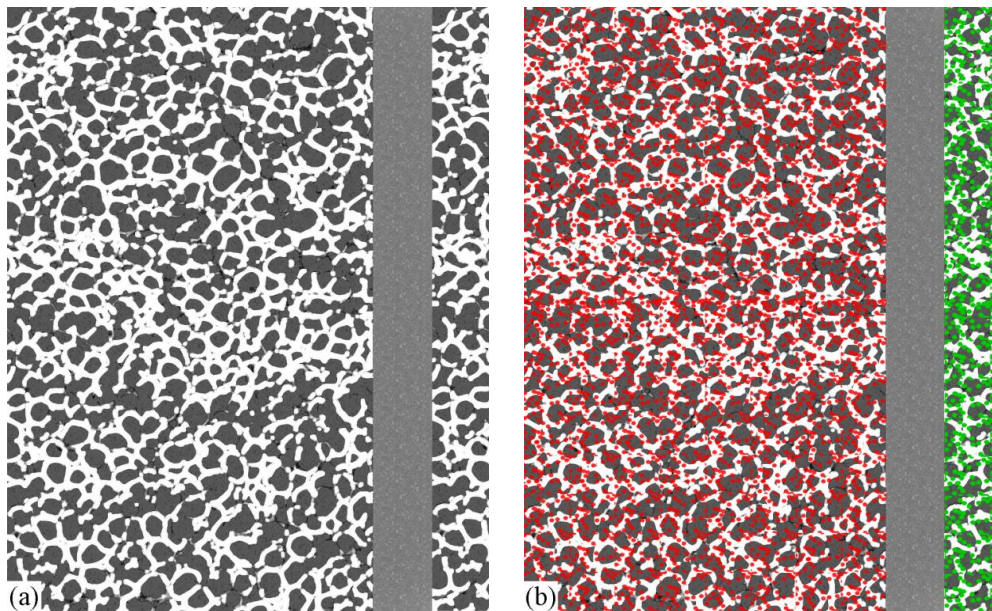
#### 5.3.4. Redox issue

One of the more significant challenges of Ni-based anodes (the state-of-the-art anode materials for SOFCs) is their poor mechanical stability during reduction/oxidation cycles. While the anode normally performs under reducing conditions, it may experience several reduction/oxidation (redox) cycles during its lifetime because of accidental occurrences such as failure in the fuel supply, a broken seal and substantial fuel utilization [39]. When a cell goes through a redox cycle, the Ni-based anode experiences a significant volume change which causes a great deal of mechanical stress on this electrode. This is a serious threat to the cell integrity particularly when the cell is mechanically supported by the anode and may result in catastrophic failure of the cell.

Similar to cells based on a Ni-YSZ anode, redox cycling could be a serious concern in SOFCs with WC-based anode materials. Upon oxidation, tungsten carbide experiences a large volume change

(theoretical density of WC and  $\text{WO}_3$  are 15.8 and 7.2  $\text{g}\cdot\text{cm}^{-3}$ , respectively) which imposes a significant mechanical stress on the anode. In a conventional composite WC-YSZ anode in which the carbide is actually a structural component of the electrode, this internal stress could devastate the structural integrity. Thus, in order for the WC-based anode to be a viable alternative, this issue needs to be addressed.

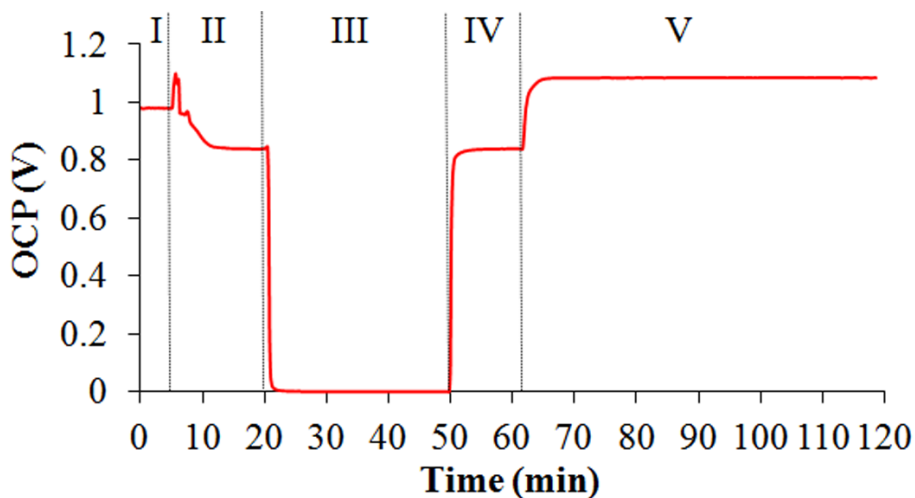
Recently, highly redox resistance tubular SOFCs with a Ni-YSZ anode were successfully developed [40]. In the current work, we used the same approach to address the redox issue. Figure 5.11 schematically shows the concept which lies behind this design. First, a robust YSZ-based cell which includes a thick (hundreds of microns) porous YSZ support, a thin (tens of microns) gas-tight YSZ electrolyte and a thin (tens of microns) porous YSZ is fabricated (Figure 5.11 (a)). The anode and cathode of choice are then incorporated into the thick and thin



**Fig. 5.11.** Schematic drawing of the cell configuration, (a) before and (b) after infiltration.

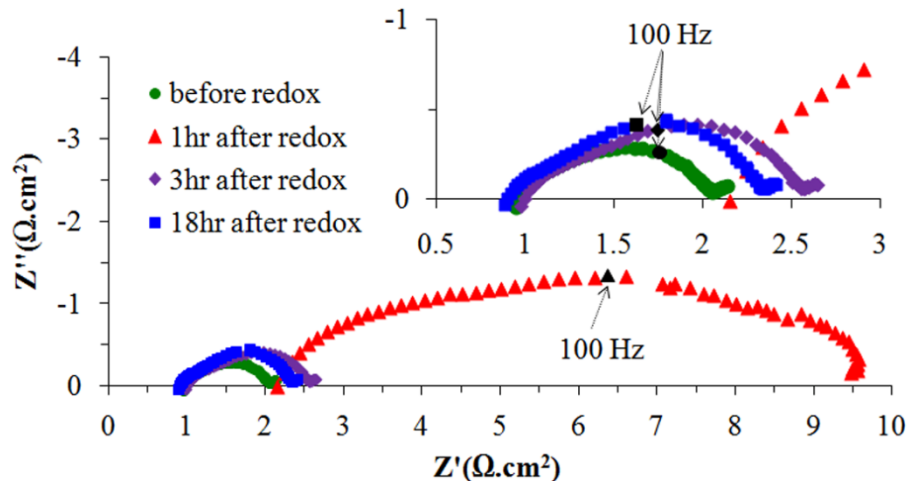
porous YSZ layers, respectively, by a post infiltration process (Figure 5.11 (b)). The major advantage of this design over the conventional one is that the infiltrated material does not contribute to the structural integrity of the cell. Additionally, while a conventional cell typically needs 50 wt% of the electronically conductive component to reach the percolation threshold, the required amount is significantly less in infiltrated cells [24], which also contributes to redox resistance.

Figure 5.12 illustrates how the open circuit potential changes during an oxidation-reduction cycle at 850°C. At the very beginning, the cell is under humidified methane and the OCP remains at 0.98 V (part I). Methane is then flushed out by a neutral gas, Ar, for a period of 15 min when the OCP drops to 0.84 V (part II). When air is introduced, the OCP drops to zero within a minute (part III). Once the anode is oxidized, the air is removed by Ar and the OCP quickly jumps back to 0.82 V (part IV). Finally, humidified hydrogen is introduced and only a few minutes are enough for the OCP to remain stable at 1.08 V.



**Fig. 5.12.** OCV change of the cell during an oxidation-reduction cycle.

After a cell goes through an oxidation-reduction cycle, the anode contains no carbide phase. Thus, the anode was treated under the 80%  $H_2 - 20\% CH_4$  atmosphere at  $850^\circ C$  for a period of 18 hours. Figure 5.13 shows how the impedance of the cell behaves during the course of recarburization. This figure contains very informative data and several observations should be pointed out. First, and perhaps the most important is that the structural integrity of the cell is maintained and no delamination occurs. Secondly, at  $850^\circ C$  under 80%  $H_2 - 20\% CH_4$  atmosphere, it takes three hours for the anode to revive. The impedance spectrum after the first hour shows that the ohmic resistance of the cell is more than twice that of the original cell with a WC-based anode ( $2.15 \Omega \cdot cm^2$  vs.  $0.97 \Omega \cdot cm^2$ ). The total polarization of the cell at this stage is also relatively high ( $7.35 \Omega \cdot cm^2$  as opposed to  $1.5 \Omega \cdot cm^2$ ). After three hours, however, the ohmic resistance and total polarization of the cell are  $0.99$  and  $1.7 \Omega \cdot cm^2$ , respectively, which are reasonably close to those before the redox cycle. Finally, while the cell shows a lower ohmic resistivity after recarburization (the total ohmic resistance of the cell is  $0.9 \Omega \cdot cm^2$ ), the total polarization is slightly



**Fig. 5.13.** OCV impedance behavior of the cell during recarburization after the oxidation-reduction cycle.

higher. This slight change is essentially the inevitable corollary of microstructural alteration due to the oxidation-reduction-re carburization process.

The V-i characterization of the cell during the recarburization process is demonstrated in Figure 5.14. As observed, the result is rather consistent with how the impedance evolves. At the beginning, when the ohmic resistance is rather high and the total polarization is relatively large, the cell performs rather poorly and the maximum power density is only  $40.7 \text{ mW cm}^{-2}$  (originally  $102.8 \text{ mW cm}^{-2}$ ). However, after three hours, when the ohmic resistance of the cell becomes close to that of the original cell, it performs similarly. Interestingly, a remarkable improvement in cell performance occurs upon continuation of the recarburization process. After 18 hr of recarburization, the final power density is  $152.8 \text{ mW cm}^{-2}$ , which is a 48.6% increase compared to that of the original cell.

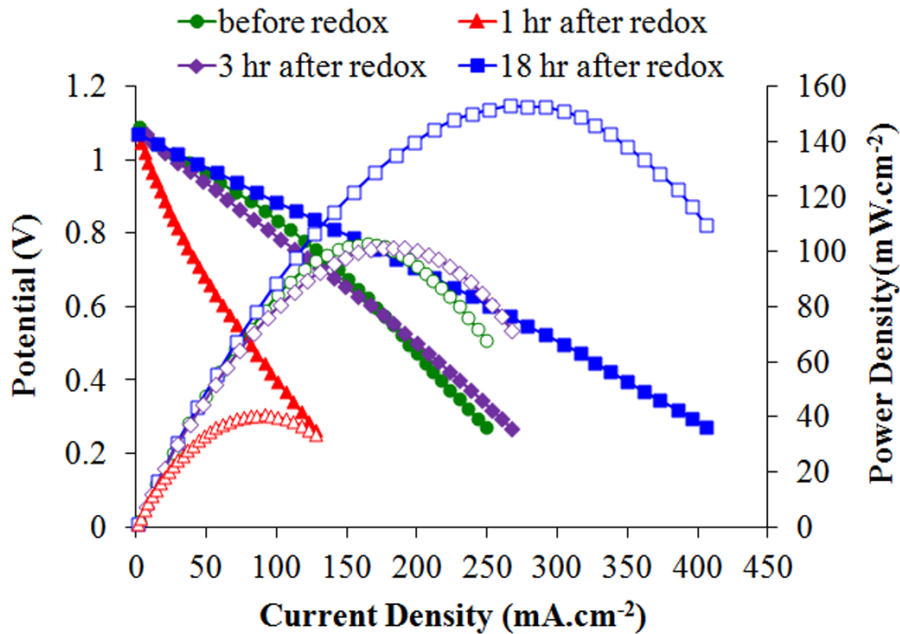


**Fig. 5.14.** V-i behavior of the cell during the recarburization process.

After recarburization, stability of the cell performance was also studied at 850°C with humidified 80% H<sub>2</sub> – 20% CH<sub>4</sub> and methane fuels. The cell was polarized at 0.7 V for a period of 24 hr under each fuel. Similar to the original cell, very stable behavior was observed in both cases. Figure 5.15 shows the OCP impedance spectra of the recarburized cell before and after a 24 hour potentiostatic test at 850°C under the mixed fuel. Since the cell was kept polarized at 0.7 V for the duration of the test, an impedance spectrum of the polarized cell is also included in this figure. While the ohmic resistance of the cell remains unchanged, a minor decrease in the total polarization is observed. Note that only the low frequency region of the impedance plot is slightly changed. The stable behavior of the polarized cell after the oxidation-reduction-recarburization cycle also suggests that the structural integrity of the cell remained intact. It is noteworthy that the post-analysis XRD test on this anode confirmed that the carbide phase was completely revived and neither tungsten metal nor oxide was observed (the XRD pattern was very similar to Figure 5.8 and, therefore, is not shown here).

An SEM micrograph of the interface between the Ni-CeO<sub>2</sub>-WC-YSZ anode and YSZ electrolyte after an oxidation-reduction-recarburization cycle is shown Figure 5.16. As suggested by the electrochemical analysis, the image also confirms that the structural integrity of the cell was maintained and no delamination and/or micro-cracks are observed along the interface. Furthermore, the porous YSZ support is uniformly and intimately covered with the infiltrated components (WC, Ni and ceria). Lastly, no carbon fiber formation is observed throughout the electrode.

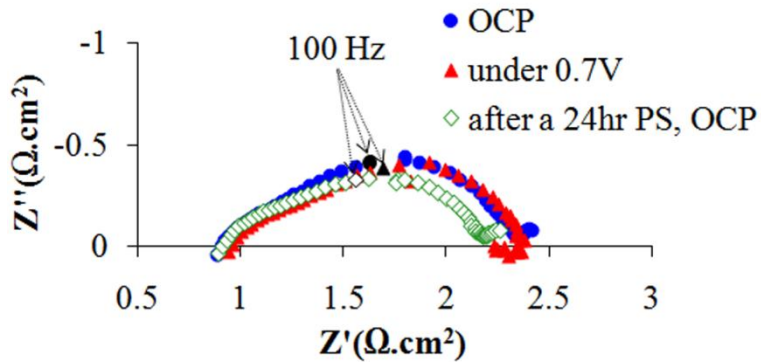


**Fig. 5.15.** OCV impedance spectra of the recarburized cell before and after a 24 hour potentiostatic test at 850°C under the mixed fuel.

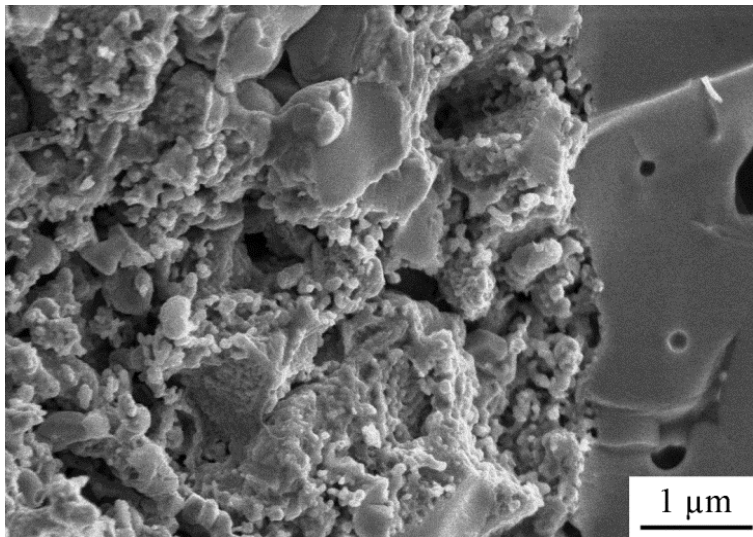


**Fig. 5.16.** SEM micrograph of an interface between the Ni-CeO<sub>2</sub>-WC-YSZ anode and YSZ electrolyte after the oxidation-reduction-recarburization cycle.

### 5.3.5. WC as an anode material

Our interest in investigating WC as a potential candidate was based on several intriguing attributes of this material including catalytic resemblance between WC and precious metals, tolerance against carbon formation, very high electronic conductivity ( $0.52 \times 10^5 \text{ S cm}^{-1}$  for

WC vs.  $1.43 \times 10^5 \text{ S} \cdot \text{cm}^{-1}$  for Ni [25]) and very high melting point ( $2870^\circ\text{C}$ ) as a reasonable guarantee of microstructural stability. Nevertheless, previous work [24] revealed that there are two major challenges in regard to WC-based anodes: their activity towards methane fuel is relatively poor and needs to be improved, and they may experience chemical instability under cell operating conditions.

Therefore, the idea of using Ni to modify the WC-based anode was not only to improve but also to stabilize the performance. As discussed above, the redox mechanism is one of the active pathways of methane oxidation on a WC surface which involves surface carbon atoms from the carbide phase (equation 5.5). As long as the rate of carbide oxidation and that of metal and/or oxide recarburization remain about the same, the cell performance will be stable. In a conventional WC-YSZ electrode with methane fuel, under cell operation conditions the recarburization reaction is kinetically less favourable and the carbide phase is unstable. Under such circumstances, carbon formation is in fact advantageous: an in-situ source of carbon is supplied to preserve the carbide from being depleted of carbon. Thus, when a WC-based anode is modified with Ni, not only can the attributes of nickel be taken advantage of, but its tendency toward catalyzing the build-up of carbon could be beneficial. This is actually a win-win situation: on the one hand stability of the carbide phase and on the other hand no destructive carbon formation.

The cell design and fabrication process proposed here can reasonably address other challenges posed by the high processing temperature and low coefficient of thermal expansion (CTE) of WC as well as its significant volume change during redox cycling. Firstly, the carbide can be incorporated into the porous YSZ support with a very simple and practical infiltration technique followed by a low temperature heat

treatment. In addition, since a nano-sized carbide network is formed within the YSZ support, the amount of carbide to meet the electronic conductivity requirement is significantly less than what it is in a conventional WC-YSZ composite. The less WC incorporated into the anode, the less problematic is the CTE mismatch and redox cycling. Finally, since WC does not play any structural role whatsoever, the structural integrity of the cell can be maintained during redox cycling and a catastrophic failure can be avoided.

At last, as far as the cell performance goes, there is definitely room for improvement: the electrode support configuration should be considered, the microstructure of incorporated WC needs to be improved, and the amount of the infiltrated components must be optimized.

#### **5.4. Conclusions**

This study shows that modifying a WC-based anode by Ni electrocatalyst can successfully address the stability challenge posed by tungsten carbide and the carbon formation challenge posed by Ni. Exposed to humidified (3% H<sub>2</sub>O) methane for a course of 48 hr at 850°C, the Ni modified WC-based anode performs stably under open circuit condition and no carbon formation is observed. The cell also maintains its steady performance under polarized condition during which the carbide phase remains stable and does not experience any catastrophic phase change. Lastly, the proposed configuration highly reinforces the cell so that it successfully withstands oxidation-reduction-re carburization cycles and structural integrity is maintained.

## References

- [1] S. McIntosh, R. J. Gorte, *Chem. Rev.* 104 (2004) 4845.
- [2] M. L. Toebes, J. H. Bitter, A. J. van Dillen, K. P. de Jong, *Catal. Today* 76 (2002) 33.
- [3] C.M. Finnerty, N.J. Coe, R.H. Cunningham, R. M. Ormerod, *Catal. Today* 46 (1998) 137.
- [4] M. D. Gross, J. M. Vohs, R. J. Gorte, *J. Mater. Chem.* 17 (2007) 3071.
- [5] C. Sun, U. Stimming, *J. Power Sources* 171 (2007) 247.
- [6] J. B. Goodenough, Y. H. Huang, *J. Power Sources* 173 (2007) 1.
- [7] J. Liu, S. A. Barnett, *Solid State Ionics* 158 (2003) 11.
- [8] H. Kim, C. Lu, W. L. Worrell, J. M. Vohs, R. J. Gorte, *J. Electrochem. Soc.* 149 (2002) A247.
- [9] E. Nikolla, J. Schwank, S. Linic, *J Electrochem. Soc.* 156 (2009) B1312.
- [10] H. Kan, H. Lee, *Appl. Catal. B* 97 (2010) 108.
- [11] W. Wang, S. P. Jiang, A. I. Y. Tok, L. Luo, *J. Power Sources* 159 (2006) 68.
- [12] S.P. Jiang, S.H. Chan, *J. Mat. Sci.* 39 (2004) 4405.
- [13] S.W. Tao, J.T.S. Irvine, *Chem. Rec.* 4 (2004) 83.
- [14] J. W. Fergus, *Solid State Ionics* 177 (2006) 1529.
- [15] Z. Cheng, J. H. Wang, Y. M. Choi, L. Yang, M. C. Lin, M. Liu, *Energy Environ. Sci.* 4 (2011) 4380.
- [16] A. Atkinson, S. Barnett, R. J. Gorte, J. T. S. Irvine, A. J. McEvoy, M. Mogensen, S. C. Singhal, J. M. Vohs, *Nat. Mater.* 3 (2004) 17.
- [17] R. J. Gorte, J. M. Vohs, *Annu. Rev. Chem. Biomol. Eng.*, 2 (2011) 9.
- [18] H. H. Hwu, J. G. Chen, *Chem. Rev.* 105 (2005) 185.

- [19] A. R. S. Darujati, D. C. LaMont, W. J. Thomson, *Appl. Catal. A* 253 (2003) 397.
- [20] J. Sehested, C. J. H. Jacobsen, S. Rokni, J. R. Rostrup-Nielsen, *J. Catal.* 201 (2001) 206.
- [21] Y. Hara, N. Minami, H. Itagaki, *Appl. Catal. A* 323 (2007) 86.
- [22] D. J. Ham, Y. K. Kim, S. H. Han, J. S. Lee, *Catal. Today* 132 (2008) 117.
- [23] R. Ganesan, D. J. Ham, J. S. Lee, *Electrochem. Comm.* 9 (2007) 2576.
- [24] A. Torabi, T. H. Etsell, *J. Power Sources*, submitted (2012).
- [25] A. Torabi, T. H. Etsell, N. Semagina, Partha Sarkar, *Electrochim. Acta* 67 (2012) 172.
- [26] M. P. Pechini, U.S. Patent No. 3,330,697 (1967).
- [27] S. B. Adler, *Solid State Ionics* 111 (1998) 125.
- [28] T. L. Reitz, H. Xiao, *J. Power Sources* 161 (2006) 437.
- [29] Q. A. Huang, R. Hui, B. Wang, J. Zhang, *Electrochim. Acta* 52 (2007) 8144.
- [30] S. Park, R. Craciun, J.M. Vohs, R.J. Gorte, *J Electrochem. Soc.* 146 (1999) 3603.
- [31] M. D. Gross, J. M. Vohs, R. J. Gorte, *J. Electrochem. Soc.* 154 (2007) B694.
- [32] S. McIntosh, H. He, S. I. Lee, O. Costa-Nunes, V. V. Krishnan, J. M. Vohs, R. J. Gorte, *J. Electrochem. Soc.* 151 (2004) A604.
- [33] S. McIntosh, J. M. Vohs, R. J. Gorte, *J. Electrochem. Soc.* 150 (2003) A470.
- [34] A. Torabi, A. R. Hanifi, T. H. Etsell, P. Sarkar, *J. Electrochem. Soc.* 159 (2012) B201.
- [35] J. B. Claridge, A. P. E. York, A. J. Brungs, C. Marquez-Alvarez, J. Sloan, S. C. Tsang, M. L. H. Green, *J. Catal.* 180 (1998) 85.
- [36] M. Mogensen, K. Kammer, *Annu. Rev. Mater. Res.* 33 (2003) 321.

- [37] Y. T. Zhu, A. Manthiram, *J. Am. Ceram. Soc.* 77 (1994) 2777
- [38] A. M. Stux, C. Laberty-Robert, K. E. Swider-Lyons, *J. Solid State Chem.* 181 (2008) 2741
- [39] Q. X. Fu, F. Tietz, *Fuel Cells* 8 (2008) 283.
- [40] A. R. Hanifi, A. Torabi, M. Zazulak, T. H. Etsell, L. Yamarte, P. Sarkar, M. C. Tucker, *Electrochem. Soc. Trans.* 35 (2011) 409.

## Chapter 6

### Concluding Remarks

Considering the incompatibility of state-of-the-art anodes based on Ni-YSZ with hydrocarbon fuels, developing alternative anodes which can be operated on fuels other than hydrogen is crucial. The anode electrode in a solid oxide fuel cell essentially operates in very demanding conditions. Catalytic activity toward the fuel, electronic conductivity, chemical stability with respect to not only the fuel but also the oxidation products, microstructural durability, compatibility with other cell compartments, processability, and structural integrity are among the major requirements that an anode has to meet. Therefore, developing competent alternative materials that are able to operate stably with a viable performance throughout a commercially reasonable lifetime is quite challenging. This study has been focused on tungsten carbide-based materials as potential candidate anodes for direct utilization of methane fuel in solid oxide fuel cells. Instead of an all-or-nothing approach, this work has tried not only to highlight the capabilities of WC-based materials, but also to appreciate the challenges.

To decrease the high processing temperature posed by the very high melting point of WC, to develop a nano-sized inter-connected electrocatalyst network, and to maintain the structural integrity of the cells, a porous YSZ support with an engineered microstructure was developed. It was shown that the morphology of the porous YSZ network greatly affects the surface area of the support, the density of the three phase boundary and, thus, the electrochemical performance of the cells. A very uniform microstructure was developed based on calcined and milled YSZ in which the pore network was well connected and the submicron calcined-based cavities guaranteed a homogenous distribution of the nano-sized electrocatalyst network. Specific surface area of the porous support and configuration of the electrocatalyst nanoparticles were found to give significant insights about the three phase boundaries and the relative electrochemical performance of the cells.

Chemical stability with respect to the fuel is a primary requirement to be satisfied with anode materials. Experimental measurements and thermodynamic calculations indicated that WC-based electrodes were not stable in hydrogen fuels under open circuit condition due to the sluggish reaction between the carbide phase and the atmosphere. These electrodes, however, remained stable with mixed hydrogen-methane and methane fuels under open circuit potential. Impedance studies revealed that the ohmic polarization of conventional WC-YSZ composites was very low. The relatively large reaction polarization, on the other hand, was a major performance bottleneck for the WC-YSZ anodes indicating that a WC catalyst cannot activate methane with a reasonable reaction rate. In addition to the rather poor performance under methane, WC experienced a major phase change under polarized condition resulting in anode/electrolyte delamination. Consequently,

conventional WC-YSZ composites cannot be considered as a potential alternative anode for direct methane utilization.

Experimental measurements revealed that cells with a WC infiltrated YSZ support performed slightly better relative to those with conventional WC-YSZ. They also maintained their structural integrity and tolerated the internal stress caused by the phase change in WC. These observations indicate that the WC infiltrated YSZ support can be considered as a foundation for any investigation into carbide-based anode materials. Incorporation of 5 wt% ceria and 1 wt% Ru into the WC infiltrated YSZ supported electrodes was found to profoundly improve the electrochemical performance. Moreover, the addition of ceria-Ru effectively enhanced the chemical stability of the WC phase such that it did not go through a major phase change. Being compatible with methane, ceria-Ru modified WC infiltrated YSZ supported anodes are able to operate steadily on methane fuel.

Modification of WC-based anodes by Ni electrocatalyst was found to be a successful approach to improve the electrochemical performance, and to address the stability challenge posed by tungsten carbide as well as the carbon formation challenge posed by Ni. Experimental results revealed that ceria-Ni modified WC infiltrated YSZ supported anodes operated steadily on methane under open circuit condition and no carbon formation was observed. Also, under polarized condition, the cell performance remained quite stable and the carbide phase did not experience any catastrophic phase change. These observations suggest that when a Ni modified WC-based anode operates on methane, not only can the unrivaled attributes of nickel be exploited, but its tendency toward the build-up of carbon can be beneficial for stabilizing the carbide phase. Finally, it was shown that a proper cell design can effectively negate the threat to structural integrity posed by a great

deal of internal stress during oxidation-reduction-re carburization cycles.

Perhaps the most important contribution of this work to SOFC scientific literature is introducing a novel class of materials based on tungsten carbide. The results on mutual performance-stability enhancement of Ni modified WC-based anodes are highly promising for direct utilization of hydrocarbon fuels in solid oxide fuel cells—and this is just a beginning for WC-based materials. As discussed earlier in this chapter, the anode electrode operates in very demanding conditions; therefore, developing an anode material which satisfactorily meets all the requirements is simply not practical. There are advantages and drawbacks associated with each material and tungsten carbide is no exception. From this work, the major benefits of WC as a methane fuel compatible anode include high electronic conductivity, superb microstructural stability at high operating temperatures, and compatibility with highly active metallic electrocatalysts. On the other hand, the catalytic activity of WC is poor. This is clearly in contrast to numerous works on catalytic characteristics of WC which indicate a resemblance between WC and precious metals. Thus it is important to understand this contradictory behavior and improve the catalytic attributes of the carbide. In addition, the chemical stability of tungsten carbide could be a critical concern which, as shown here, should be thoroughly addressed.

### *Recommendations and Future Work*

SOFCs based on Ni-CeO<sub>2</sub> modified WC infiltrated YSZ supported anodes are of practical interest for the direct utilization of methane. They operate stably on CH<sub>4</sub> with reasonable electrochemical performance, do not suffer from carbon buildup, and maintain their

chemical stability as well as their structural integrity. The following can be the subjects of further investigations:

- This study was based on an electrolyte supported design which essentially poses a great performance loss due to the relatively high ohmic resistance of the thick electrolyte. The practical approach would be to develop a porous YSZ support which is the structural framework as well as the support for the catalysts.
- Electrochemical activity of WC is greatly influenced by the surface area as well as the synthesis of the carbide<sup>1</sup>. Thus, it is very important to synthesize WC with higher surface areas through different processing pathways to see which one results in a higher electrochemical activity toward the fuel.
- The amounts of nickel, ceria, and tungsten carbide, and also the sequence of infiltration steps should essentially be optimized.
- It would also be useful to research the electrochemical activity of this anode system toward other hydrocarbons including natural gas.

---

<sup>1</sup> Y. Hara, N. Minami, H. Matsumoto, H. Itagaki, *Appl. Catal. A* 332 (2007) 289.